Empirical Design Rules for Binder Jetting Additive Manufacturing

by

Edward Yang

A thesis
presented to the University of Waterloo
in fulfillment of the
thesis requirement for the degree of
Master of Applied Science
in
Mechanical and Mechatronics Engineering

Waterloo, Ontario, Canada, 2024

© Edward Yang 2024

Author's Declaration

I hereby declare that I am the sole author of this thesis. This is a true copy of the thesis, including any required final revisions, as accepted by my examiners.

I understand that my thesis may be made electronically available to the public.

Abstract

Metal binder jetting additive manufacturing (BJAM) is an additive manufacturing (AM) process that builds parts from a feedstock metal powder material by spreading a layer of powder, then depositing liquid binder over the desired cross-sectional area to bind the powder together. Once completed, the part is cured and depowdered, resulting in a green part with the desired form but lacking functional material properties. Heat treatment, typically in the form of sintering, is required to impart the desired properties to the material by pyrolyzing the binder and densifying the part.

During each of these steps is the challenge of creating or maintaining a dimensionally accurate part that adheres to the intended geometry of the part that was designed. Each step has interactions between process parameters, material properties, and geometric feature characteristics that determine the degree of accuracy of the finished part. Benchmarking and understanding the physical phenomena of each of these steps is a field of active research with many domains to be covered. In particular, there is a lack of information on the dimensional accuracy of the printed green parts prior to post-processing and how to design parts to achieve a desired accuracy.

The goal of this work is to develop a set of design rules that can be applied when designing for binder jetting additive manufacturing with stainless steel (SS316L). This was done by printing artifacts with geometric primitives at different scales and orientations to determine which features can be printed successfully. Six types of features were included in the design of these to examine minimum feature dimensions and clearances. The artifacts were analysed with the help of a custom developed automated computer vision approach to quantify the degree of dimensional accuracy. These results are compiled into a practical set of design rules for designers that express printability and dimensional error as a function

of feature type, nominal dimension, thickness, and orientation. Future work is proposed to expand the formalization of design rules for binder jetting additive manufacturing and to apply this workflow to other processes.

Acknowledgements

I would like to thank everyone at the Multi-Scale Additive Manufacturing lab for their support and assistance throughout my degree, particularly the past and present members of the binder jetting research group that provided valuable advice and camaraderie, and to the technical staff who were always reliable.

Thank you to Profwww. Mihaela Vlasea for supervising me and always giving me sound guidance even when the path forward was unclear, providing invaluable encouragement when it was most needed.

My sincere gratitude to Prof. Michael Mayer for his initial offer that led me down this path to pursue graduate studies and for mentoring me on how to do good research, pushing me to try new things that I could not have done otherwise.

Dedication

To many family who have loved and supported me unfailingly, giving me opportunities to learn and thrive; and to Nethy, who supported me through the many trials and tribulations of my degree.

Table of Contents

Author's Declaration ii

Abstract iii

Acknowledgements v

Dedication vi

List of Figures xi

List of Tables xviii

1 Introduction 1

1.1 Overview of design rules for BJAM 2

1.2 Thesis objectives 3

2 Background 4

2.1 Binder jetting additive manufacturing 4

2.1.1 Printing process . . . 5
2.1.2 Depowdering and post-processing . . . 8
2.1.3 Relevant process parameters . . . 9
2.1.4 Comparison to other AM technologies . . . 11
2.1.5 Materials . . . 12
2.2 Additive manufacturing benchmarks . . . 14
2.3 Design rules for additive manufacturing . . . 18

3 Artifact design **20**
3.1 Thin walls . . . 22
3.2 Thin gaps . . . 23
3.3 Vertical gaps . . . 23
3.4 Through holes . . . 24
3.5 Clearance cylinders . . . 25

4 Methodology **27**
4.1 Specimen printing and materials . . . 27
4.2 Printed orientation of specimens . . . 32
4.3 Build layouts . . . 36
4.4 Post-processing: binder curing and de-powdering . . . 37
4.5 Feature measurement workflow . . . 37

4.6 Computer vision algorithm 40
4.6.1 Part extraction and binarization 41
4.6.2 Comparison of contour against CAD model 42
4.6.3 Measured dimension and projection contour roughness from ROI . . 43

5 Results and discussion **48**
5.1 Feature printability success maps 48
5.2 Measured dimension and error 56
5.3 Overprint and underprint areas 72
5.4 Projection contour roughness 75
5.5 Clearance between solid volumes 77
5.6 Effect of process parameters 79
5.7 Proposed design rules 87
5.7.1 Thin walls 87
5.7.2 Thin gaps and vertical gaps 88
5.7.3 Through holes 88
5.7.4 Clearance 89

6 Conclusion **92**
6.1 Limitations of this work 93
6.2 Future work 94

Letters of Copyright Permission 96

References 98

List of Figures

2.1 A diagram illustrating the steps required to manufacture a part using BJAM, including post-processing 5

2.2 A diagram showing the powder spreading and jetting steps for a BJAM machine with a hopper configuration. For description of steps, see main text. 6

2.3 A diagram showing the powder spreading and jetting steps for a BJAM machine with a feed bed configuration. For description of steps, see main text. 7

2.4 Benchmark parts used by Centrum voor Productietechniek and TNO that were printed using selective laser sintering, stereolithography, and laminated object manufacturing to measure the geometric accuracy of each technology. [48] 16

2.5 The benchmark proposed by Moylan et al. [54] 16

2.6 Benchmark used by Castillo [55] 17

3.1 Views of the thin walls artifact CAD model 22

3.2 Views of the thin gaps artifact CAD model 23

3.3 Views of a vertical gaps artifact CAD model, where the vertical gap distances being tested are 0.1, 0.2, 0.3, and 0.4 mm (from left to right), and the part thickness is 1.0 mm for each feature (inset squares) 24

3.4 Views of a through holes artifact CAD model, where the hole diameters being tested are 1.6, 1.7, 1.8, 1.9, and 2.0 mm (arranged in a clockwise spiral), repeated for 1.0, 2.0, 3.0, 4.0, and 5.0 mm part thicknesses (each step from left to right) 25

3.5 Views of the clearance cylinders artifact CAD model 26

4.1 a Photo of the reduced bed volume installed in the ExOne build bed, labelled with the feed and build beds. b CAD model of how the reduced bed volume is mounted into the larger ExOne build bed 28

4.2 Photos of the BJAM printing process: a The roller is midway through spreading powder over the build bed b The printhead is partway through jetting the calculated geometry for this layer. 29

4.3 The ExOne M-Flex BJAM machine 30

4.4 The axes of the ExOne printer and how it relates to the powder spreading and printhead jetting directions 33

4.5 The names of each orientation used to print the thin wall, thin gap, and through hole artifacts; the red, green, and blue lines correspond to the X, Y, and Z axes of the BJAM machine, respectively. 34

4.6 The names of each orientation used to print the vertical gap and clearance cylinder artifacts; the red, green, and blue lines correspond to the X, Y, and Z axes of the BJAM machine, respectively. 35

4.7 An example of a build layout that contains thin wall, through hole, vertical gap, and clearance cylinder artifacts in various orientations. 36

4.8 An example of a brush used to depowder the specimens in this study. . . . 37

4.9 The setup used to capture backlit images of specimens on the Keyence VHX-700, labelled with the backlight and specimen placement 40

4.10 Stage 1 of computer vision algorithm: the workflow used to isolate the specimen projection contour from the background, demonstrated on a thin wall specimen 42

4.11 Stage 2 of computer vision algorithm: the workflow used to align the sliced CAD image with the projection contour image, demonstrated on a thin wall specimen 44

4.12 Stage 3 of computer vision algorithm: the process of extracting a feature's region of interest and measuring geometric dimensions using a best fit approximation 45

4.13 Labelled image of projection contour 47

5.1 Degree of print success for thin wall features based on the Coincident% . . 50

5.2 Degree of print success for thin gap features based on the Coincident% . . 51

5.3 Degree of print success for vertical gap features with part thickness of 1 mm 52

5.4 Degree of print success for vertical gap features with part thickness of 5 mm 52

5.5 Degree of print success for through hole features with part thickness of 1 mm 53

5.6 Degree of print success for through hole features with part thickness of 2 mm 53

5.7 Degree of print success for through hole features with part thickness of 3 mm 54

5.8 Degree of print success for through hole features with part thickness of 4 mm 54

5.9 Degree of print success for through hole features with part thickness of 5 mm 55

5.10 Measured dimension of thin wall features as calculated using Equation 4.1 plotted against their nominal dimension, categorized by orientation 57

5.11 Dimensional error of thin wall features as calculated using Equation 5.2 plotted against their nominal dimension, categorized by orientation 59

5.12 Measured dimension of thin gap features as calculated using Equation 4.1 plotted against their nominal dimension, categorized by orientation 60

5.13 Dimensional error of thin gap features as calculated using Equation 5.2 plotted against their nominal dimension, categorized by orientation 61

5.14 Measured dimension of vertical gap features as calculated by Equation 4.1, plotted against their nominal dimension, categorized by orientation, for part thickness: a 1 mm; and b 5 mm. 63

5.15 Dimensional error of vertical gap features for all orientations, as calculated using Equation 5.2, plotted against their nominal dimension, categorized by part thickness. 64

5.16 Dimensional error of vertical gap features for all orientations, plotted against their nominal dimension, categorized by part thickness. Error bars correspond to 95% confidence interval and the lines represent the linear regression evaluated for each part thickness. 65

5.17 Dimensional error of through hole features for all orientations, as calculated using Equation 5.2, plotted against their nominal dimension, categorized by part thickness 66

5.18 Dimensional error of through hole features for all nominal dimensions, as calculated using Equation 5.2, plotted against their part thickness, categorized by orientation 67

5.19 Effect of orientation on dimensional error averaged across all part thicknesses and nominal dimensions of through hole features as calculated using Equation 5.2. Error bars correspond to 95% confidence interval. 68

5.20 Effect of part thickness on dimensional error averaged across all orientations and nominal dimensions of through hole features as calculated using Equation 5.2. Error bars correspond to 95% confidence interval. 69

5.21 Dimensional error of through hole features for all nominal dimensions, plotted against their part thickness, categorized by orientation. Error bars correspond to 95% confidence interval and the lines represent the linear regression evaluated for each part thickness. 70

5.22 The build layout used to print a subset of through hole specimens, where the parts with "Flat, X aligned" orientations are stacked on top of the ones with "Flat, Y aligned" orientations, with sufficient vertical clearance. . . . 71

5.23 Warping observations in a through hole feature specimen. a Warping seen with through hole specimen, the top and bottom edges do not align with the CAD model and have overprint and underprint resepectively. b Amplified contour of warping behaviour seen along bottom edge of part in a, where the part contour curves upwards and does not follow the designed straight edge 73

5.24 Exaggerated view of how part proximity to build volume wall during printing can lead to warping, where the arrows represent the forces acting on the powder bed as the build bed moves down 74

5.25 Close-up view of a through hole feature showing the powder along the edges of the parts and how projection contour roughness is determined by the number and size of powder agglomerations. 76

5.26 Clearance cylinder printed specimen 77

5.27 Heatmap depicting the success of removing a cylinder feature from a hole with a given clearance between the concentric surfaces and a given cylinder height (part thickness). 79

5.28 Degree of success for printing thin gap features as categorized by Coincident%, split by bed temperature used during printing a specimens printed as part of main collection, with bed temperature set to 35 °C b specimens printed at an alternate bed temperature of 22 °C 81

5.29 The effect of bed temperature on dimensional error of thin wall features, averaging across all nominal dimensions and orientations. Error bars represent 95% confidence interval. 82

5.30 Oversaturation of thin gap specimen due to inadequate heating and binder evaporation, causing lumpy surfaces and poor geometric fidelity. 82

5.31 Degree of success for thin wall features based on the Coincident%, printed with powder supplied by a feed bed or; b hopper. 83

5.32 Effect of powder supply configuration on dimensional error of thin wall features, averaging across all nominal dimensions and orientations. Error bars represent 95% confidence interval. 84

5.33 Heatmap depicting the success ratio for through hole features averaged across different part thicknesses. The colour represents the ratio of number of features successfully printed, averaged across all part thicknesses, with the ratio ranging from 0 to 1 as indicated by the colour bar. This is for orientations of a Flat, X aligned and; b Flat, Y aligned 85

5.34 Effect of printer configuration on dimensional error for through hole features, averaging across all nominal dimensions, part thicknesses, and orientations. Error bars represent 95% confidence interval. 86

5.35 Proposed design rule table for thin walls, thin gaps, and vertical gaps, with graphical representations of each feature type and their orientation. 90

5.36 Proposed design rule table for through holes and clearances, with graphical representations of each feature type and their orientation. 91

6.1 Letter confirming the license to reproduce Figure 2.4 96

6.2 Letter granting appropriate permission to reproduce Figure 2.6 97

List of Tables

2.1 Materials that have been deployed with BJAM 13

2.2 Existing metal BJAM design rules 19

4.1 Technical specifications for the ExOne M-Flex BJAM printer [76] 29

4.2 Printing parameters used to print main collection of specimens, using the hopper for powder dispensing 31

4.3 Printing parameters used to print a subset of specimens, using the feed bed for powder dispensing, to test the effect of process parameters on geometric accuracy 31

5.1 Ranges used for categorizing degree of feature printability success based on its Coincident% 49

5.2 Table containing the goodness of fit as calculated using R^2 for each full linear regression used to try modelling projection contour roughness of each feature. 75

Chapter 1

Introduction

Additive manufacturing opens the doors to production of complex designs, ones that could not be easily manufactured using conventional techniques, and enables them to be made from a variety of materials, including polymers, metals, and ceramics. To maximize the potential of additive manufacturing, designers and engineers need to have a thorough understanding of the limitations and possibilities of the technology class used. One critical behaviour that needs to be understood is the dimensional accuracy of the manufactured parts. From a high level, the key is to understand how a digital part file is translated into a physical object and how closely does it match the design intent of the part. These can be expressed as a set of design rules [1] which describe the requirements that parts must meet to be successfully manufactured using a given additive manufacturing process. These design rules are expressed in numerical form, with quantified limits for what can be printed. In contrast, design guides provide broader recommendations for how parts should be designed to improve printability, repeatability, reduce post-processing work required, and optimize the physical properties of the final part [1].

1.1 Overview of design rules for BJAM

Binder jetting additive manufacturing (BJAM) of metals is a two-step process: the printing step is where the geometry of desired parts is created through a layering process and a post-processing step that involves heat treatments to impart the desired physical properties to the part such as mechanical strength, density and surface roughness [2]. BJAM has advantages over other forms of AM with regards to higher part throughput, compatibility with a variety of material classes, tunable physical properties, and greater geometric freedom [3].

Design rules and guides for a variety of AM technologies have been developed by both researchers and industrial professionals, including for laser powder bed fusion (LPBF), fused filament fabrication (FFF), selective laser sintering (SLS), and stereolithography (SLA) technologies [4]–[7]. For BJAM, existing design guidelines lack the information needed by designers to explore complex geometries and optimize designs for additive manufacturing. The information provided by manufacturers and service bureaus [7]–[9] provides guidance on a set of features but does not take into account the effects of orientation and the underlying data is not available, nor verifiable across different systems and materials. It is also in the AM community's interest to publish on robust methodologies for creating BJAM design rules and report on these design rules, as the rapid pace of changes within the AM industry means that even basic design rules and guidelines from manufacturers are prone to becoming lost and inaccessible. Emerging research into design rules for BJAM has been published by Blunk and Seibel [6] for a limited set of designs; more work can still be done to fully characterize a diverse range of design features under different print conditions and to establish a workflow to analyze and extract process-specific knowledge from such data.

Design rules are intended to cover as many features and materials possible, particularly

those that would be useful to designers, however it can be challenging to generalize design rules to new materials and process parameters in a robust manner. A need exists for a method to rapidly develop BJAM design rules for new materials, as the continuing development of AM processes enables them to be printed. For BJAM, the effect of process parameters on mechanical properties has been extensively studied [10]. An opportunity exists to direct the same level of attention to their effect on green part geometric accuracy.

1.2 Thesis objectives

This work aims to expand the body of knowledge surrounding the geometric accuracy of BJAM in two ways. The first way is to propose a robust workflow that can automatically extract data from optical images of specimens printed using BJAM and use that data to establish a set of design rules. The second is to demonstrate this workflow for a given process parameter set and material to develop preliminary design rules for desired feature types printed using a particular feedstock material and process parameter set.

Chapter 2

Background

2.1 Binder jetting additive manufacturing

Binder jetting additive manufacturing (BJAM) is a form of additive manufacturing that takes raw material powder and combines it with a liquid binder to form parts. It is a multi-step process that can be used with a wide range of materials and can be scaled up to produce large build volumes of parts. The steps used by BJAM can be broken down into the following steps: printing, curing, depowdering, and sintering, as illustrated in Figure 2.1 [11]. All these steps can be organized into two categories, the steps involved in forming the geometry of the part and the steps required to impart the desired material properties of the part. Printing is the only step that is used to create the geometry and part features, while the rest of the steps, which are considered post-processing steps, are needed to improve part density and strength, while balancing geometric shrinkage and distortion.

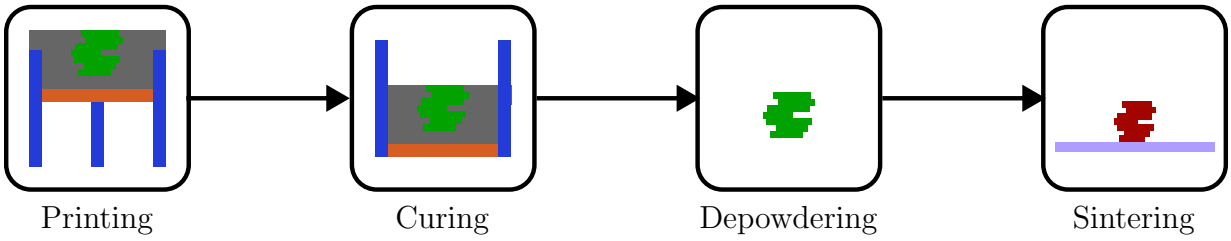


Figure 2.1: A diagram illustrating the steps required to manufacture a part using BJAM, including post-processing

2.1.1 Printing process

The printing stage is the initial step for producing parts using BJAM, where the geometry is formed using a liquid binder being jetted onto a powder bed at select locations and forming the desired geometries layer by layer. A graphical depiction of this process can be seen in Figure 2.2 for the hopper configuration of the BJAM process, where powder is supplied from above the print bed from a hopper holding powder for future layers. An explanation of the steps shown in Figure 2.2 is as follows: (1) the initial state of the printer part-way through the build process, where the green areas represented the portions of the powder bed that have already been exposed to binder to be consolidated together; (2) the build bed is lowered by a single layer height, which is typically in the range of 50 to 200 µm [10]; (3) powder is dispensed on top by a hopper that travels over the bed; (4) the loose powder dispensed in the previous step resting on top; (5) a counter-rotating roller traverses over the bed, compacting the powder and removing excess powder to ensure a consistent layer height and compaction; (6) the build bed after a complete powder layer has been deposited; (7) an inkjet printhead moves over the layer of powder, jetting liquid binder droplets into the bed to produce a 2D cross-section of the desired part geometry; (8) a heater is passed over the entire layer to partially evaporate and/or cure the binder,

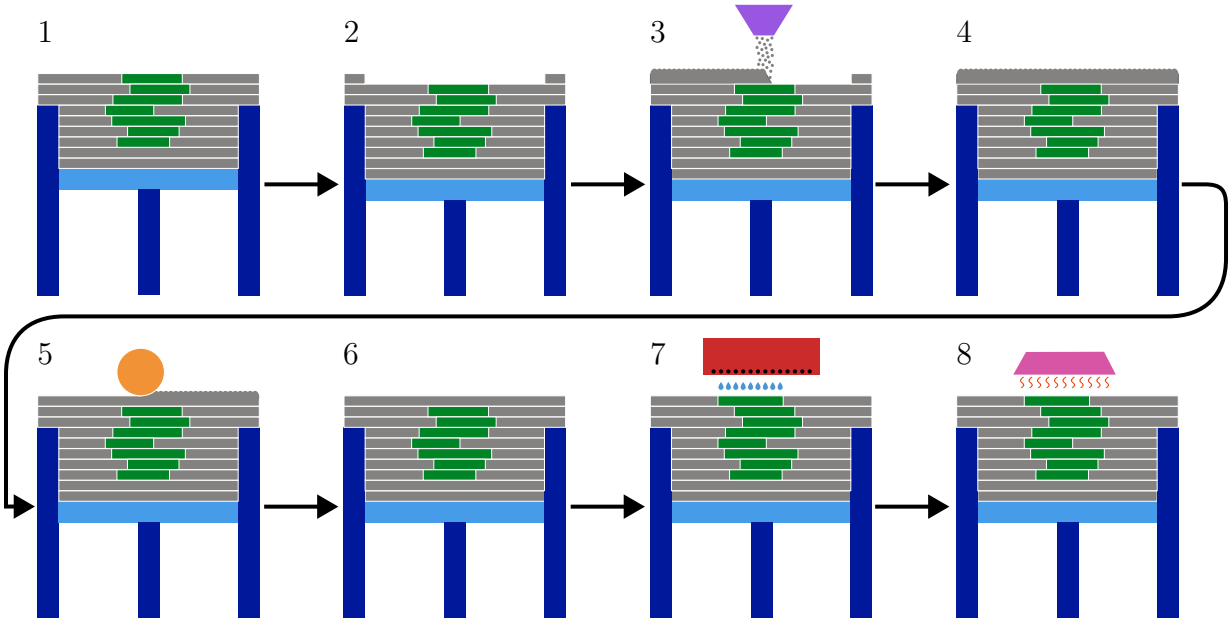


Figure 2.2: A diagram showing the powder spreading and jetting steps for a BJAM machine with a hopper configuration. For description of steps, see main text.

depending on binder chemistry, prior to repeating the process. The process for one layer is now complete, ready to repeat from step (1). This process repeats for as many layers as needed, building up the part in 2D cross sections until it is complete. The areas of the powder bed that will become the final part are now saturated with binder that will hold that portion of powder together in later steps, while the remaining powder on each layer remains loose and will be removed during depowdering. Slight variations of the BJAM process exist.

This entire process depends on the machine configuration, some BJAM machines do not employ a hopper for supplying powder but instead, rely on a feed bed to supply powder at each layer. This process can be seen in Figure 2.3, each step explained as follows: (1) the left side represents the feed bed and the right side is the print bed that contains a print

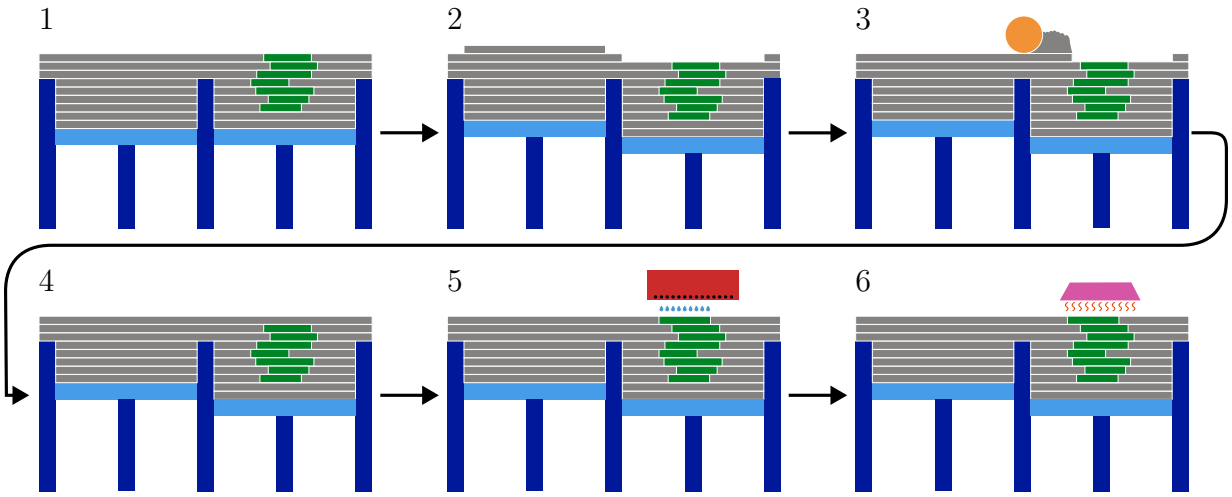


Figure 2.3: A diagram showing the powder spreading and jetting steps for a BJAM machine with a feed bed configuration. For description of steps, see main text.

in progress; (2) the build bed is lowered and the feed bed is raised by one layer height; (3) a counter rotating roller spreads the powder from the feed bed across to the build bed, compacting it into a dense layer; (4) the completed powder spreading process; (5) inkjet printhead deposits the binder; (6) a heater is passed over the powder bed. The process is now ready to repeat from step (1), as in the case for the hopper configuration.

Once the part has been built up from layers of binder-saturated powder, the whole build volume, including excess powder surrounding the part, is typically placed into an oven to fully cure the binder. The build volume is held at 175 to 450 °C, depending on the binder used, for several hours until it is fully cured [11]. Typically, the curing process is done in an ambient atmosphere and air, but can be done in an inert atmosphere depending on the material being printed. The purpose of curing the binder is to improve the strength of the part, otherwise the binder would either remain in a wet state or non-cross-linked state, and the parts would not be able to be removed from the build volume intact. Once cured,

the parts are now referred to as green parts and can be handled gently without damage.

2.1.2 Depowdering and post-processing

Depowdering is a manual process where the green parts are carefully removed from the build volume and excess powder is removed. This is typically done by hand using tools such as brushes, compressed air blow guns, or vacuum nozzles [12]. This step requires careful attention by the user, as the green parts are still delicate and any thin or detailed features could be damaged or destroyed if too much force is applied. Any excess powder from internal cavities needs to be drained out at this step, using pre-designed holes in the part. Other methods for effective depowdering using a vortex oscillator have been proposed by [13].

Once the green parts have been cleaned and excess powder removed, they are still porous, with densities typically ranging from 50-60% [10]. The particles within the powder are still only bound by the binder, thus the green part strength is very weak and a sintering post-processing step is needed to obtain the desired material properties based on the powder material system utilized. Alternatively, an infiltration step is used in lieu of sintering to form a metal matrix composite by introducing a different metal into the part.

For sintering, the part is placed into a furnace and heated to a lower temperature to first burn away the binder, then the temperature is increased and held to allow the sintering process to occur, wherein the part goes through several stages of sintering, eventually reaching a density of typically 70-92%, dependent on material class and process parameters [11]; higher densities have recently been reported [14]. The furnace has a protective gas flowing around the part to prevent oxidation. The exact details of the sintering schedule and protective gas used are chosen based on the materials that are being printed, with

the starkest differences being between different classes of materials (i.e. metals, ceramics, polymers, etc.). The sintering profile also is based on the desired properties for the final part, particularly for metals, as the microstructure is highly dependent on how the part is sintered [15].

An important aspect of particular concern is that the sintering process causes the part to shrink and deform depending on part geometry; this has to be accounted for when designing the part. This has been the subject of research that attempts to simulate and measure this deformation for a variety of materials and geometries [16]–[19].

When infiltration is used, the part is first heated to burn away the binder, then a metal with a lower melting temperature than the powder material is brought into contact with the part and both are heated in a furnace. The new metal infiltrates the material and fills the pores that existed, densifying the part [20]. Occasionally, infiltration is performed after sintering to further improve part density if the materials used are compatible and do not result in adverse mechanical properties. Infiltration was the initial technique used for densifying parts when BJAM was first developed, but the focus has shifted largely to sintering in recent years [21].

2.1.3 Relevant process parameters

BJAM has a long list of process parameters that affect the final part quality, with each step of the process having its own key parameters that then influence subsequent steps. These process parameters will be split between printing and post-processing steps. This is not an exhaustive list of process parameters, rather a collection of the key ones that have been the focus of research and have been found to have the greatest impact on final part properties.

The characteristics of the powder used during printing are critical for ensuring that the print succeeds and that the final part has desired properties. Some of the key parameters used to characterize the powder and its suitability for BJAM are the powder size distribution, mean size, morphology, flowability, and packing density [10], [22]. These properties impact the final properties of the part through two main ways, the density of the part as it is printed and sintering properties [23]. Generally, when selecting a powder, its ability to from a denser green part is desirable as it leads to greater success in sintering density outcomes and resulting part strength.

Aside from the powder feedstock, the parameters that are set on the BJAM machine as it prints each layer of the part are also critical for determining green and final part quality. The mechanisms to spread the powder evenly across the bed are dictated by parameters such as layer thickness, translational and rotational speed of the roller, and possibly even the vibration of the roller or hopper [23]. The interaction of the binder and the powder is given by the behaviour of the inkjet printhead as it deposits droplets with a certain velocity at a given distance from the powder, and the layer thickness of the powder [10]. This can be summarized as the saturation of the powder with the binder liquid and the degree to which it fills the void between particles. Excess saturation will lead to excessive powder being bound together, causing dimensional inaccuracies, while inadequate saturation will result in weak parts that will not survive the depowdering and/or post-processing steps [15]. The time spent between each layer to allow the binder to dry, as well as any heating performed to partially cure the binder also has an impact on part properties [10].

Lastly, the placement (location and orientation) of the part within the build volume can also have an impact on the final resulting parts, with differing densities based on which area of the powder bed that the part was printed [11], and increased dimensional accuracy along certain axes based on part position [24]. This is due to the spreading direction of

the powder, the jetting direction of the printhead, and gravity.

Regarding post-processing, the focus of process parameters is on the sintering step used to produce a dense part. The sintering step can involve heating the part to multiple different temperatures under various gas conditions, for set amounts of time at different heating rates, all of which impact the final density and strength of the part. The temperature can impact the type of sintering that occurs, particularly relative to the material's solidus and liquidus temperatures [10]. The gas atmosphere chosen for the sintering process can also impact final part properties [11].

For this work, the focus will be on observing geometric properties of the green parts to develop strategies to propose design rules and calibrate design features to improve printing fidelity. As such, the interplay of parameters involved in the printing process will have a significant importance.

2.1.4 Comparison to other AM technologies

In comparison to other metal powder bed AM processes, BJAM has the advantage of occurring in an ambient environment when printing. This means that larger print volumes can be used for large or multiple parts when printing. It also does not require a high energy source to melt the material that can be expensive or lead to residual thermal stresses in the printed part [25]. BJAM is also typically faster than other AM technologies due to its inkjet printhead that can quickly cover large areas of each layer instead of relying on one or multiple point sources such as lasers or electron-beams to cover that same area [10].

From a design perspective, BJAM allows metal parts to be printed without supports, as the binder jetting process can dispense binder without issue onto unsupported regions. This means that multiple layers of parts can be printed on top of each other within the

same print volume during a batch, increasing productivity. However this does not imply true support-free design freedom, as designs that will be sintered still need some supports to prevent slumping or distortion due to gravity [25].

BJAM does have certain disadvantages that need to be overcome or avoided. Some of these arise from its nature as a multi-step process, meaning that parts do require additional effort and intervention to be manufactured. The sintering step introduces a level of inaccuracy to part geometry due to shrinkage that needs to be compensated using multiple trial runs before obtaining reliable part dimensions [10]. From a design perspective, this shrinkage is dependent on the geometry of the part and accurate simulation software to predict this behaviour is an ongoing challenge. BJAM is also a powder bed process at its core, meaning that internal cavities and detailed features must be designed with depowdering in mind, ensuring that there are appropriate channels and holes for powder to be removed.

The mechanical properties of the part are also dependent on its successful densification and BJAM has many steps where defects can arise which cause entrapped porosity that hinders the part's full potential. Additionally with regards to metals, the composition of the binder may result in leftover elements in the final part that can compromise material properties, for example, leaving excess carbon in a steel parts may weaken its strength [14].

2.1.5 Materials

The range of materials compatible with BJAM can be roughly organized into three groups: metals, ceramics, and other specialty materials. Table 2.1 gives an overview of the different types of materials that have been reported in the literature as having been printed using BJAM.

Table 2.1: Materials that have been deployed with BJAM

Metals	**Ceramics**	**Specialty Materials**
Stainless Steel (316L, 420) [26], [27]	Calcium phosphate [28]	Casting sand [29]
Nickel Alloys (Inconel 718, 625) [30], [31]	Hydroxyapatite [32]	Active pharmaceutical ingredients [33]
Iron [34]	Alumina [35]	Cement [36]
Titanium [37]	Porcelain [38]	Plaster [24]
Copper [39]		Calcium Caseinate [40]
Nickel-manganese SMA [41]		Silicone [42]
Cobalt Alloys [43]		
Aluminum [44]		

BJAM can work with metals such as stainless steel for functional parts, in particular, 316L and 17-4PH stainless steels have been well studied in the existing BJAM research literature, with process parameters being optimized for those materials [15], [21], [45]. BJAM is uniquely suited for printing parts with copper as other metal AM technologies face issues printing copper due to its material properties [46]. There are a range of ceramic materials that have also been a focus of ongoing research due to their uses as bioceramics in medical applications and functional ceramics in engineering designs [47]. More specialized materials have been explored for targeted applications such as calcium caseinate which was used to print high-protein snacks [40].

The challenge with printing some of these materials is either due to powder characteristics that negatively impact its performance during the printing step or the powder behaviour when being sintered that prevents the part from reaching sufficient density. An example of difficult powder to print would be non-spherical powders as they have low flowability due to higher friction [15]. This would typically lead to either less dense layers of powder or a complete inability to spread a thin layer of powder without disturbing the underlying layers. Ongoing research is focused on addressing such challenges.

2.2 Additive manufacturing benchmarks

Throughout the history of additive manufacturing, particular part designs have been developed to be used as tools to benchmark additive manufacturing technologies [48]. A helpful classification of these benchmarks comes from Mahesh [49]: geometric benchmarks to test the dimensional accuracy of printing certain features, mechanical benchmarks for examining the mechanical properties that are independent of geometry, and process benchmarks used to compare the effects of process parameters in order to optimize said parameters.

Benchmarks in literature have changed and adapted over time, expanding into new materials and AM technology classes as they become available. One key shift has been the move from looking at pre-existing parts that are designed for a realistic functional purpose to parts intentionally designed for benchmarking with features based around various primitives such as holes, walls, cylinders, and overhangs [50]. These benchmarks usually include the most challenging situations for the AM technology being tested, where the geometric feature is likely to warp, be damaged, or fail during the printing process.

A comprehensive list of benchmarks was compiled by Rebaioli and Fassi in their review of artifacts for AM [50], and a few prominent benchmarks will be mentioned in this work to provide guidance for the design of new benchmarks. One of the earliest benchmarks depicted in Figure 2.4 and is described by Kruth as having been performed by Centrum voor Productietechniek and TNO to compare different AM processes available at the time [48]. Indeed, many of the benchmarks since then have been used to compare different additive manufacturing technologies [51]–[53].

Another benchmark part that is often referenced is one that was proposed by Moylan et al. known as the NIST test artifact, that is designed in a way to act as a geometric, mechanical, and process benchmark [54]. The benchmark contains surfaces, pins, holes, staircases, ramps, and cylinders that can be measured and can be seen in Figure 2.5. Another benchmark of particular interest is the one used by Castillo to compare different AM processes, including metal BJAM [55]. This benchmark contains hollow cylinders, holes, and multiple types of overhangs as seen in Figure 2.6.

An important consideration when deciding on benchmark parts is to ensure that the benchmark encompasses the most useful and common features for the intended AM technology. For example, it is of little use to examine the effect of extreme overhangs in AM processes such as LPBF as the design will be guaranteed to fail, whereas it may provide

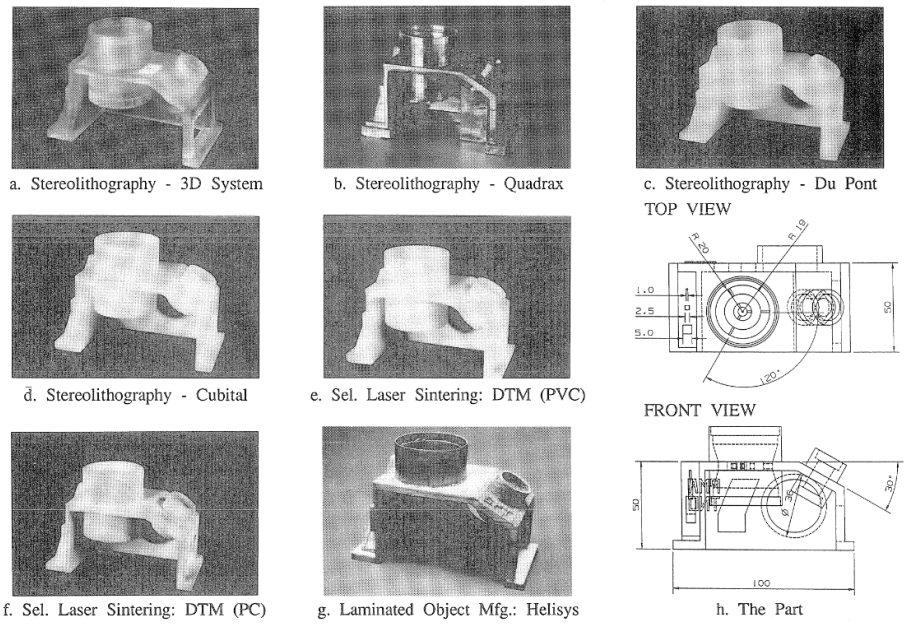


Figure 2.4: Benchmark parts used by Centrum voor Productietechniek and TNO that were printed using selective laser sintering, stereolithography, and laminated object manufacturing to measure the geometric accuracy of each technology. [48]

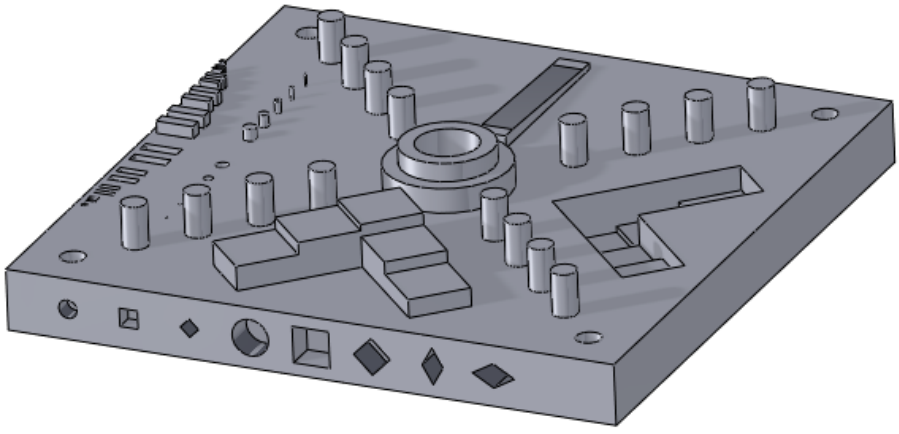


Figure 2.5: The benchmark proposed by Moylan et al. [54]

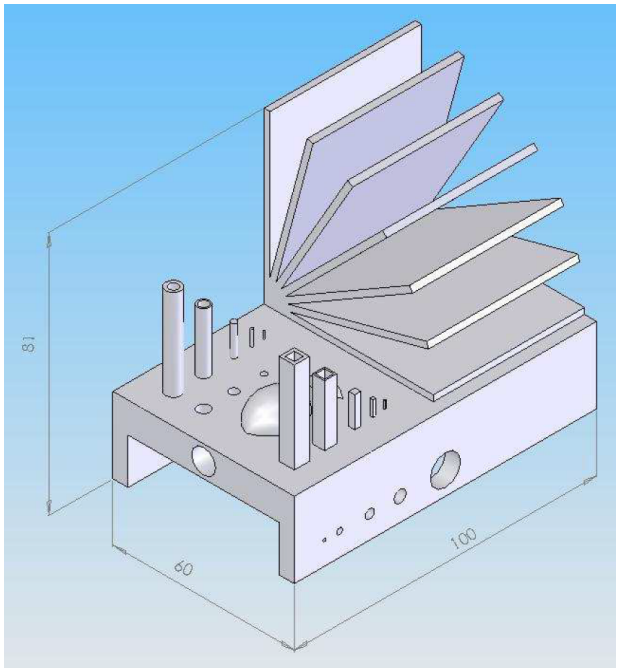


Figure 2.6: Benchmark used by Castillo [55]

little value when examining SLS technologies as overhangs pose no significant challenges to that AM class. Use cases are also important to consider, as noted by Buswell et al. [56] who focused on a wall feature when examining concrete material extrusion AM printers, as construction of building structures was their primary use case.

These manufactured benchmarks are typically measured using CMM [53], [57], [58], 3D optical scanners [59]–[63] , X-Ray CT scanning [51], [60], [64], image processing techniques [28], [65], optical microscope [66], [67], caliper gauge [24], [55], [68]. All these measurement techniques have their own benefits and drawbacks, for example, X-Ray CT scanning allows for the measurement of internal feature that would be impossible to quantify otherwise, but at high financial and time costs.

2.3 Design rules for additive manufacturing

Design guides have been developed for a variety of AM technologies, including LPBF, FFF, SLS, and SLA [4], [5], [61], [62], [69]. The most relevant ones are the powder based technologies, as they share the closest similarities to BJAM. However, these similarities cannot be directly correlated as most of these are fusion- or sinter-based processes while BJAM is unique in only having a liquid binder being deposited to form geometry from powder during the printing process.

Historically, the first BJAM machines commercially available were intended for use with plaster and ceramic materials and the geometric accuracy of parts made using these materials have been studied in the past [24], [28], [53], [58], [67], [68], [70]–[72]. Many general observations about the nature of binder saturation and the jetting process could theoretically be transferred to metal powders and binders, however experimental validation

Table 2.2: Existing metal BJAM design rules

Publication Author	Minimum wall thickness	Minimum hole diameter	Minimum inner corner radius
Blunk and Seibel [6]	0.1 mm	0.2 mm	0.06 mm
ExOne [8]	1 mm	Not given	0.8 mm
Xometry [9]	1 mm	1 mm	Not given
Schmidt-Lehr and Fuhrer [7]	0.3 mm	1.5 mm (vertical) 1.0 mm (horizontal)	0.8 mm

of these effects have not been recorded for metal powders except in a limited number of cases [22].

With regards to metal BJAM, there are only a handful of works that compile a useful set of design rules for different types of geometric features. A selection of design rules extracted from these publications is compiled in Table 2.2. The content in the industrial publications are focused more on general guidelines as opposite to numerical design rules. This motivates the goal of this work to provide a workflow that can be used to expand this body of knowledge around binder jetting design rules and formalize the design guidelines that already do exist.

Chapter 3

Artifact design

The goal is now to design benchmark artifacts that isolate design primitives that can be manufactured to test their printability and dimensional accuracy. Drawing on the work done by Seepersad et al.[5] and Castilho et al. [28], the artifacts used for this experiment will use a factorial design to test multiple levels of feature size, part thickness, and orientation. The desire is not to design a monolithic artifact that contains as many different features as possible, as done before by other researchers [54], [58], [63], but to design a series of parts that will focus on fully investigating a limited subset of features. A monolithic artifact is also undesirable, as it presents many challenges in accurately measuring the dimensions of the features it contains due to the crowding of features. Most monolithic benchmarks are also only intended to be printed in a single orientation, optimizing their overall dimensions to fit common rectangular build volumes; however, the goal of this work is to also examine how orientation affects the quality of features, making it difficult to use these existing benchmarks.

To demonstrate the workflow for developing a design guide, a subset of basic geometric

features were chosen that could be printed as specimens to collect data on their geometric fidelity and printability. For the purpose of this work, the focus was on fine features below 5 mm to investigate minimum feature sizes of BJAM.

The motivation for fine features come from applications for binder jetting for detailed features with complex geometries, to best leverage the unique capabilities of this AM technology, namely the ability to print without requiring supports and how increased complexity does not increase the printing time due to the inherent nature of jetting requiring only a constant amount of time per layer. For this work, the measure of interest is the geometric fidelity of the feature, with reference to dimensions such as the length, width, and position of the feature. Surface roughness is not within the scope of this work.

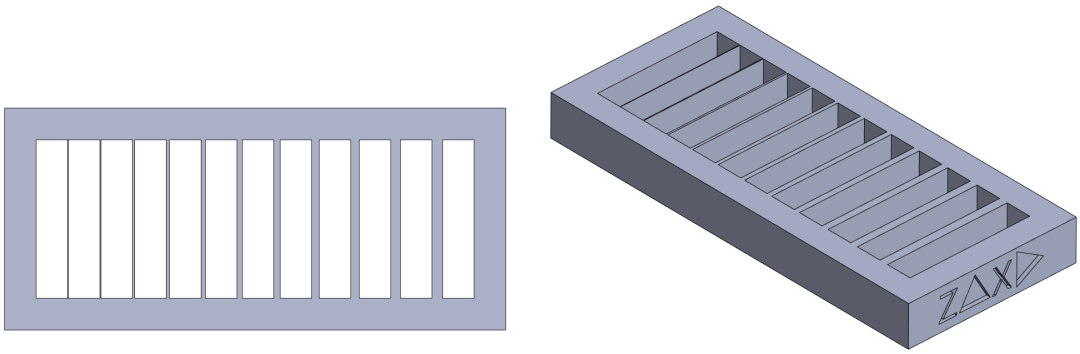
In particular, three types of geometric features were chosen: thin walls, circular through holes, and rectangular slots. Thin walls exemplify the fine features required for flexures [73] and surface lattice structures [74]. Circular through holes are representative of microchannels [75] or fine lattice structures. Lastly, rectangular slots are important for demonstrating the minimum separation between parts when laying out print beds of parts and are also important for quantifying the minimum width required for powder to escape from a negative feature; additionally, such features are important in printing of thin fins, similar to ones present in heat exchangers. This last feature is sub-divided into thin gaps along the X and Y directions and vertical gaps in the Z direction, this is since the Z axis is expected to result in different print quality behaviour [24] and also to keep the artifacts within a maximum height to reduce printing times for efficiency.

All of these features were designed to be analysed using an optical microscope, which required them to have a constant 2-dimensional cross-section for the features of interest which could be imaged to capture the entirety of the feature. This effectively meant that all these parts are extrusions of a 2D shape that has the key dimensions. In addition

to these artifacts, another artifact was designed to test the minimum clearance between surfaces that can still be successfully printed and depowdered as separate parts without fusing together. More complex geometries are out of scope of this present study and will be considered in future work.

3.1 Thin walls

The thin walls artifact is composed of 15.0 mm long walls of varying widths held together with an outer frame. The walls are separated by 3.0 mm gaps and the entire artifact is 5.0 mm thick. The wall dimensions that were examined are 0.05, 0.1, 0.2, 0.3, 0.4, 0.5, 0.6, 0.7, 0.8, 0.9, and 1.0 mm. On the side of the artifact, text is embossed that indicates the intended orientation of the part relative to the printer axes, this embossed text is standard for all artifacts used in this work. Figure 3.1a and 3.1b are the top and orthographic view of the artifact respectively.

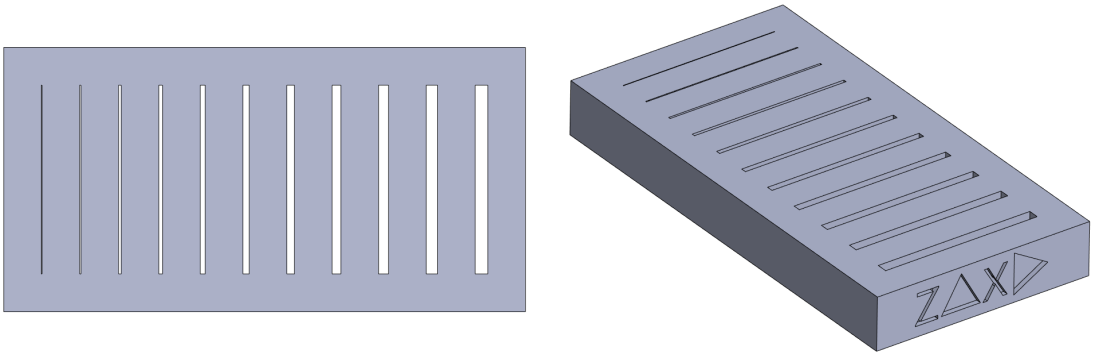


(a) Top view (b) Orthographic view

Figure 3.1: Views of the thin walls artifact CAD model

3.2 Thin gaps

The thin gaps artifact is composed of 15.0 mm long gaps of varying widths within an outer frame. The gaps are separated by 3.0 mm walls and the entire artifact is 5.0 mm thick. The gap width dimensions that were examined are 0.05, 0.1, 0.2, 0.3, 0.4, 0.5, 0.6, 0.7, 0.8, 0.9, and 1.0 mm. Figure 3.2a and 3.2b are the top and orthographic view of the artifact respectively.



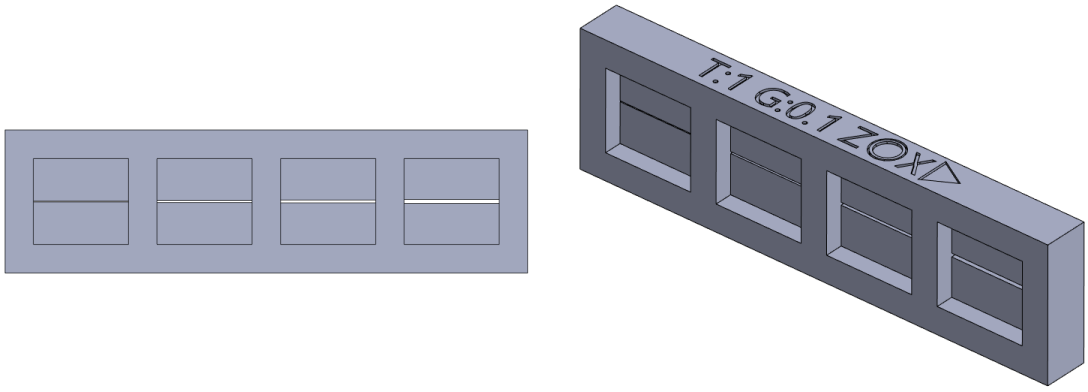
(a) Top view (b) Orthographic view

Figure 3.2: Views of the thin gaps artifact CAD model

3.3 Vertical gaps

The vertical gaps artifact has gaps that are 10 mm in length, surrounded by a 5.0 mm thick frame. The square insets around the gaps were used to set the part thickness to either 1.0 or 5.0 mm. The gap widths that were tested for this feature range from 0.1 to 0.8 mm, in increments of 0.1 mm. Each artifact has 4 different feature widths, so the complete list of

vertical gap widths is measured using 2 different artifacts. Figure 3.3a and 3.3b are the side and orthographic view of the artifact respectively.



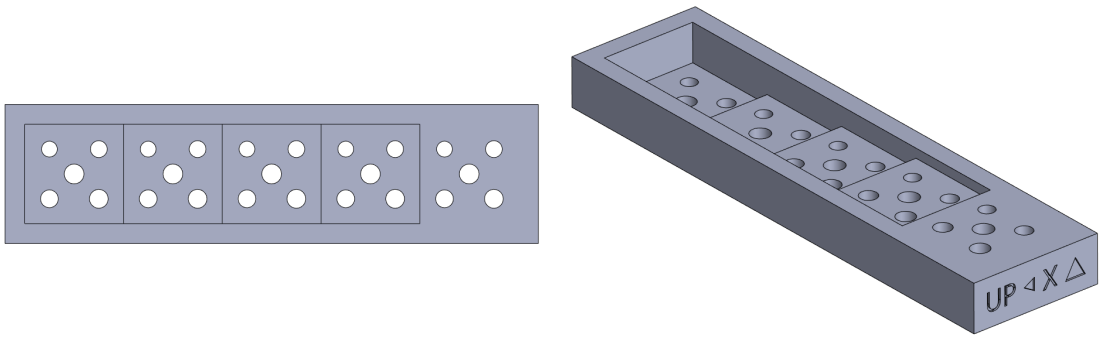
(a) Side view (b) Orthographic view

Figure 3.3: Views of a vertical gaps artifact CAD model, where the vertical gap distances being tested are 0.1, 0.2, 0.3, and 0.4 mm (from left to right), and the part thickness is 1.0 mm for each feature (inset squares)

3.4 Through holes

Each through hole artifact was designed to test 5 different hole diameters at 5 different part thicknesses to cover the full factorial design. The part thicknesses ranged from 1.0 mm to 5.0 mm, in 1.0 mm increments. The hole diameters that were tested ranged from 0.1 to 2.0 mm, in 0.1 mm increments. A total of 4 different artifacts were used to span all hole diameters in this testing range. Each artifact has 5 different hole diameters arranged in a cross pattern, with this pattern repeated 5 times for each part thickness. The entire part has a 3.0 mm frame to stabilize and protect the delicate thinner portions of the artifact.

Figure 3.4a and 3.4b are the top and orthographic view of one such artifact.

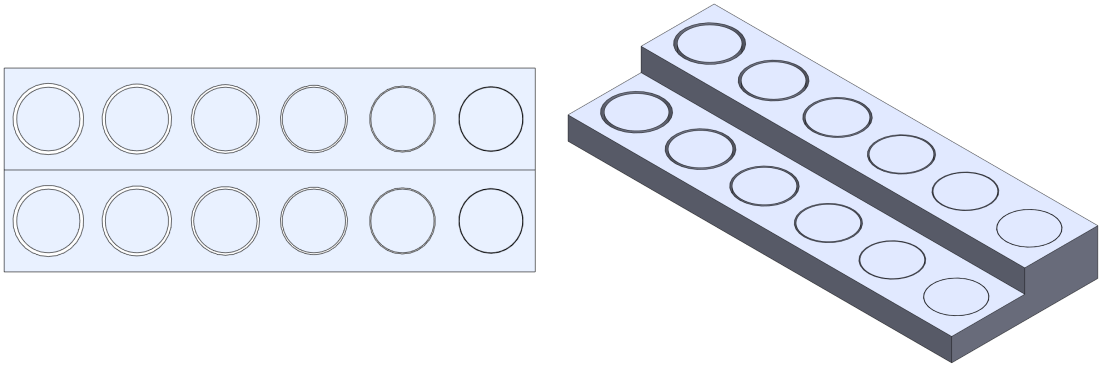


(a) Top view (b) Orthographic view

Figure 3.4: Views of a through holes artifact CAD model, where the hole diameters being tested are 1.6, 1.7, 1.8, 1.9, and 2.0 mm (arranged in a clockwise spiral), repeated for 1.0, 2.0, 3.0, 4.0, and 5.0 mm part thicknesses (each step from left to right)

3.5 Clearance cylinders

To determine the minimum clearance required between concentric geometries, an artifact was designed that had a grid of cylinders, 10.0 mm in diameter, placed inside holes with varying amounts of clearance between the cylinder and the outer wall. Clearances of 0.1, 0.2, 0.3, 0.4, 0.5, and 0.6 mm were tested. For each clearance measurement, two different heights of cylinder were used: 5.0 and 10.0 mm. This artifact can be seen in Figure 3.5b. Figure 3.5a and 3.5b are the top and orthographic view of the artifact respectively.



(a) Top view (b) Orthographic view

Figure 3.5: Views of the clearance cylinders artifact CAD model

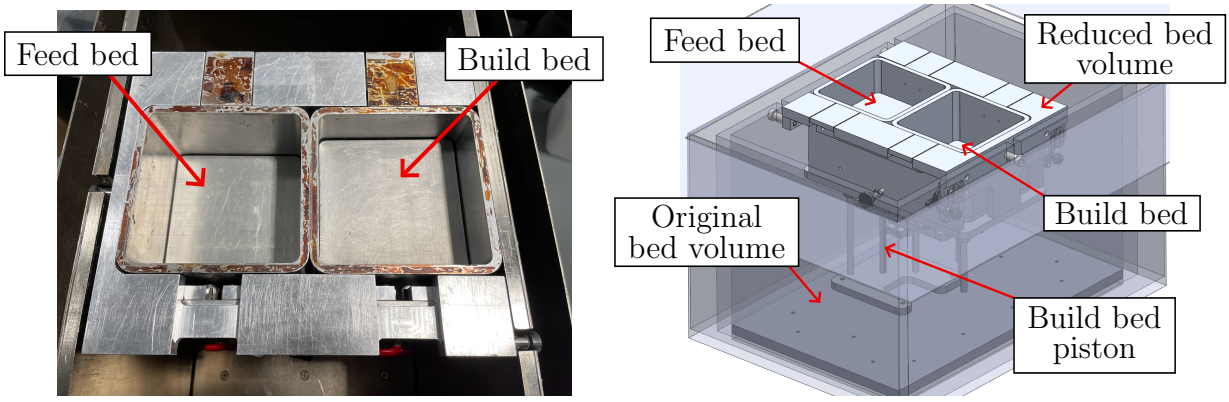
Chapter 4

Methodology

4.1 Specimen printing and materials

The specimens used for this experiment were printed using a ExOne M-Flex (ExOne, North Huntingdon, PA, USA) Binder Jetting machine. The specifications for this machine can be seen in Table 4.1 The particular machine used can be seen in Figure 4.3. All the parts were printed using a custom reduced build volume (RBV) that was designed and built in-house, which is shown in Figure 4.1. The RBV slots into the existing build volume of the machine to reduce the effective print volume to 110 x 110 x 50 mm, reducing the amount of powder required for a print job.

The RBV is also equipped with a mechanically-driven feed bed that can be enabled to move upwards and supply powder for the layering step. This allows the machine to print using either this feed bed system, or the built-in hopper powder dispensing mechanism of the ExOne machine, where the powder is dispensed using an oscillating motor for each layer. This printing process can be seen in Figure 4.2. These two methods are defined

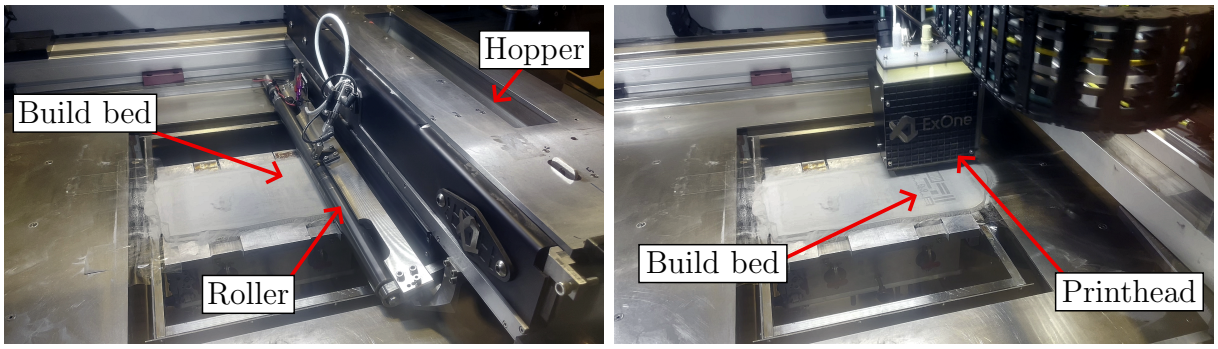


(a) (b)

Figure 4.1: (a) Photo of the reduced bed volume installed in the ExOne build bed, labelled with the feed and build beds. (b) CAD model of how the reduced bed volume is mounted into the larger ExOne build bed

by the source of powder for each new layer and are referred to as as feed bed and hopper respectively. Refer to chapter Background for more details on the differences between these two mechanisms. The powder used for all the printed specimens was a stainless steel 316L alloy (Renishaw, UK) with a particle size distribution (PSD) of 15-45 um. The powder has a spherical morphology and a PSD range with generally good flowability [22], [77]. During printing, the powder used was fresh powder blended with sieved recycled powder from prior BJAM prints. The recycled powder was processed from the leftover powder after depowdering parts nad was sieved with a 45 µm sieve (Hogentogler, Maryland, USA) to keep the PSD of the blended powder within the same original PSD. The use of recycled powder in this way is justified as the final parts have similar properties [78].

The binder used to print the specimens is the AquaFuse binder (ExOne, North Huntingdon, PA, USA). This is a proprietary aqueous polymer binder formulation that is designed for use with the ExOne M-Flex machine and is suitable for the SS316L powder material



(a) (b)

Figure 4.2: Photos of the BJAM printing process: (a) The roller is midway through spreading powder over the build bed (b) The printhead is partway through jetting the calculated geometry for this layer.

Table 4.1: Technical specifications for the ExOne M-Flex BJAM printer [76]

Build Box Dimensions	400 x 250 x 250 mm
Build Volume	25 L
Layer Height	50 - 200 µm
Print Resolution	200 dpi
Max Build Rate	1600 $cm^3\,h^{-1}$

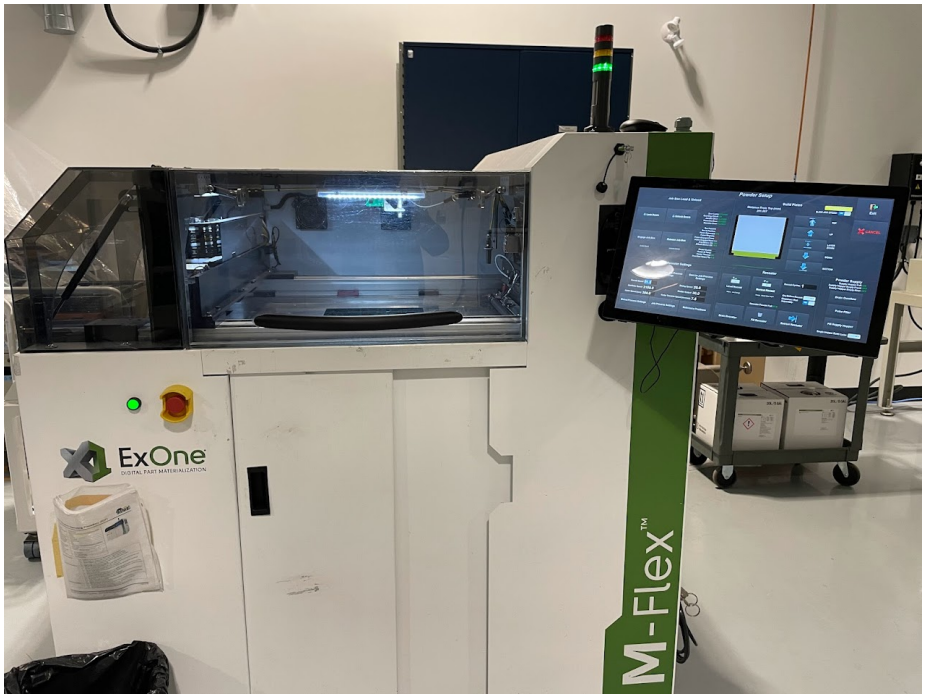


Figure 4.3: The ExOne M-Flex BJAM machine

used. The binder is dispensed using a modified piezoelectric printhead (ExOne, North Huntingdon, PA, USA) with 30 pL drop volume with a resolution of 200 dpi.

The main collection of specimens were printed using the hopper powder dispensing mechanism as it was the more reliable method for dispensing this particular material system. The printing parameters were held constant when printing these specimens and are summarized in Table 4.2. However, to compare the effects of powder feeding methods, a subset of specimen designs were also printed using the feed bed system using the parameters in Table 4.3. Some parameters were altered to improve print reliability based on previous experience with the custom RBV system. Note that hopper oscillation speed and hopper traverse speed are only applicable when printing with the hopper powder dosing; otherwise, the powder is supplied from the feed bed.

Table 4.2: Printing parameters used to print main collection of specimens, using the hopper for powder dispensing

Parameter	Value	Units
Layer Thickness	100	µm
Binder Saturation	40	%
Bed Temperature	35	°C
Roller Rotation speed	300	rpm
Roller Traverse speed	10	$\mathrm{mm\,s^{-1}}$
Hopper Oscillator Speed	1800	rpm
Hopper Traverse speed	170	$\mathrm{mm\,s^{-1}}$

Table 4.3: Printing parameters used to print a subset of specimens, using the feed bed for powder dispensing, to test the effect of process parameters on geometric accuracy

Parameter	Value	Units
Layer Thickness	100	µm
Binder Saturation	45	%
Bed Temperature	22	°C
Roller Rotation speed	300	rpm
Roller Traverse speed	10	$\mathrm{mm\,s^{-1}}$

Similarly, a subset of specimen designs were printed with the bed temperature process parameter set to 22 °C to investigate the effect of that parameter on geometric accuracy of features.

4.2 Printed orientation of specimens

Each artifact design was printed in multiple orientations to examine the effect of the printing direction on geometric accuracy. Each orientation was defined in terms of the machine's axes, which are shown in Figure 4.4. For the thin wall feature artifact, it was printed in four orientations, all keeping the walls vertical while rotating it about the Z axis to align the length of the walls with the X, Y positive diagonal (XY), and negative diagonal (YX) directions, as seen in Figure 4.5a. The same four orientations were used for the thin gap feature artifact, shown in Figure 4.5b. For the vertical gap feature artifact, two orientations were used, keeping the gap vertical and rotating the part about the Z axis to align the length of the gap with the X or Y direction, as seen in Figure 4.6a. The through hole feature artifacts were printed in four different orientations, two of which keep the holes aligned vertically and aligning the overall part along the X or Y direction, and two of which align the holes horizontally and the overall part along the X or Y direction, labelled as shown in Figure 4.5c. The clearance cylinder artifact was printed in two orientations, aligning the length of the part along the X or Y direction while keeping the cylinder vertical, as seen in Figure 4.6b.

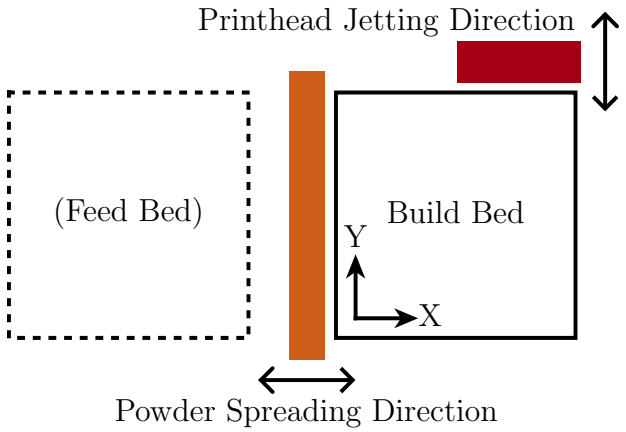
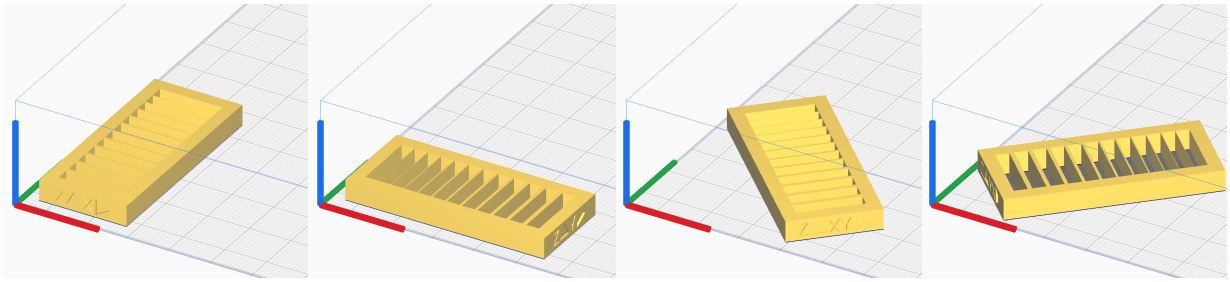
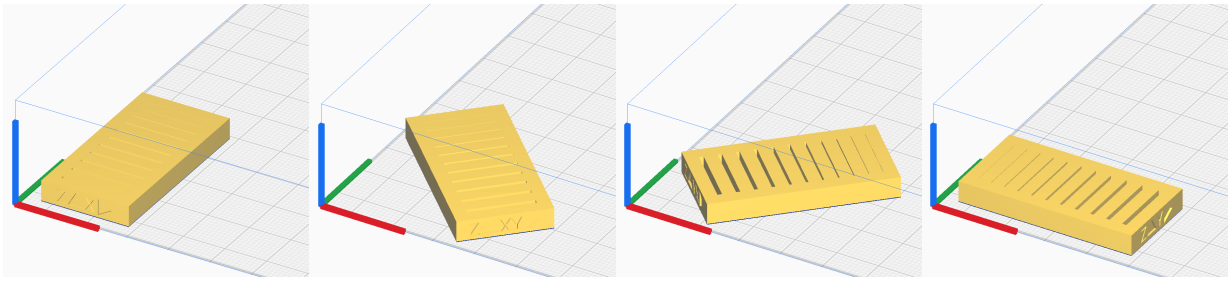


Figure 4.4: The axes of the ExOne printer and how it relates to the powder spreading and printhead jetting directions



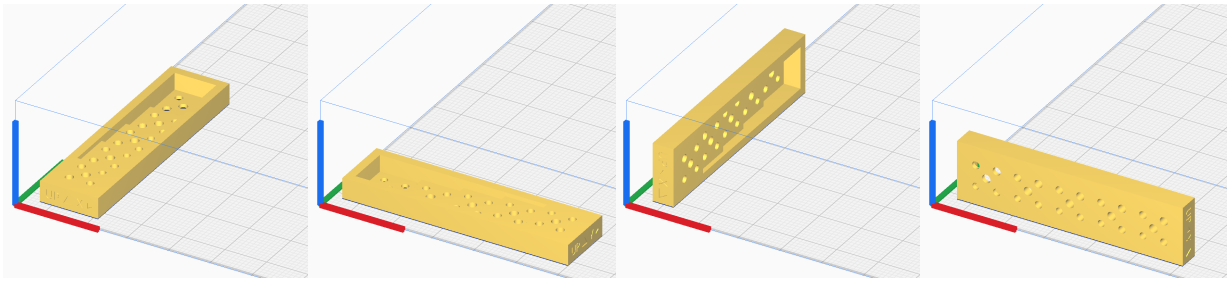
Flat, X aligned | Flat, Y aligned | Flat, XY aligned | Flat, YX aligned

(a) Thin wall feature artifact



Flat, X aligned | Flat, Y aligned | Flat, XY aligned | Flat, YX aligned

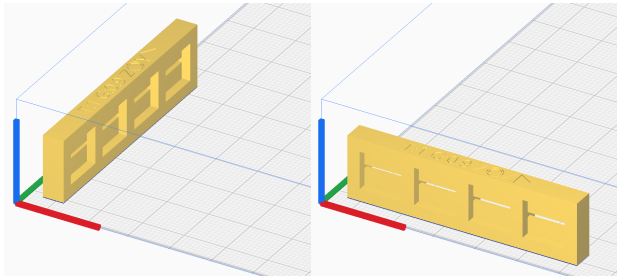
(b) Thin gap feature artifact



Flat, X aligned | Flat, Y aligned | Upright, X aligned | Upright, Y aligned

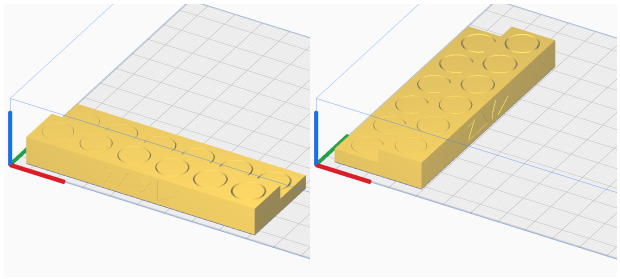
(c) Through hole feature artifact

Figure 4.5: The names of each orientation used to print the thin wall, thin gap, and through hole artifacts; the red, green, and blue lines correspond to the X, Y, and Z axes of the BJAM machine, respectively.



Upright, X aligned Upright, Y aligned

(a) Vertical gap feature artifact



Upright, X aligned Upright, Y aligned

(b) Clearance cylinder feature artifact

Figure 4.6: The names of each orientation used to print the vertical gap and clearance cylinder artifacts; the red, green, and blue lines correspond to the X, Y, and Z axes of the BJAM machine, respectively.

4.3 Build layouts

The build layouts were prepared using Cura software (Cura 5.4.0, Ultimaker, Netherlands) [79], where all the design files were exported from the CAD software (Solidworks 2022, Dassault Systèmes, France) in stereolithography (.stl) format and imported into Cura to arrange within the build volume. The parts were arranged to maximize the number of parts that can fit inside the build volume while maintaining their required orientations. Parts were separated by a minimum of 0.5 mm spacing as a conservative estimate to ensure that parts did not get stuck together [6]. The complete build volume was then exported as a 3D Manufacturing Format (.3mf) file to reduce the overall file size. This file was then transferred to the ExOne machine to start each print job.

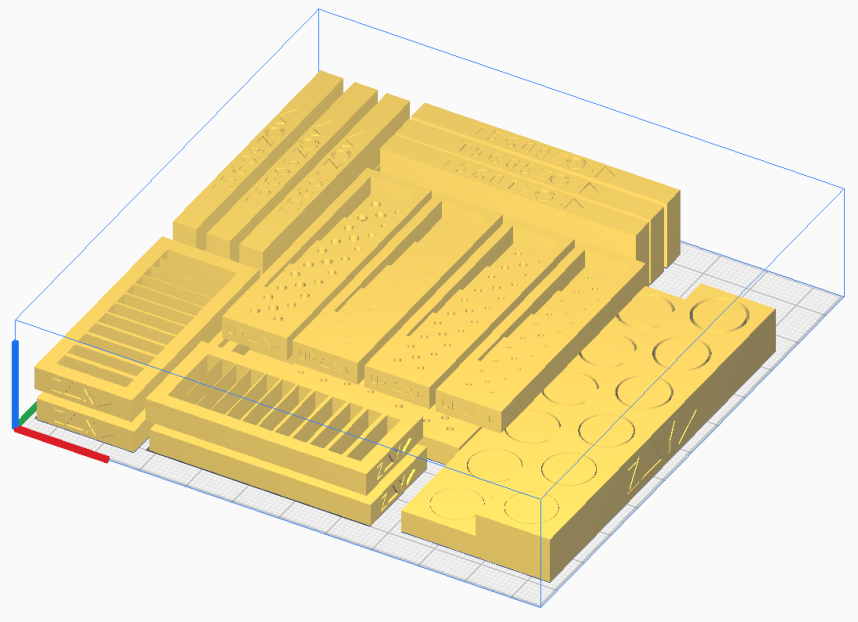


Figure 4.7: An example of a build layout that contains thin wall, through hole, vertical gap, and clearance cylinder artifacts in various orientations.

4.4 Post-processing: binder curing and de-powdering

The specimens all underwent a curing process as is typical for binder jetted parts, placing the whole bed volume into an oven (CT-333, JPW) and heating it to 180 °C for 12 h under open atmospheric conditions. The parts were then cooled down to room temperature before depowdering.

Depowdering was conducted by hand using a fine flat paint brush with polymer bristles to brush away sufficient powder from portions of the build volume before carefully extracting the fragile green parts from the loose powder. An example of such a brush is seen in Figure 4.8, the brush is approximately 15 mm wide and each bristle is approximately 100 µm thick. Once parts were extracted from the bulk of the powder bed, depowdering of the features and surfaces of the each specimen was carried out using the fine paint brush and a metal hypodermic needle to dislodge as much powder as possible with minimal damage to the specimen.



Figure 4.8: An example of a brush used to depowder the specimens in this study.

4.5 Feature measurement workflow

The measurement of the the geometric features of the specimens were carried out while they were still in a green part state, that is, after they have been cured and depowdered but prior to densification through sintering and any other heat treatment or post-processing.

This was done so that the data would reflect the capabilities of the binder jetting process on parts as they come out of the machine, without introducing additional factors that come from shrinkage and deformation of parts during post-processing [15]. By isolating the behaviour of how the binder jetting process translates digital CAD geometry into physical part features, improvements can be made to the part design and printing process independently of post-processing steps.

Additionally, work has been ongoing to develop simulation models to predict the effects of sintering on geometric distortion with the goal of counteracting these effects by applying an inverse transformation to the digital file prior to printing and sintering [17], [80]. A good understanding of the geometric accuracy of green parts and the ability to correct dimensional error that occurs during the printing stage is thus essential for a complete workflow that can manufacture highly accurate usable parts by accounting for the effects of each step along the process.

To analyze the specimen images, an approach based on existing optical comparator and vision measuring machine systems was developed. The principle was to use a non-contact measurement approach that could accurately and repeatably measure the dimensions of geometric features while minimizing operator influence. A non-contact method was required as the green parts produced by the BJAM process were fragile and the smallest features could not be measured using conventional methods such as a micrometer or CMM without damaging or destroying the feature entirely. The physical force applied by such a probe on a small contact area also easily indent the green part, affecting the measurement and altering the specimen. A visual measurement approach promises that parts can be measured quickly, with only a single image required to collect data on all geometric features of a specimen. Other non-contact methods such as optical 3d scanning / photogrammetry were considered [60], however it would not be possible to accurately inspect features such

as thin gaps or narrow holes due to the limited number of perspectives from which such a feature could be observed and the difficulty in evenly illuminating occluded surfaces. Another barrier to photogrammetry techniques is the reflective surface of the parts, which cannot be mitigating using the conventional technique of a matte scanning spray as the chemicals within such a spray dissolve the binder holding the green part together, causing the specimen to disintegrate. X-ray CT scanning was not a cost effective option for the number of samples that needed to be analysed.

The specimens were optically imaged using a digital microscope (VHX-700, Keyence) with a 20x objective lens and 3.19 megapixel CMOS image sensor while lit with a ring light from the top and with a diffuse LED backlight from underneath. This arrangement can be seen in Figure 4.9. The purpose of the backlight was to clearly indicate which portions of the part had been sufficiently depowdered to permit light to be transmitted through the entire thickness of the feature and to provide an even contrasting background to simplify the extraction of the specimen contours. Multiple images were taken to capture the entirety of each specimen and were then stitched together to form a larger image that contained the extents of each specimen. To reduce the effect of blurry edges from out of focus images, focus stacking was employed to combine images taken at different focal distances to create a composite image that kept the portions of each image that were in focus, effectively increasing the depth of field [81]. This does introduce some error due to the perspective view of the microscope, as the surface of the part closest to the lens will appear larger than the bottom surface farther away, however over the constrained height of the specimen designs (5-10 mm) this effect is negligible.

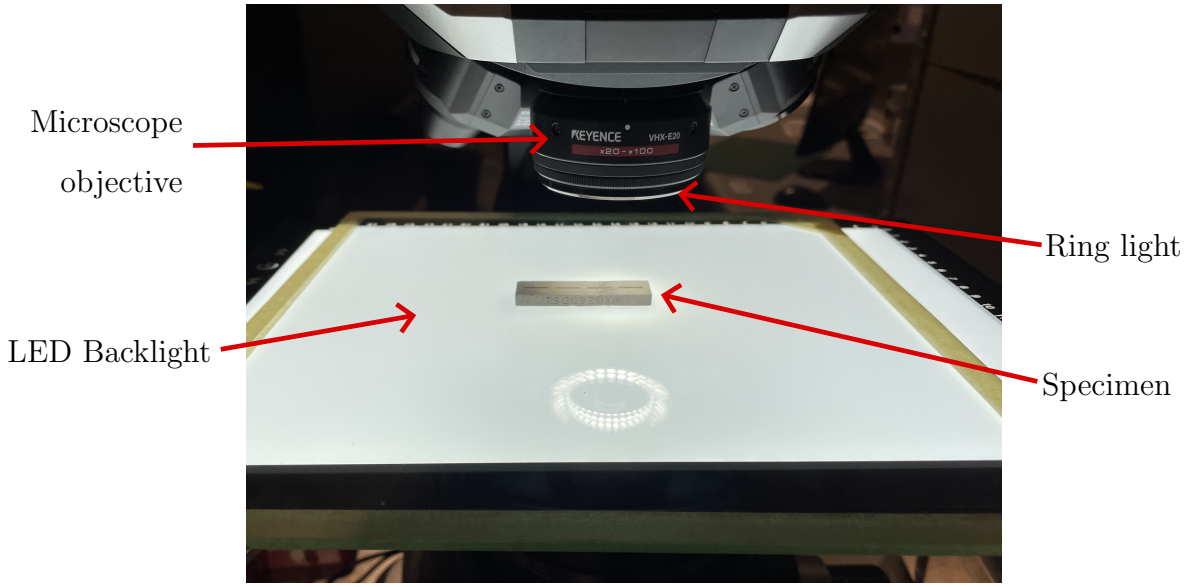


Figure 4.9: The setup used to capture backlit images of specimens on the Keyence VHX-700, labelled with the backlight and specimen placement

4.6 Computer vision algorithm

Work by other researchers at using computer vision to perform metrology of additively manufactured geometric features has proven effective [28], [65] at extracting data from a large number of features. This previous work used algorithms written for MATLAB [65] or ImageJ [28]. For this work, a new software package (Open-OpticalComparator) was written in Python to process images from the optical miroscope [82]. This was motivated by the desire to have an open software framework built for optical metrology approaches that could easily be automated for batch processing of images and potentially tailored for in-situ detection of geometric features. The code is available for download at https://github.com/ewdyang/Open-OpticalComparator.

Having the algorithm implemented in Python also allows the use of libraries for image

processing and scientific computing available for Python. The Open-OpticalComparator software employed various libraries including OpenCV and scikit-image to apply computer vision strategies to extract data on geometric features from images of parts [83], [84]. These strategies are explained in detail below. Other libraries for loading .stl files and performing optimization for fitting lines were also used [85]–[90].

This process is divided into three stages, the first step is to convert the raw image into a binarized image that separates the specimen from the background. The portion of the image containing the specimen is denoted the projection contour area. The next step is to calculate the appropriate 2D planar cross-section of the 3D CAD file and align it with the position of the specimen in the image so that it can be overlaid. The last step is to crop the image to each individual geometric feature of interest and perform dimensional measurements.

4.6.1 Part extraction and binarization

Stage 1 is the process of separating the part from the background and binarizing the image according, which is outlined in Figure 4.10. The first step is to convert the colour image into a grayscale equivalent. This then allows the image to be have a threshold operation applied that sets all pixels above a certain intensity to the maximum value and the rest to zero. The scale bar is used to calculate the scale of the image in pixels per mm and is then covered in the image to prevent it from affect later operations. The next operation is to apply a morphological opening operation, which removes the noise from the interior area of the part contour. A morphological closing operation is then applied to remove specks from the background of the image. Finally, the entire image is inverted so that the high intensity (white) pixels with correspond to the projection contour area and the low

intensity (black) pixels correspond to the background. This final image is a binary image, with only 2 possible values for each pixel, either low or high which correspond to 0 and 255 (the maximum integer value used by the image data structure).

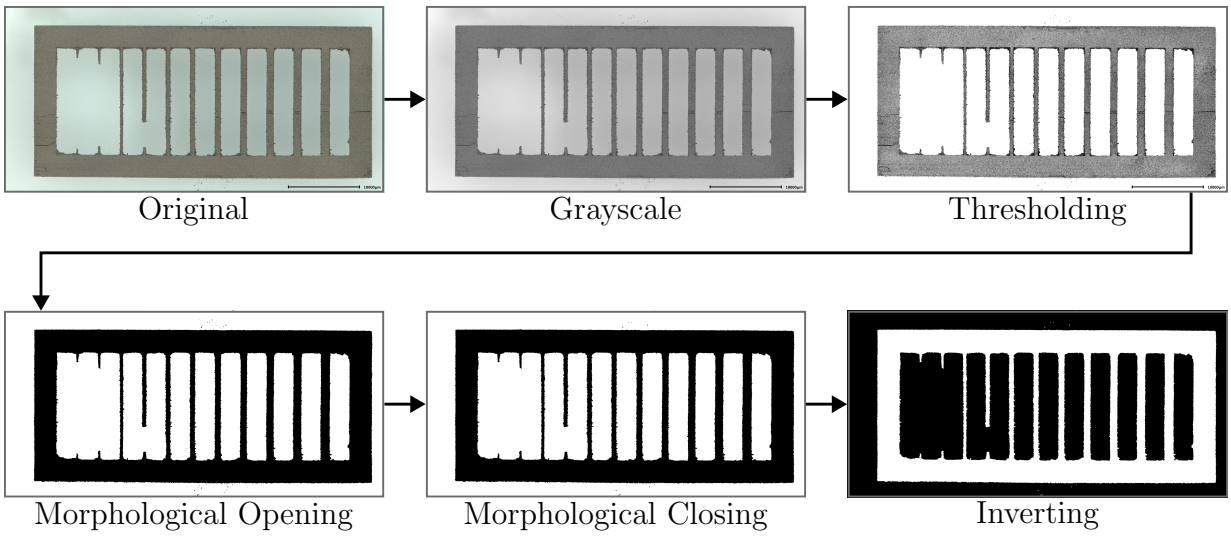


Figure 4.10: Stage 1 of computer vision algorithm: the workflow used to isolate the specimen projection contour from the background, demonstrated on a thin wall specimen

4.6.2 Comparison of contour against CAD model

Stage 2 is to compare the projection contour against the CAD model file that was used to manufacture the specimen. The goal is to identify the areas where the specimen lacks material or is missing features, which is referred to as underprinting, and the areas where the specimen has excess material, which is called overprinting [74]. The areas where the specimen has material exactly as described by the CAD file is the coincident area. The steps required for this are shown in Figure 4.11. A 2D image is produced from the 3D CAD file by slicing the 3D geometry with a plane that has a normal that corresponds to

the orientation of the part when it was imaged, and taking intersection of the part with the plane. This image is scaled appropriately so that the 2D slice has the same pixel / mm scale as the projection contour image. In order to align this sliced image with the projection contour, the 4 corners of each area are found using a Harris corner detector algorithm. A Euclidean transform is calculated by taking the corners from the CAD slice image as the input and the corners in the projection contour as the destination, which gives the necessary information to align the two images. A Euclidean transform only involves translation and rotation so no scaling or skew factor will be applied, allowing for an accurate one-to-one comparison. Once the two images are properly aligned, they can be combined to give information on how the as-printed part compares to the digital geometry. The comparison image utilizes different colours to provide a visual reference of where the part is underprinted (red), overprinted (green), or coincident (yellow). The underprinted area and overprinted area can be independently determined by applying a bitwise AND operation between the inverted projection contour and non-inverted aligned CAD slice image for the case of underprinting, or the inverted aligned CAD slice image and the non-inverted projection contour for the case of overprinting.

4.6.3 Measured dimension and projection contour roughness from ROI

Stage 3 of the computer vision process is to isolate the geometric features that are being tested, as seen in Figure 4.12. The image needs to be cropped or masked to limit calculations on individual features. A region of interest (ROI) is defined for each feature within the CAD slice. For the rectilinear features, (thin wall, gap width, and vertical gap) this ROI is selected around the central portion of the feature, avoiding any internal corners which

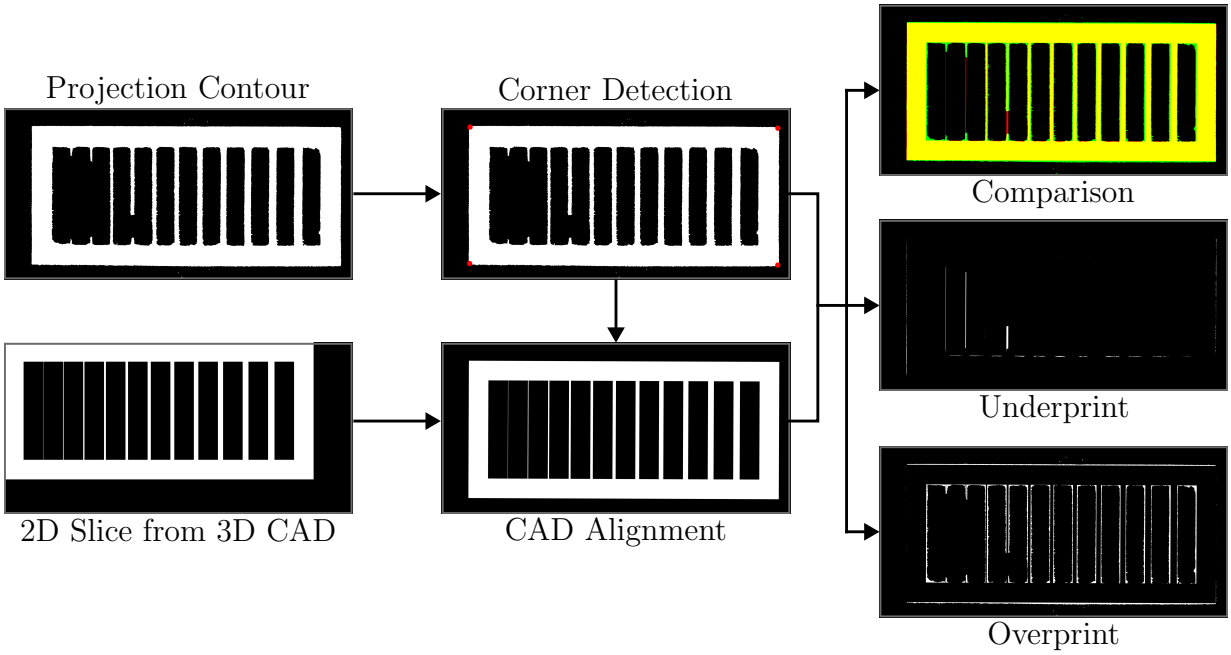


Figure 4.11: Stage 2 of computer vision algorithm: the workflow used to align the sliced CAD image with the projection contour image, demonstrated on a thin wall specimen

have their own dimensional variability. For circular features, the whole shape is included in the ROI. The Euclidean transform calculated in the previous stage is then applied to the ROI coordinates so that they correspond to the positions of the correct features on the projection contour image. These transformed ROI coordinates are used to crop the overprint and underprint images so that a consistent region is used between features to count the number of pixels in the overprint and underprint regions, which corresponds to their areas. To facilitate analysis, the overprint and underprint can be expressed as a percentage relative to the nominal area of the feature. Note that the nominal area for positive features such as for thin walls is defined as the area where material is present, whereas the nominal area for negative features such as through holes is defined as the area where material is not present. The ROI coordinates are also used to crop the projection contour images to

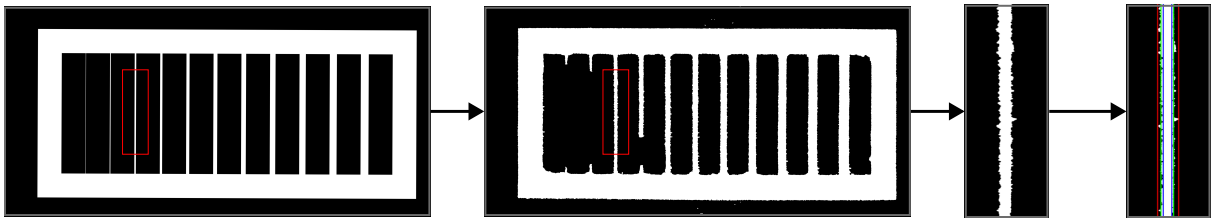


Figure 4.12: Stage 3 of computer vision algorithm: the process of extracting a feature's region of interest and measuring geometric dimensions using a best fit approximation

calculate the measured dimension of each feature independently of the CAD file. For linear features, a line is fitted using the arithmetic mean of the horizontal coordinates of points along the left and right contour edge, and the distance between these two averaged lines is taken as the measured dimension. This is expressed in Equation 4.1, where $D_{measured}$ is the calculated linear measurement, x_{R_i} is the horizontal coordinate of a point i, for all n_R points on the right edge, and x_{L_i} is the horizontal coordinate of a point j on the left edge for all n_L points on the left edge. The minimum dimension representing the largest width that fits within the projection contour and the maximum dimension representing the smallest width that covers the full extent of the projection contour is also determined. This entire process is rotated as needed for vertical features.

$$D_{measured} = \frac{1}{n_R}\sum_{i=0}^{n_R} x_{R_i} - \frac{1}{n_L}\sum_{j=0}^{n_L} x_{L_i} \tag{4.1}$$

For circular features, namely the through hole feature, the process is adapted to fit a circle using a linear least squares optimization as described by Coope [91], and using its diameter as the measured dimension . The minimum and maximum dimensions are taken as the diameters of the inscribed and circumscribed circles of the contour outline.

To capture the quality of the how well the projection contour follows a fit dimension, a metric called projection contour roughness (PCR) was formulated, as detailed in Equation

4.2. This measure is calculated by taking the sum of the absolute distance between each point along the edge of the contour and the its closest point on the fit line, which is then divided by the length of the contour. This can be expressed in equation 4.2, where z_i denotes the distance to the fit line for contour point i, and there are n points along the contour. These measurements are labelled on Figure 4.13.

$$PCR = \frac{1}{n}\sum_{i=0}^{n}|z_i| \tag{4.2}$$

This measure is analogous to the Ra surface roughness measure which is commonly used as an indicator of surface quality when discussing additively manufactured specimens. Ra measures surface roughness by taking the arithmetic mean of the absolute value of surface deviations from the calculated mean height [52], [92], as described in Equation 4.3, where l is the length along which measurements are taken and $z(x)$ is the distance from the profile to the mean line for position x along the length.

$$Ra = \frac{1}{l}\int_{0}^{l}|z(x)|dx \tag{4.3}$$

The key differences is that the Ra surface roughness is intended to be applied to measurement made along a single line, while PCR is calculated on a contour made by combining the projections of all contours at each depth through the part. Due to the way the parts are imaged, it is not possible to separate out the contour of the part at a given height slice. Additionally, the two are differentiated by having PCR be normalized around the length of the contour while Ra is normalized against the ideal length. Nevertheless, PCR can give an quantitative measure of the quality of the feature, indicating whether the overall edge of the feature is ragged or smooth.

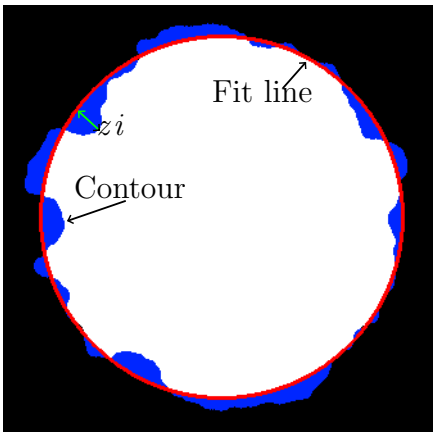


Figure 4.13: Labelled image of projection contour

Chapter 5

Results and discussion

5.1 Feature printability success maps

The first metric that was examined is whether features printed successfully, to what degree their geometry coincides with the desired CAD model, and the likelihood of successful printing across specimens. This was done to see which features can be reliably printed and determine the minimal designed feature size. To do this, first each feature had its coincident percentage calculated, which is the area of the physical print coincident with the CAD, normalized by the nominal area, as expressed in Equation 5.1. The nominal area of a feature is defined as the area that defines the feature, which is the area with material for a positive feature such as the thin wall, or the area without material for a negative feature such as the thin gap. Each feature was then categorized based on its coincident percentage, as detailed in Table 5.1. The thresholds for the Coincident% can be customized based on tolerance to failure for printing features; the thresholds in this study

were decided based on expert domain knowledge.

$$Coincident\% = \frac{Coincident\ Area}{Nominal\ Area} \tag{5.1}$$

The results for the thin wall feature are shown in Figure 5.1, organized by the printing orientation and the nominal dimension of the feature. It is observed that the Flat, Y aligned orientation was the only orientation that allowed the thinnest walls less than 0.1 mm thick to be printed. This is likely explained by the method of which the printhead deposits binder. As the printhead moves along the Y direction, a row of nozzles jets droplets to generate the desired part geometry cross section at that specific layer. In the case where the wall length is aligned with the X direction, all nozzles must fire at precisely the same time and each droplet must fall onto the powder at the same Y position in order for a coherent feature to form. If any of the nozzles fail to jet or jets earlier/later than the others, the resulting feature will likely be much weaker and prone to damage during post-processing. In contrast, for walls aligned in the Y direction, a specific set of nozzles only need to jet repeated to form a consistent coherent feature, and it is much less sensitive to timing issues. A similar mapping can be made for the thin gap feature and can be seen in Figure 5.2. It can be observed that for this feature, no fully successful instances are observed. Reasons for this will be discussed further below when examining the dimensional

Table 5.1: Ranges used for categorizing degree of feature printability success based on its Coincident%

Category	Range
Fail	Coincident% $<$ 1%
Partial Success	1% $<$ Coincident% $<$ 75%
Success	75% $<$ Coincident%

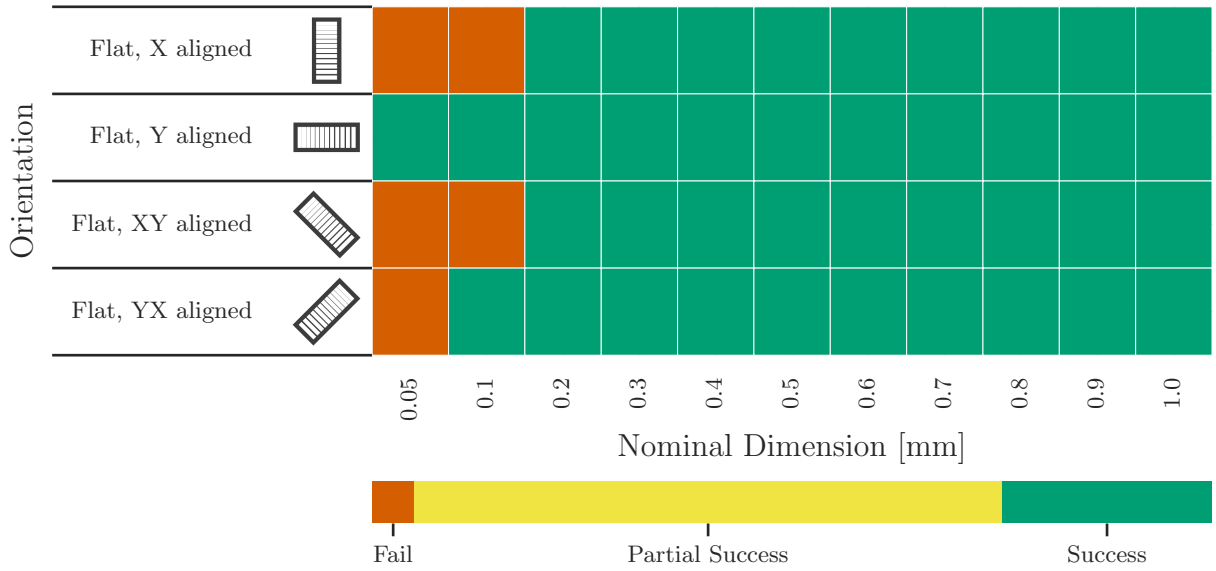


Figure 5.1: Degree of print success for thin wall features based on the Coincident%

error of this feature. The results for the vertical gap feature are captured in Figure 5.3 and Figure 5.4 for 1 and 5 mm thick gaps respectively. For the vertical gap, it is observed that the feature with a 1 mm part thickness is more likely to print successfully compared to the same sized feature with a 5 mm part thickness, particularly for nominal dimensions below 0.6 mm. Because this is a negative feature, the most likely cause for a failure is due to residual powder that is still contained in the part. The trends seen are consistent with the behaviour that is expected when depowdering parts, as it indicates powder is more unlikely to be fully removed from tall narrow crevices. No particular orientation is preferred for this feature, as the dimension of interest is along the Z axis and thus the impact of spreading or jetting direction is minimal. Overall, for 1 mm thick gaps design features, the success threshold is observed at the nominal feature size of 0.4 mm for both upright part orientations, along the X- and Y-directions; for 5 mm thick gaps, the 0.7 mm threshold is observed in both orientations.

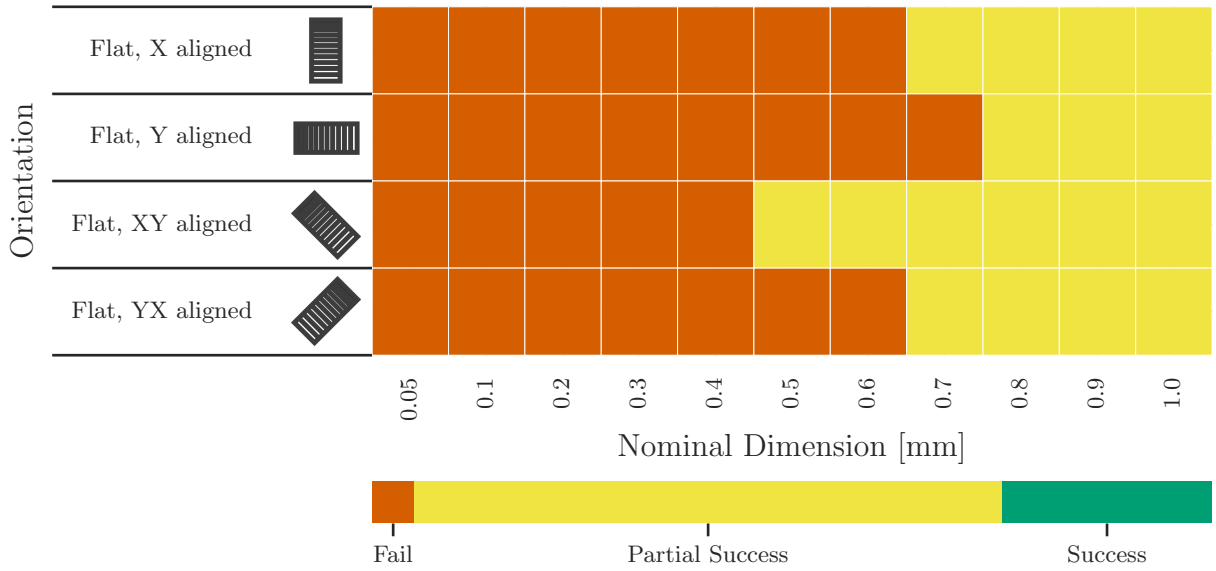


Figure 5.2: Degree of print success for thin gap features based on the Coincident%

The results for through hole features are in Figures 5.5 to 5.9, organized by part thickness, which is the length of the through hole. The two overall trends that can be seen from these observations is that smaller diameter holes are more likely to experiencing printing failures and that smaller part thicknesses are more likely to print successfully. Both of these patterns are in line with earlier results from the thin gap feature that indicate that negative features with large aspect ratios, such as long narrow holes, will not be fully depowdered and suffer from issues. In conjunction with depowdering issues, another explanation is that the effect of under-cured binder due to excessive saturation or insufficient heating is more pronounced at lower layers of a part, as observed by Miyanaji et al [93], [94]. The additional weight of the upper layers causes the additional binder that accumulates in that portion of the part to penetrate to the lower layers, increasing dimensional error as the binder migrates towards areas of lower binder saturation.

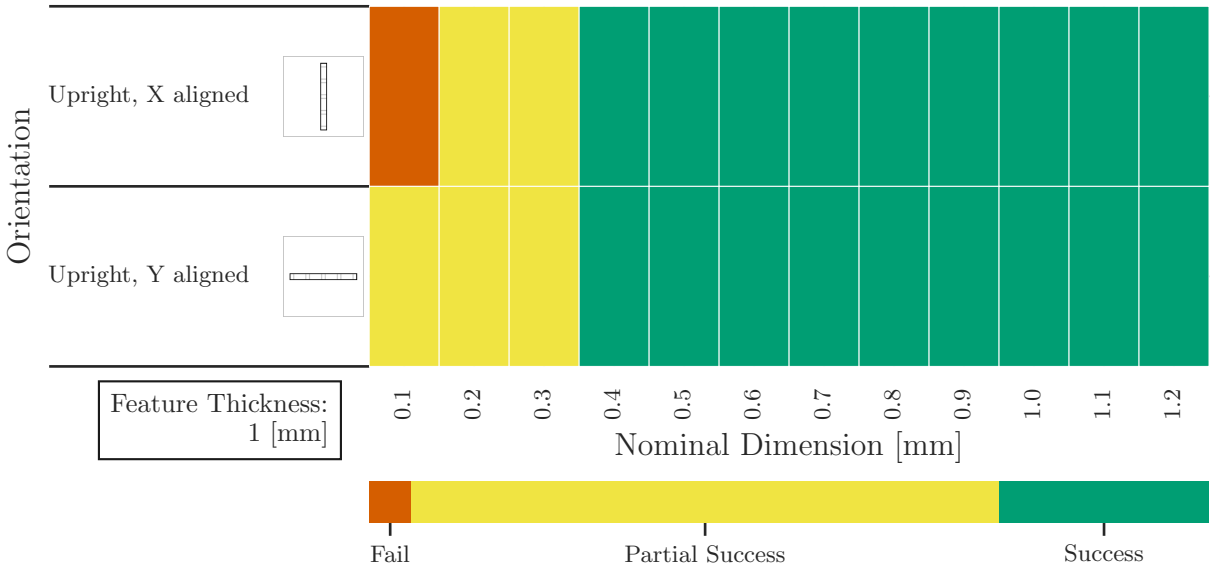


Figure 5.3: Degree of print success for vertical gap features with part thickness of 1 mm

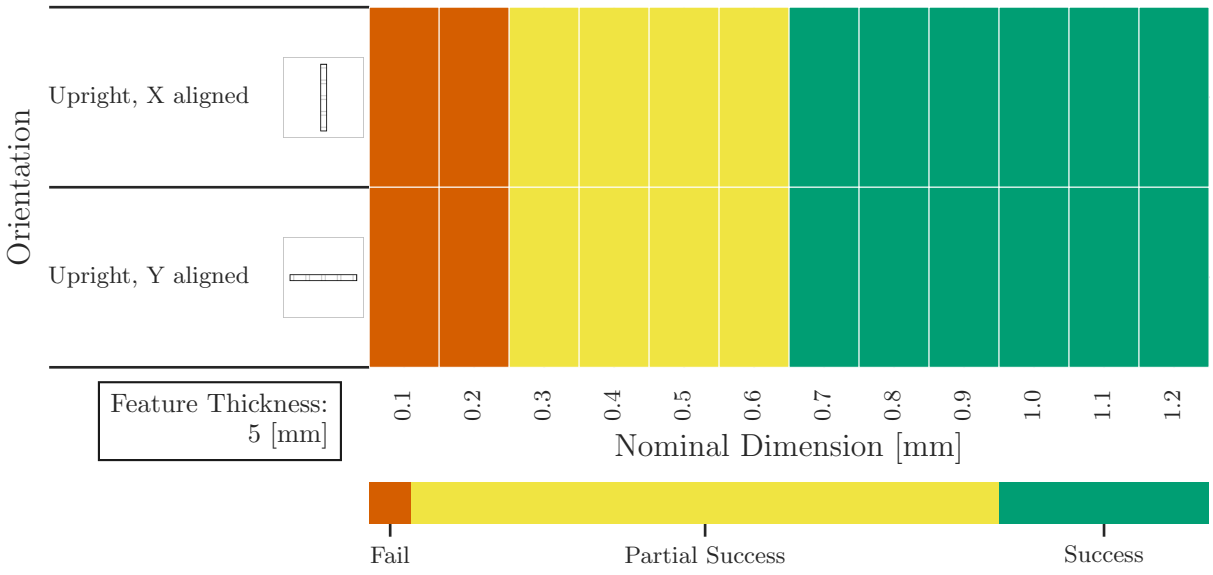


Figure 5.4: Degree of print success for vertical gap features with part thickness of 5 mm

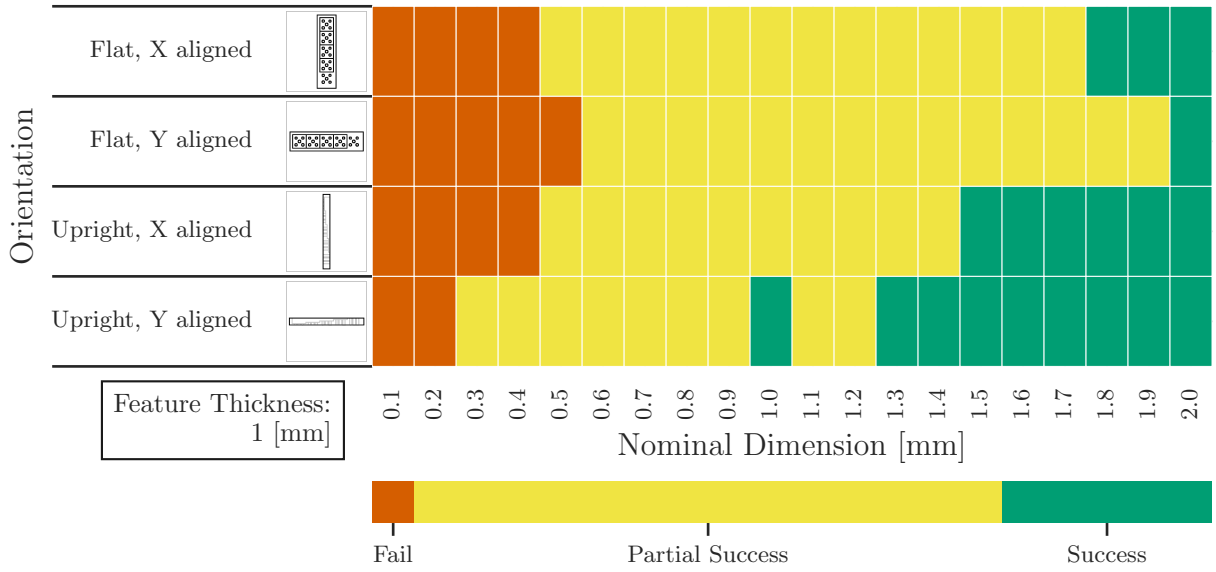


Figure 5.5: Degree of print success for through hole features with part thickness of 1 mm

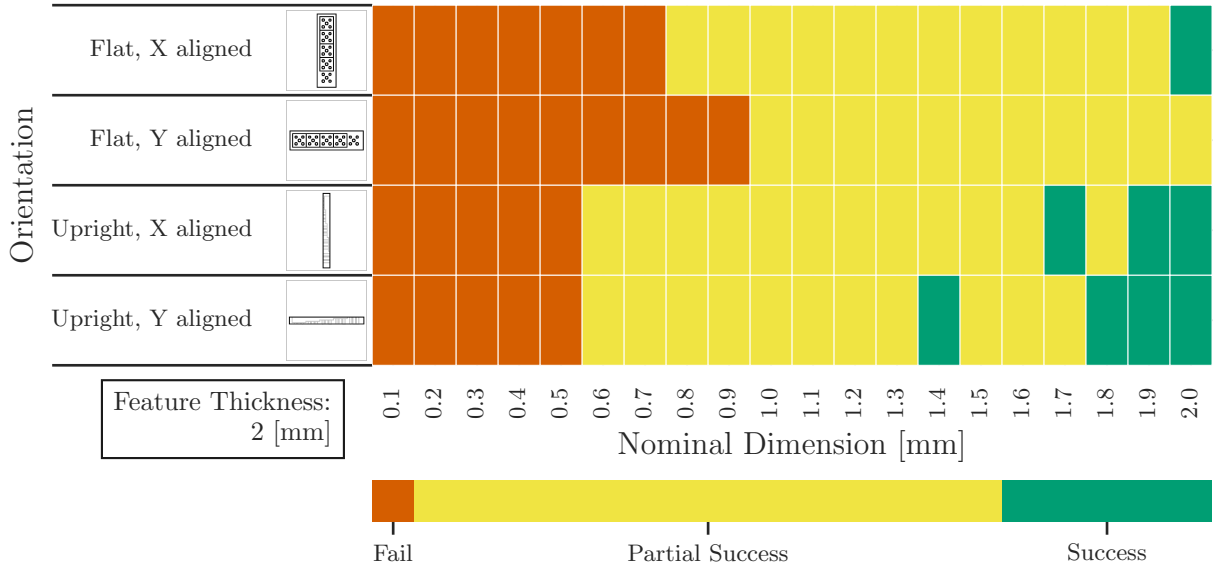


Figure 5.6: Degree of print success for through hole features with part thickness of 2 mm

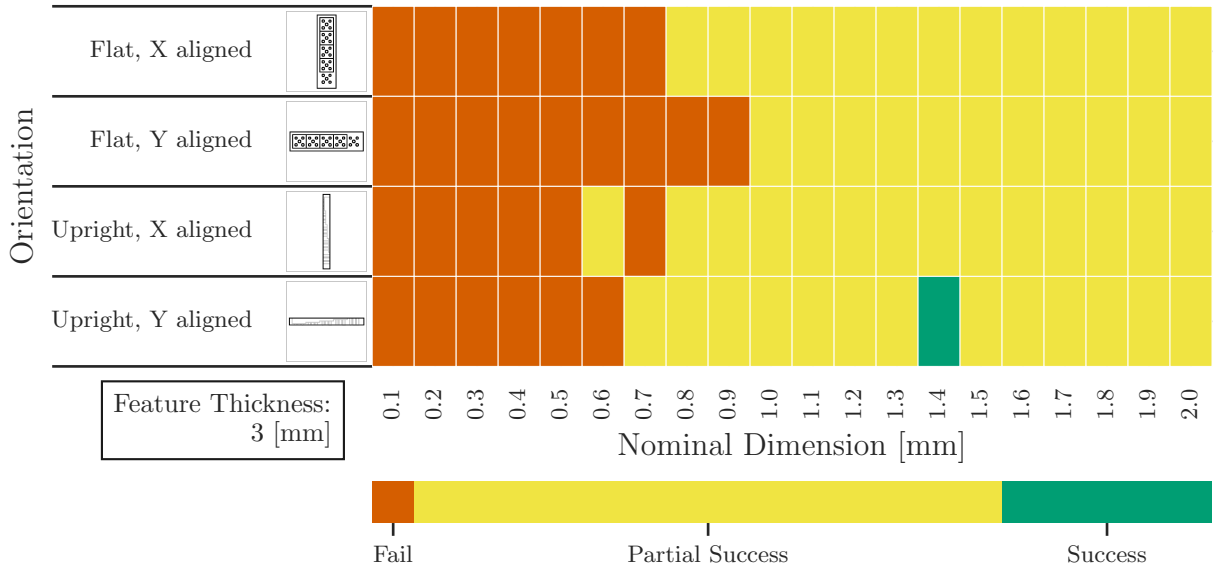


Figure 5.7: Degree of print success for through hole features with part thickness of 3 mm

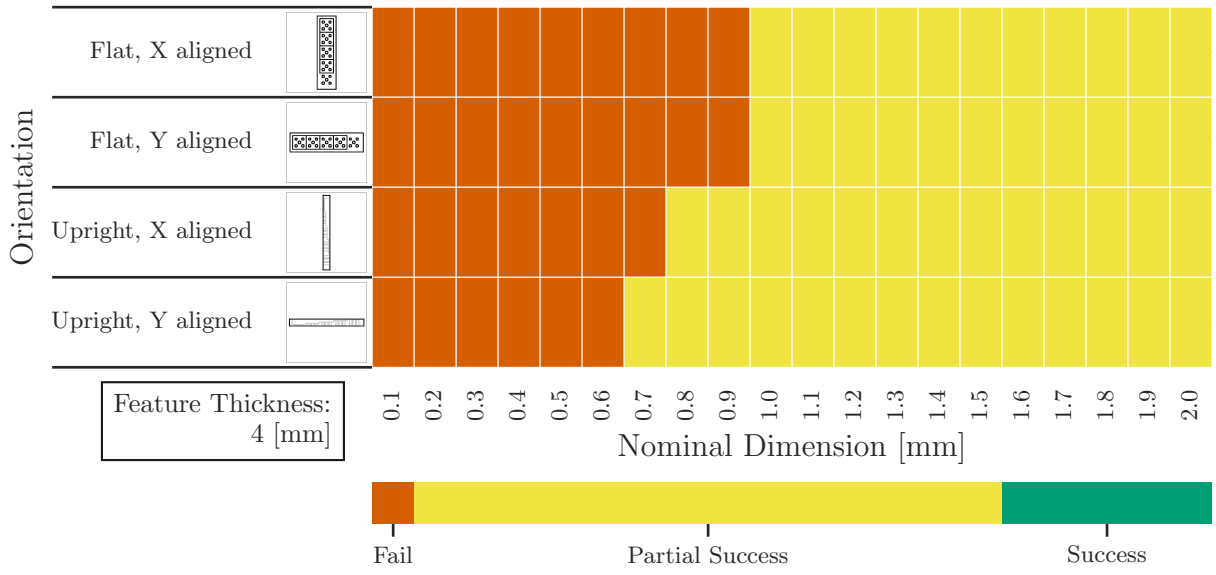


Figure 5.8: Degree of print success for through hole features with part thickness of 4 mm

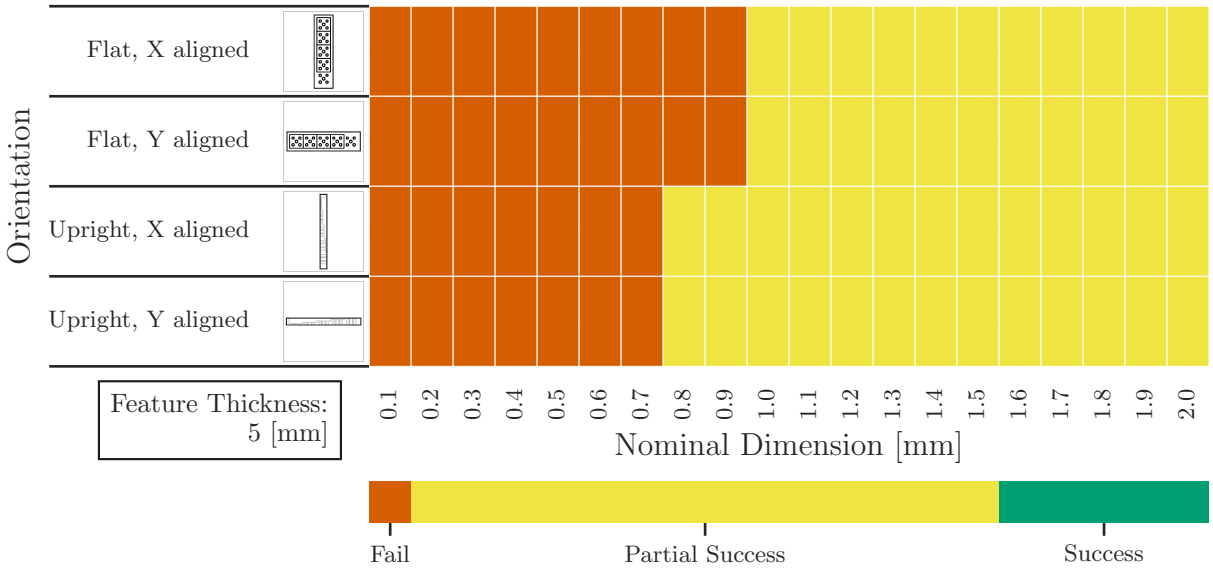


Figure 5.9: Degree of print success for through hole features with part thickness of 5 mm

5.2 Measured dimension and error

The next part of the analysis examined the measured dimension for each feature. This is the key part of the feature that will inform whether any adjustments should be made to designed parts prior to printing in order for them to have the desired dimension fidelity once manufactured. The measured dimension can be converted to a dimensional error following Equation 5.2, where E is the dimensional error, $D_{measured}$ is the measured dimension calculated using the method in section: Measured dimension and projection contour roughness from ROI, and $D_{nominal}$ is the nominal dimension that was used in the design file, described in chapter: Artifact design.

$$E = D_{measured} - D_{nominal} \tag{5.2}$$

In many cases, this adjustment can be a single offset constant that is added to critical dimensions to over/under size to counteract the error during manufacturing. This is only possible if the offset is consistent across the same feature printed multiple times. The adjustment could also be expressed as a function of the nominal dimensions, acting as a scaling factor that is dependent on the size of the geometry being printed. Linear regression was applied to determine whether the adjustment should be expressed as a constant offset or as a scaling factor. A constant offset can be desirable as it is simple to apply in practice and can be reasonably extrapolated to larger feature sizes, whereas a scaling factor can be automatically applied to the design prior to printing but can be prone to errors when extrapolated too far.

The thin wall features are analyzed to determine whether this error is dependent on the nominal dimension of the feature being printed. All thin wall features were printed with a constant part thickness of 5 mm. Figure 5.10 shows the relationship between the measured dimension, as described in Equation 4.1, of the part compared to the nominal designed

dimension used in the CAD model file. As expected, the two are correlated, however there is a positive offset from the ideal line which represents what would be seen if the manufactured parts were perfectly accurate. It is also observed that the orientation does not affect the dimension offset of this feature. Given that the slope of the points is roughly the same as the slope of the ideal line, it can also be inferred that the nominal dimension does not scale the dimensional error, rather it results in a constant offset. Indeed, these

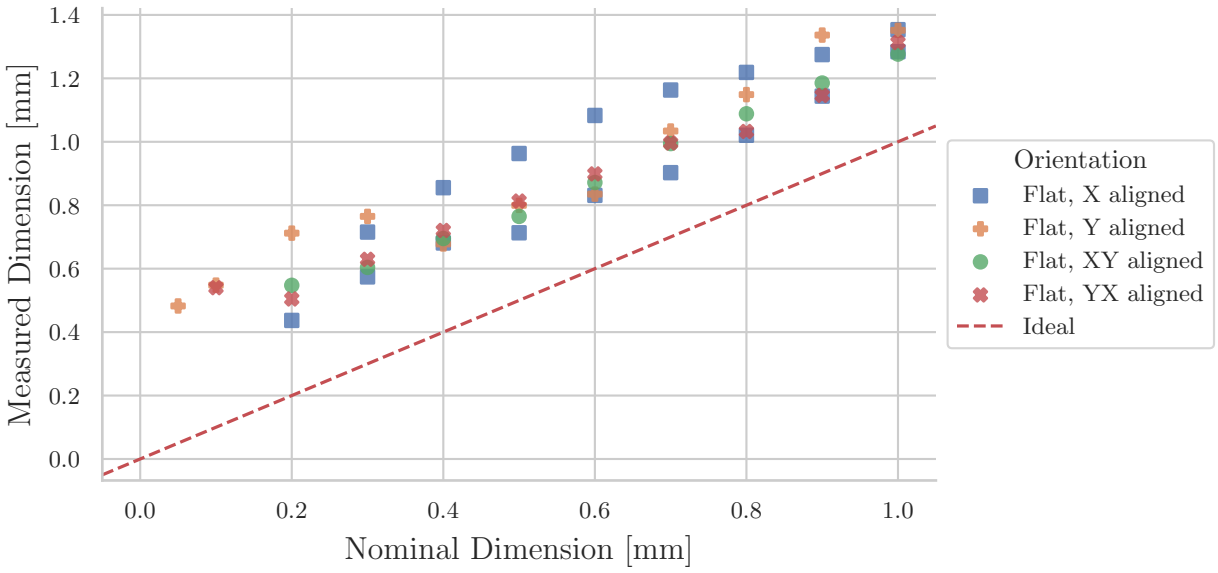


Figure 5.10: Measured dimension of thin wall features as calculated using Equation 4.1 plotted against their nominal dimension, categorized by orientation

relationships can be more clearly seen when looking at just dimensional error for these same specimens, compared against nominal dimension as seen in Figure 5.11. These observations were confirmed using a linear regression to test the significance of orientation and nominal dimension as regressors for measured error at ($p < 0.05$). So, for a thin wall feature, dimensional error can be modeled as a constant value independent of nominal dimension or orientation and has been calculated to be $E_{tw} = 0.329$ mm, $\sigma = 0.082$ mm.

A constant value for dimensional error is consistent with the working method of binder jetting, as the geometry is defined by the portions of powder that are held together with binder deposited during the printing process. As each droplet of binder is deposited onto the surface of the powder bed, the binder infiltrates the porous powder bed, spreading both laterally along the X-Y plane and penetrating downwards in the Z direction. As reported by Bai et al. the lateral spreading of binder in a powder bed is roughly three times greater than the penetration depth [95]. Given that the measured dimensions of these features are strictly on the X-Y plane, this lateral spreading is the dominant cause of dimensional error. The saturation value from the process parameters determines the quantity of binder that is dispensed per area, which in turn affects the distance that each drop spreads upon contact with the powder bed. If this saturation value is too high and the heat lamp is not able to mitigate the excess water content via evaporation, then the excess binder liquid will spread further than expected, causing the shape of the specimen to expand outwards [67], [94]. Indeed, it was observed by Miyanaji et al. that geometric fidelity in the X-Y plane was significantly affected by binder saturation [93]. This effect is most apparent along the edges of the part, but is likely not affected by excess binder within the interior of the part, as the binder cannot easily migrate large distances. Therefore, for constant part thickness, this outwards expansion is not dependent on the nominal size of the geometric feature (thin wall dimension) and is primarily driven by the behaviour of the binder at the edge of the part, which can be described by the constant dimension error found above. If the part thickness is increased, the calculated error is expected to be different, as hinted by the results captured in in Figures 5.5 to 5.9.

For the thin gap feature, the same approach can be taken as for the thin wall feature, as can be seen in Figure 5.12. The data follows the same patterns, with the only difference being that the error is now negative rather than positive, as seen in Figure 5.13, showing a

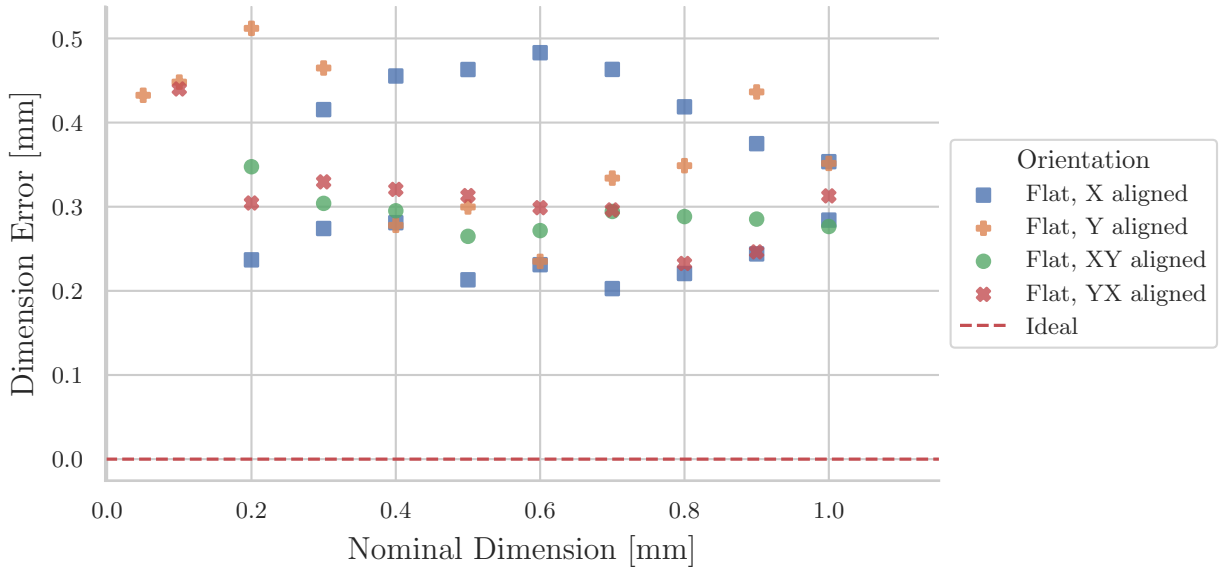


Figure 5.11: Dimensional error of thin wall features as calculated using Equation 5.2 plotted against their nominal dimension, categorized by orientation

propensity of thin gaps to be undersized, while the material surrounding them is oversized. This is due to the thin gap feature being a negative feature, thus the tendency of the binder jetting process to produce parts with excess material due to binder imbibition leads to oversized positive features and undersized negative features. The dimensional error for this feature was found to be $E_{tg} = -0.366$ mm, $\sigma = 0.079$ mm.

Examining the vertical gap feature class, the features were printed with different part thicknesses (1 mm and 5 mm), which must also be considered as a possible regressor for the dimensional error. The part thickness is the thickness of the part that includes the feature, as measured orthogonal to the nominal dimension. As with the thin wall and thin gap features, the features have dimensions correlated to nominal dimension, shown in Figure 5.14. The effect of thickness on error can be seen in Figure 5.15. A stepwise regression technique was used to build a model that accounted for variables with significant effects

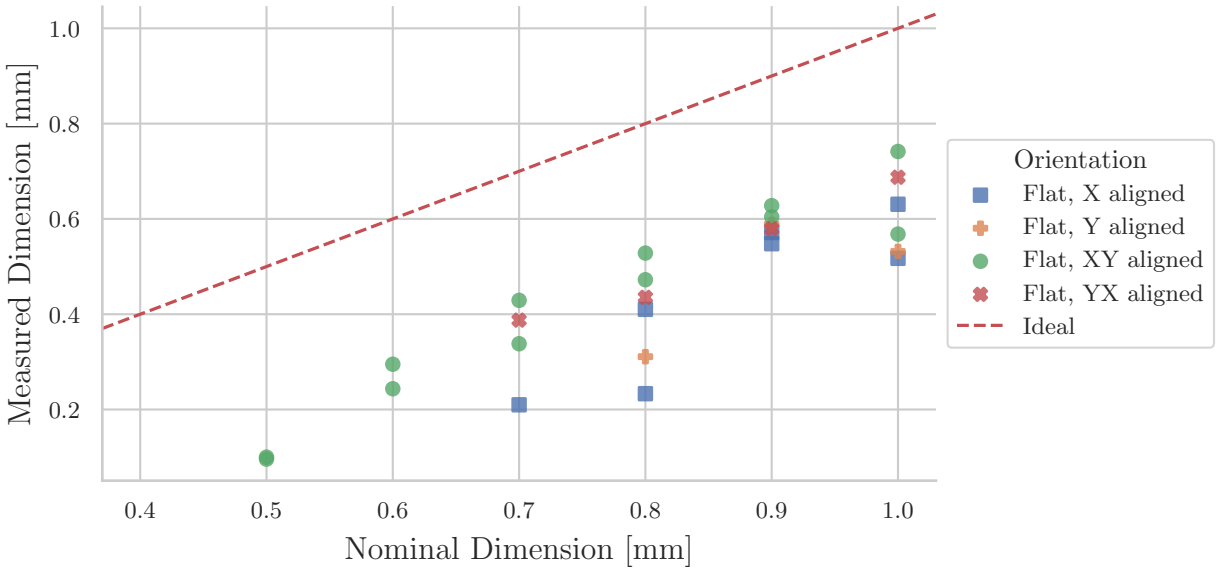


Figure 5.12: Measured dimension of thin gap features as calculated using Equation 4.1 plotted against their nominal dimension, categorized by orientation

[96]. This results in the model shown in Figure 5.16, where it was determined that the part thickness and nominal dimension are the relevant factors that determine the degree of dimensional error and orientation does not play a significant role in the geometric accuracy of this feature.

In this case, the error is dependent on the nominal dimension of the feature and the part thickness, as can be described by Equation 5.3, where E_{vg} is the dimensional error, $t_{feature}$ is the part thickness and $d_{feature}$ is the nominal dimension of the feature, all in mm. It is notable that the error model for this feature predicts zero error for a certain nominal dimension for a given part thickness.

$$E_{vg} = -0.0356\ t_{feature} + 0.1532\ d_{feature} - 0.0439 \tag{5.3}$$

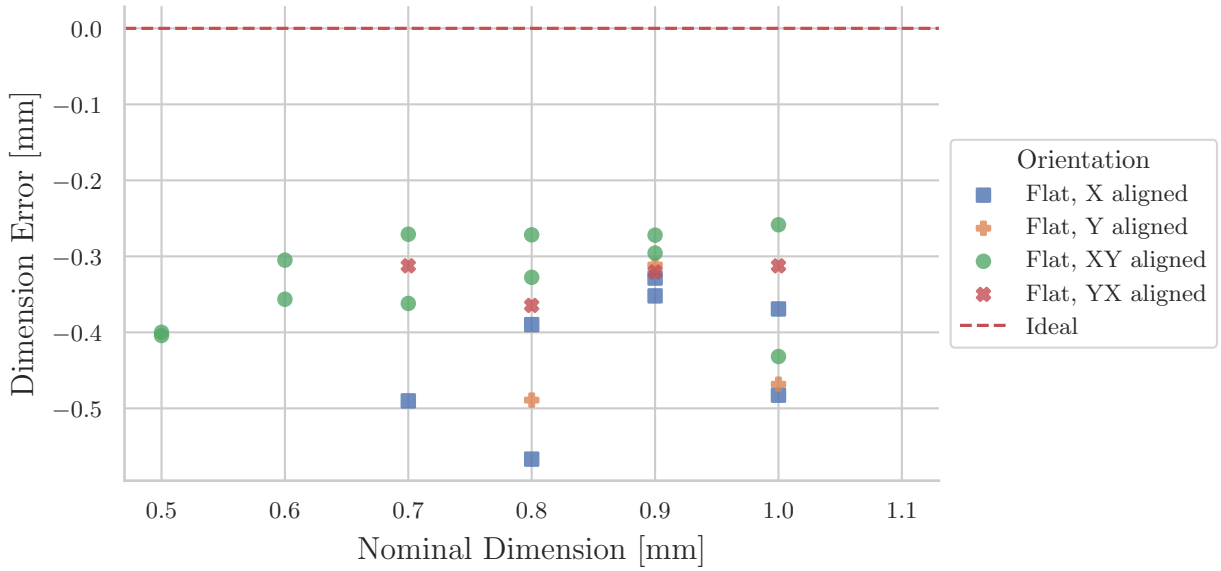


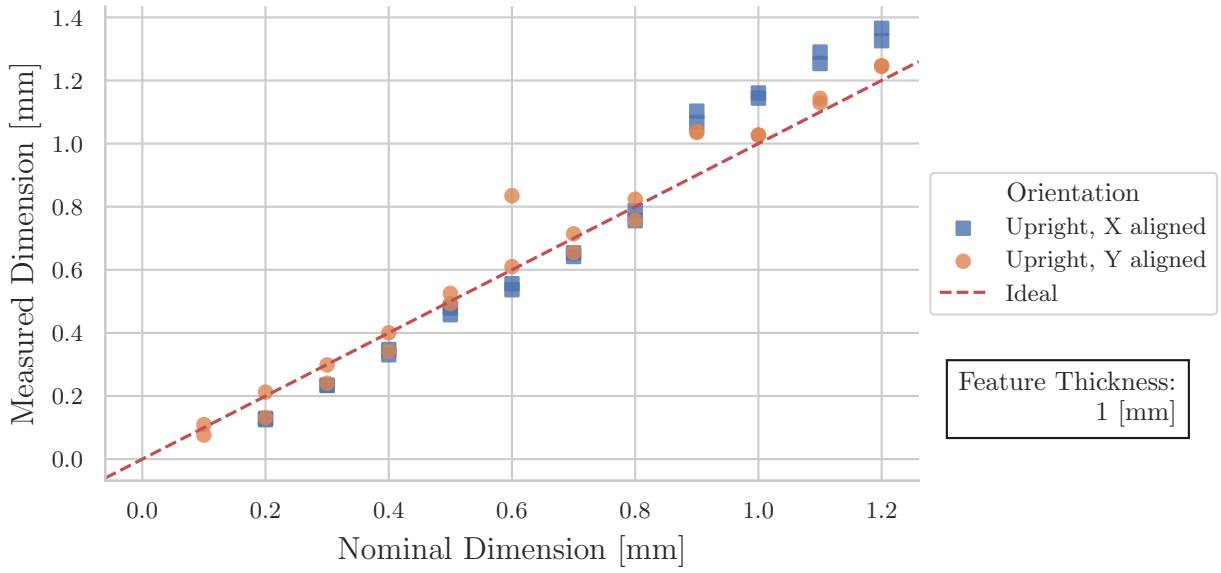
Figure 5.13: Dimensional error of thin gap features as calculated using Equation 5.2 plotted against their nominal dimension, categorized by orientation

Finally, looking at the through hole feature, when lumping all the different part thickness levels into a single data set, no clear relationship between dimensional error and nominal dimension can be seen in Figure 5.17. Reorganizing the data to lump by nominal dimension reveals that the dimensional error is dependent on part thickness and orientation, as seen in Figure 5.18, where the error tends to globally increase as the part thickness increases, while keeping the through hole nominal dimension constant. These trends can be separately seen in Figure 5.19 where the effect of orientation is quantified, with parts printed in the "Flat, Y aligned" orientation having the worst performance and 5.20 where the effect of thickness indicates that the higher the thickness, the greater chance of occlusion of small features. The results for through hole features at different part thickness are combined into a linear regression as seen in Figure 5.21. The model is expressed in Equation 5.4, where $t_{feature}$ is the part thickness, and $O_{orientation}$ represents the indicator

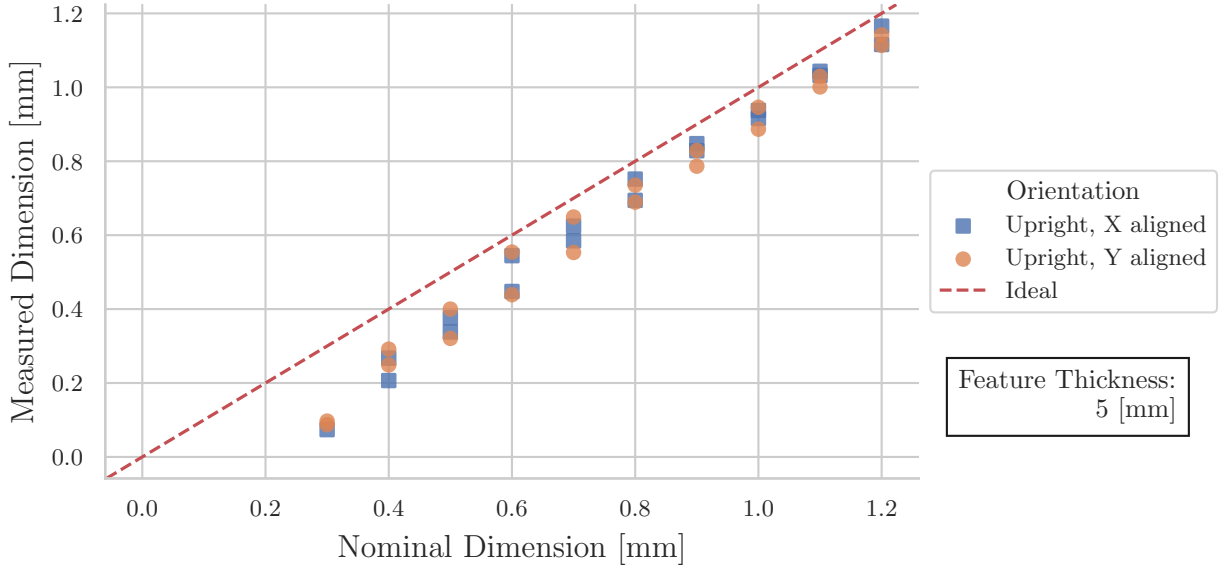
variable for each given orientation, taking the Flat, X aligned orientation as the default condition. This linear regression model can now be applied to determine appropriate compensation factors to improve geometric accuracy of through hole features, a process which will be discussed further in Section 5.7. The effect of orientation on curved surfaces such as holes has been discussed with respect to the stair stepping effect, where the layer-wise nature of BJAM can limit the resolution of curves in certain orientations, particularly when trying to reproduce a shallow slope relative to the X-Y plane [97].

$$E_{th} = -0.0485\ d_{feature} - 0.0728\ O_{Flat,Y} + 0.0627\ O_{Up,X} + 0.1097\ O_{Up,Y} - 0.2087 \quad (5.4)$$

For the through hole feature, there appears to be a difference in the Flat, X aligned and Flat, Y aligned orientations for the dimensional error. This is unusual as the hole feature should be equally affected by the powder spreading and printhead jetting directions in these two orientations. Looking at the way these parts were printed in the build volume, a confounding factor was discovered in that the specimens in the Flat, Y orientation were printed on the bottom layer of the print volume whereas the Flat, X orientation specimens were printed above on the upper layer. This may explain the difference in dimensional accuracy observed in Figure 5.22. One cause may be the printing parameters for the binder jetting machine which automatically attempts to compensate for excess bider on the initial layers of the print by reducing the saturation for the first few layers. Since it is theorized that binder saturation [66] is largely responsible for the geometric accuracy of printed parts, this is a plausible explanation. Additionally, the effect of the heater on the overall increase in powder bed temperature as the layers are stacked can be a compounding factor in the amount of binder evaporation, thus influencing dimensional fidelity [94]. More work should be carried out to examine the effect of placement within the print volume and effect of heater power on specimen dimensional accuracy, as this appears to be an influencing factor.



(a)



(b)

Figure 5.14: Measured dimension of vertical gap features as calculated by Equation 4.1, plotted against their nominal dimension, categorized by orientation, for part thickness: (a) 1 mm; and (b) 5 mm.

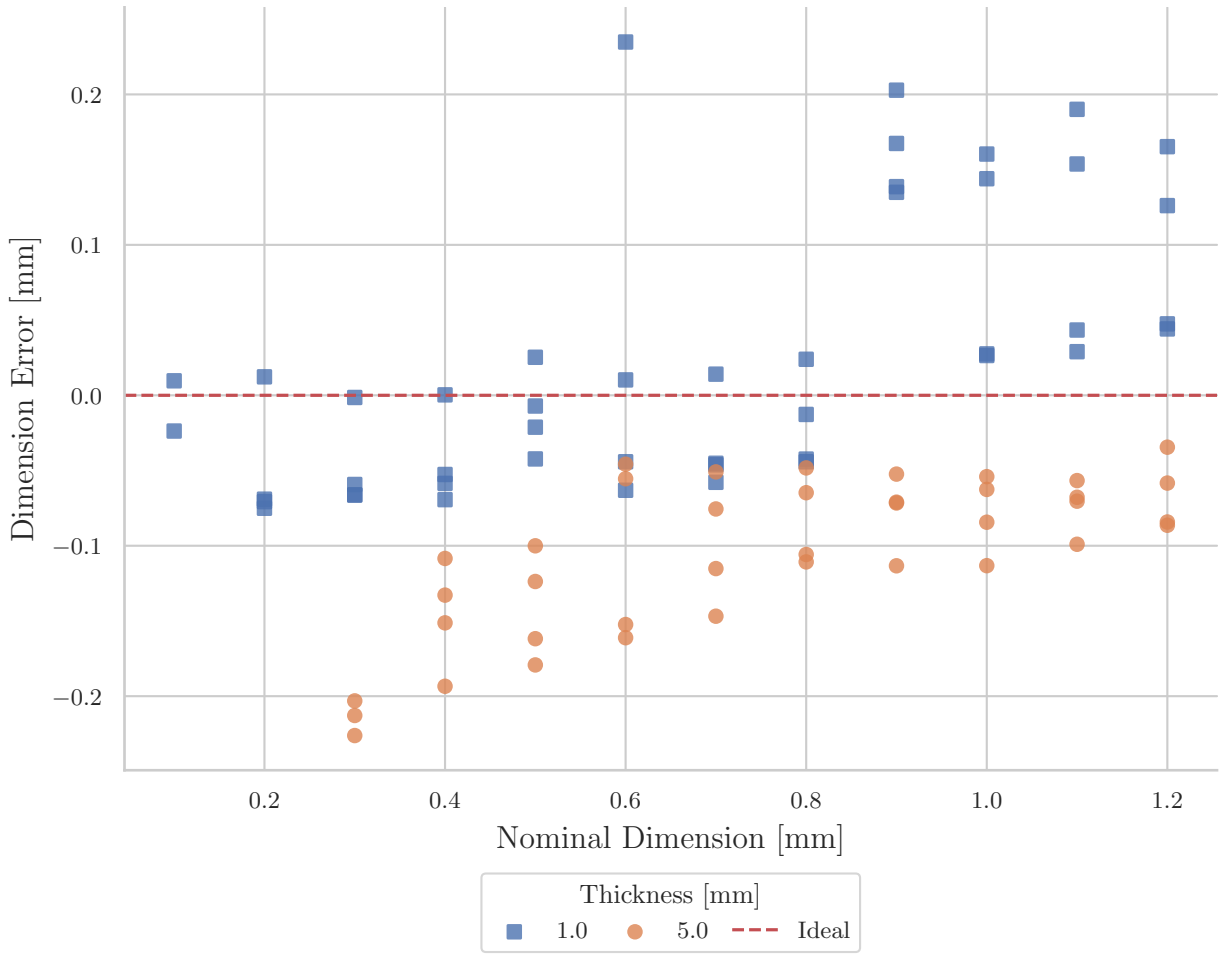


Figure 5.15: Dimensional error of vertical gap features for all orientations, as calculated using Equation 5.2, plotted against their nominal dimension, categorized by part thickness.

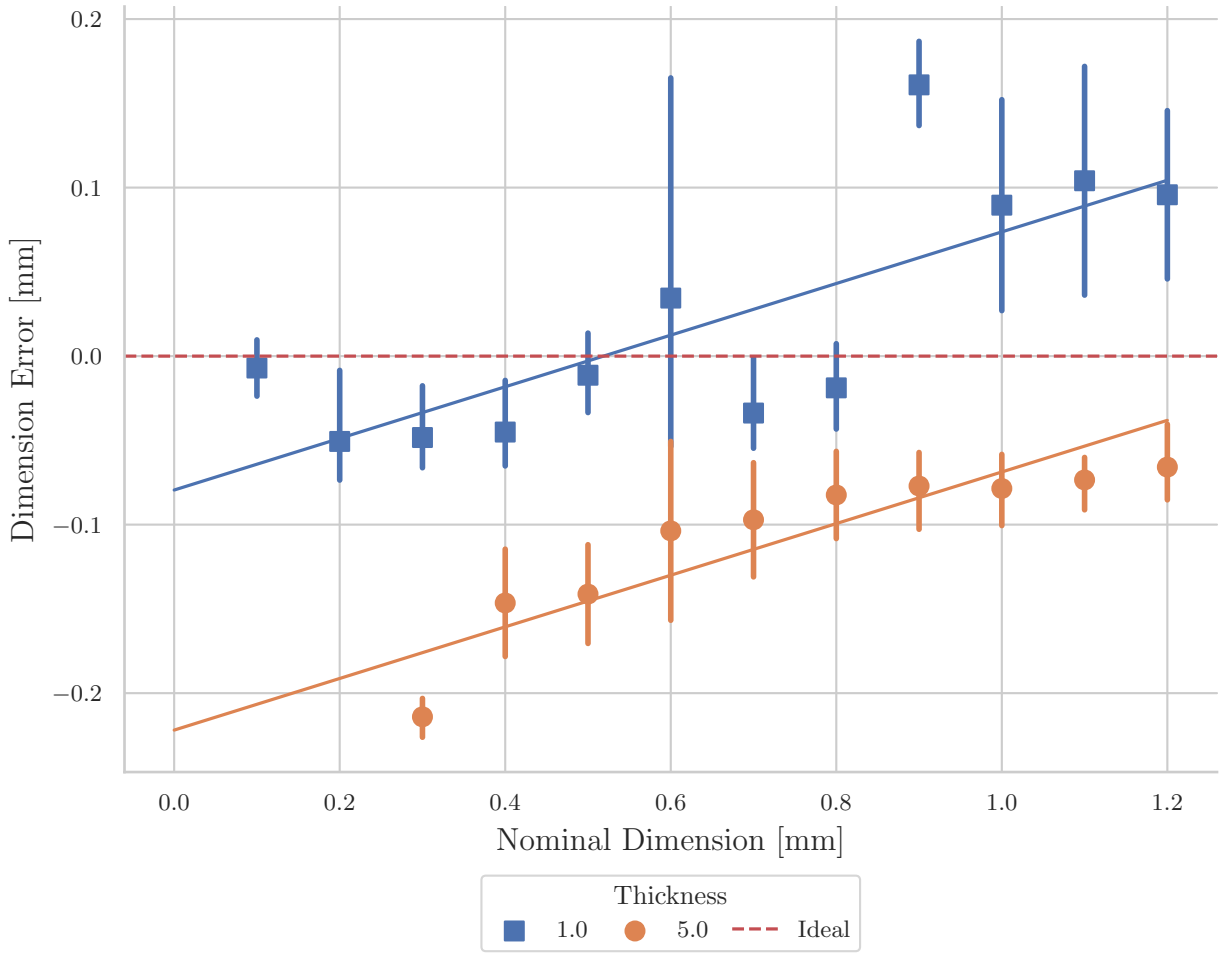


Figure 5.16: Dimensional error of vertical gap features for all orientations, plotted against their nominal dimension, categorized by part thickness. Error bars correspond to 95% confidence interval and the lines represent the linear regression evaluated for each part thickness.

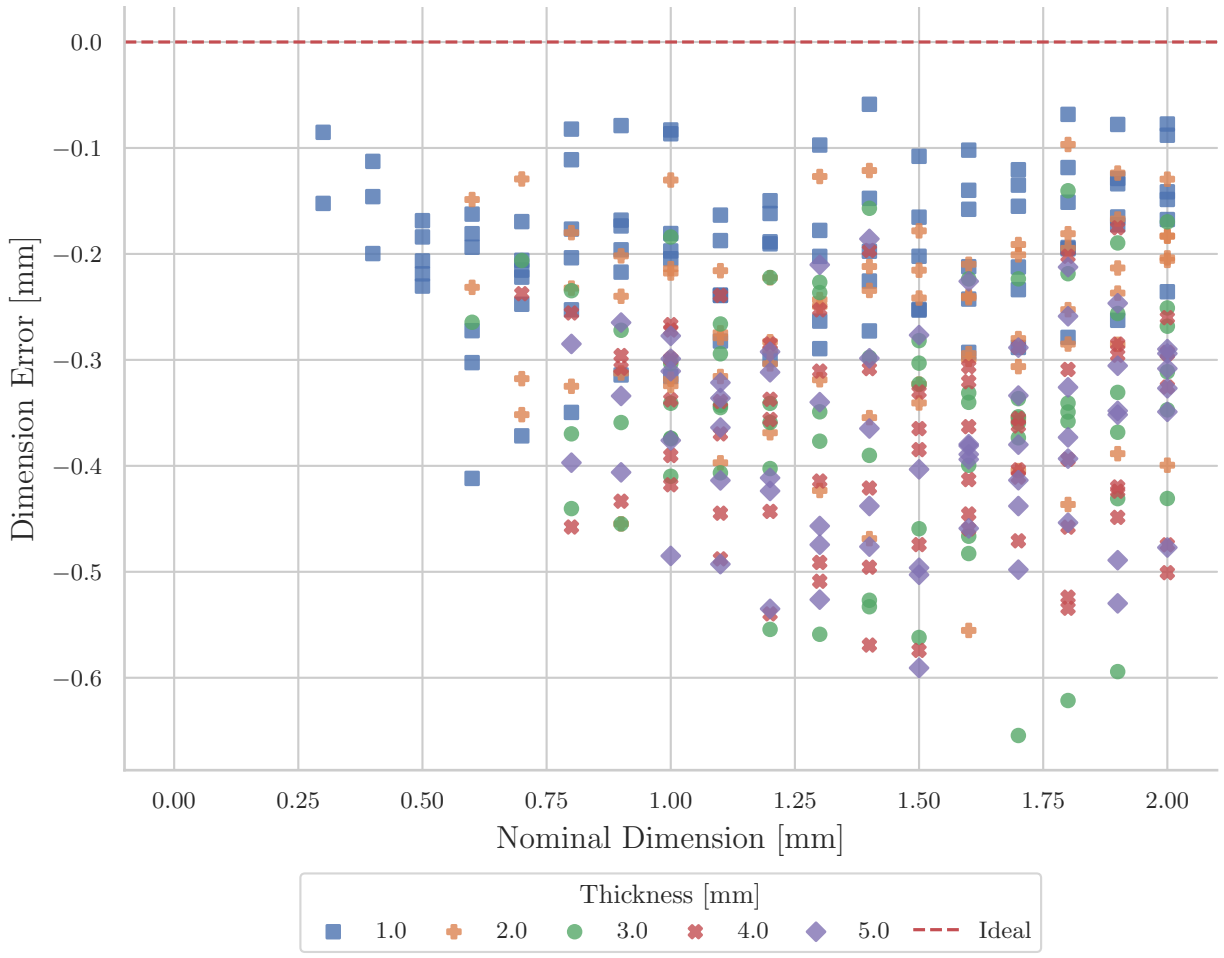


Figure 5.17: Dimensional error of through hole features for all orientations, as calculated using Equation 5.2, plotted against their nominal dimension, categorized by part thickness

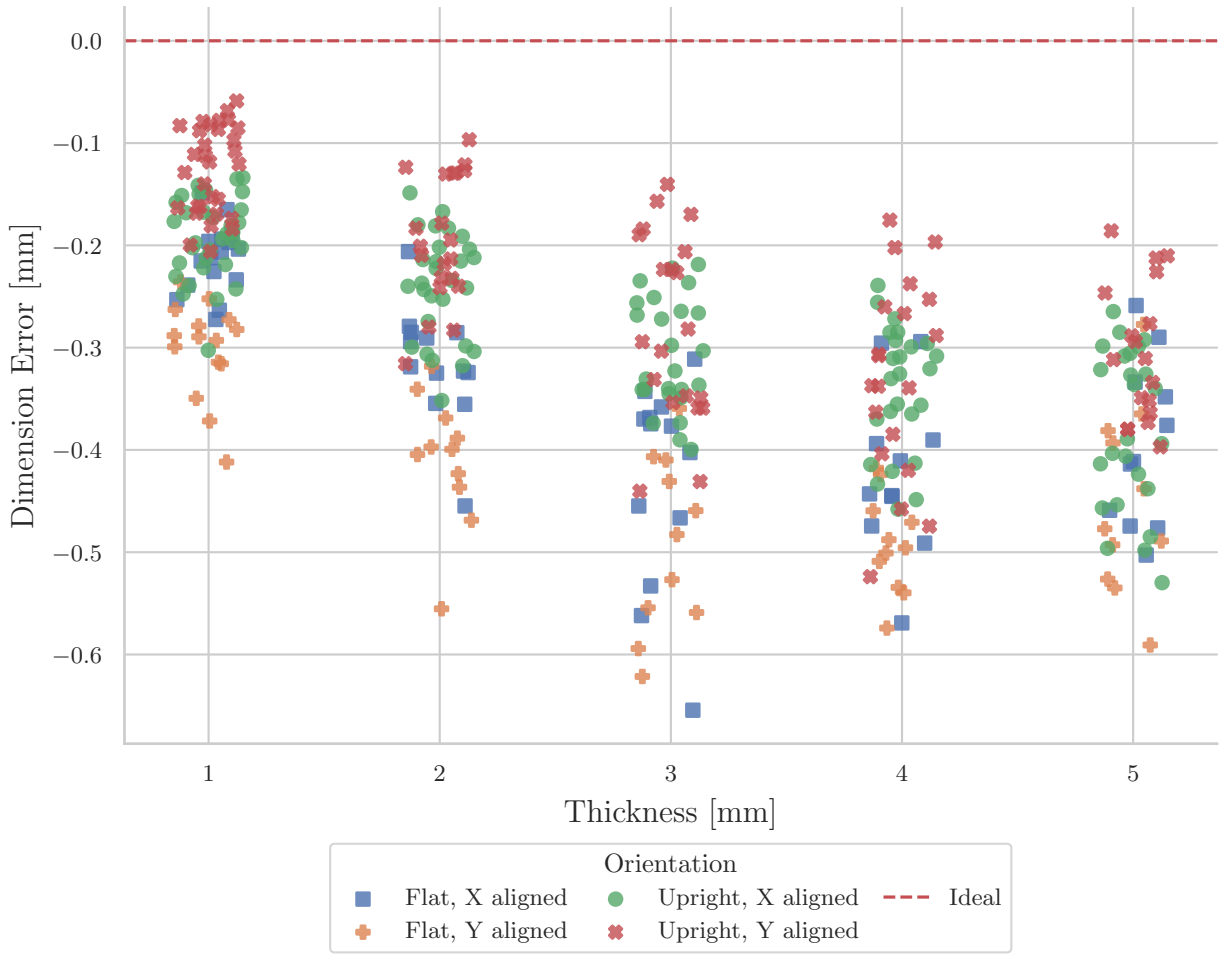


Figure 5.18: Dimensional error of through hole features for all nominal dimensions, as calculated using Equation 5.2, plotted against their part thickness, categorized by orientation

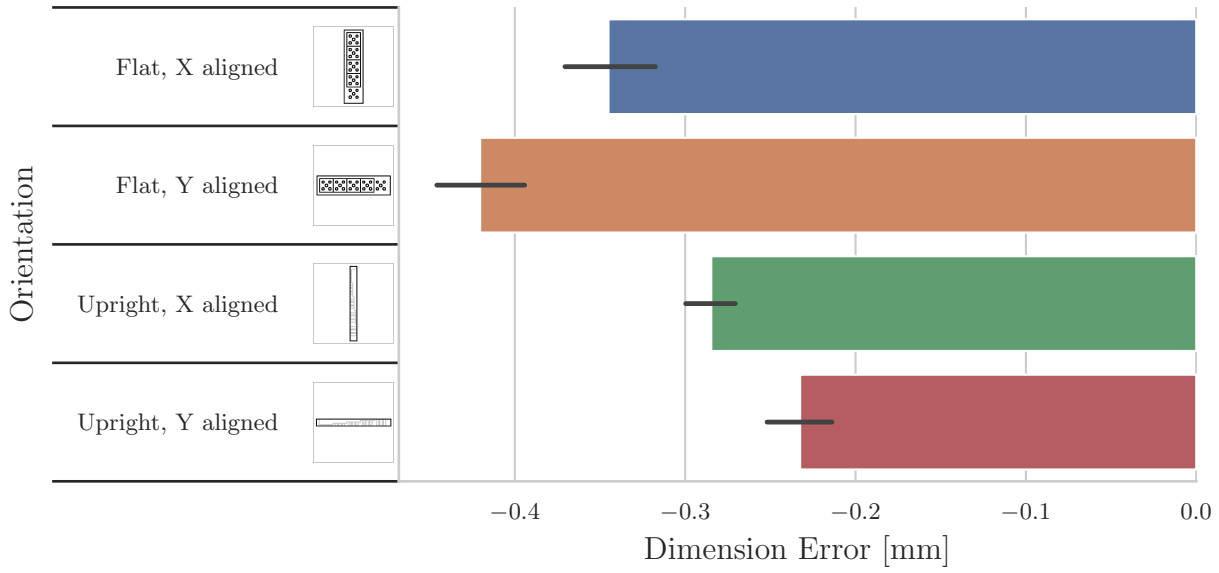


Figure 5.19: Effect of orientation on dimensional error averaged across all part thicknesses and nominal dimensions of through hole features as calculated using Equation 5.2. Error bars correspond to 95% confidence interval.

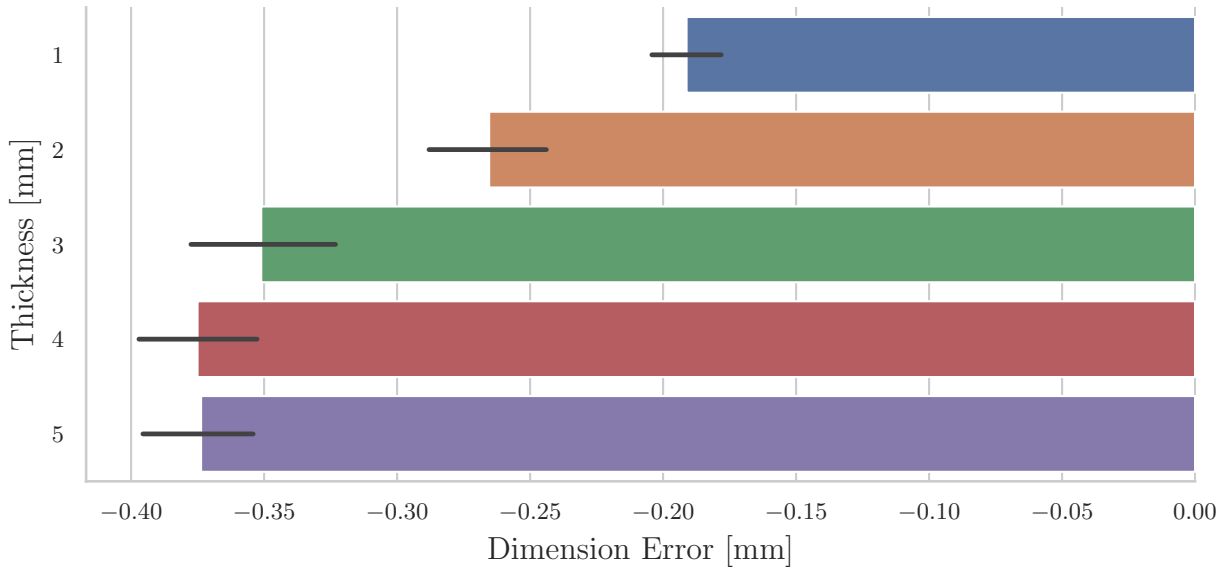


Figure 5.20: Effect of part thickness on dimensional error averaged across all orientations and nominal dimensions of through hole features as calculated using Equation 5.2. Error bars correspond to 95% confidence interval.

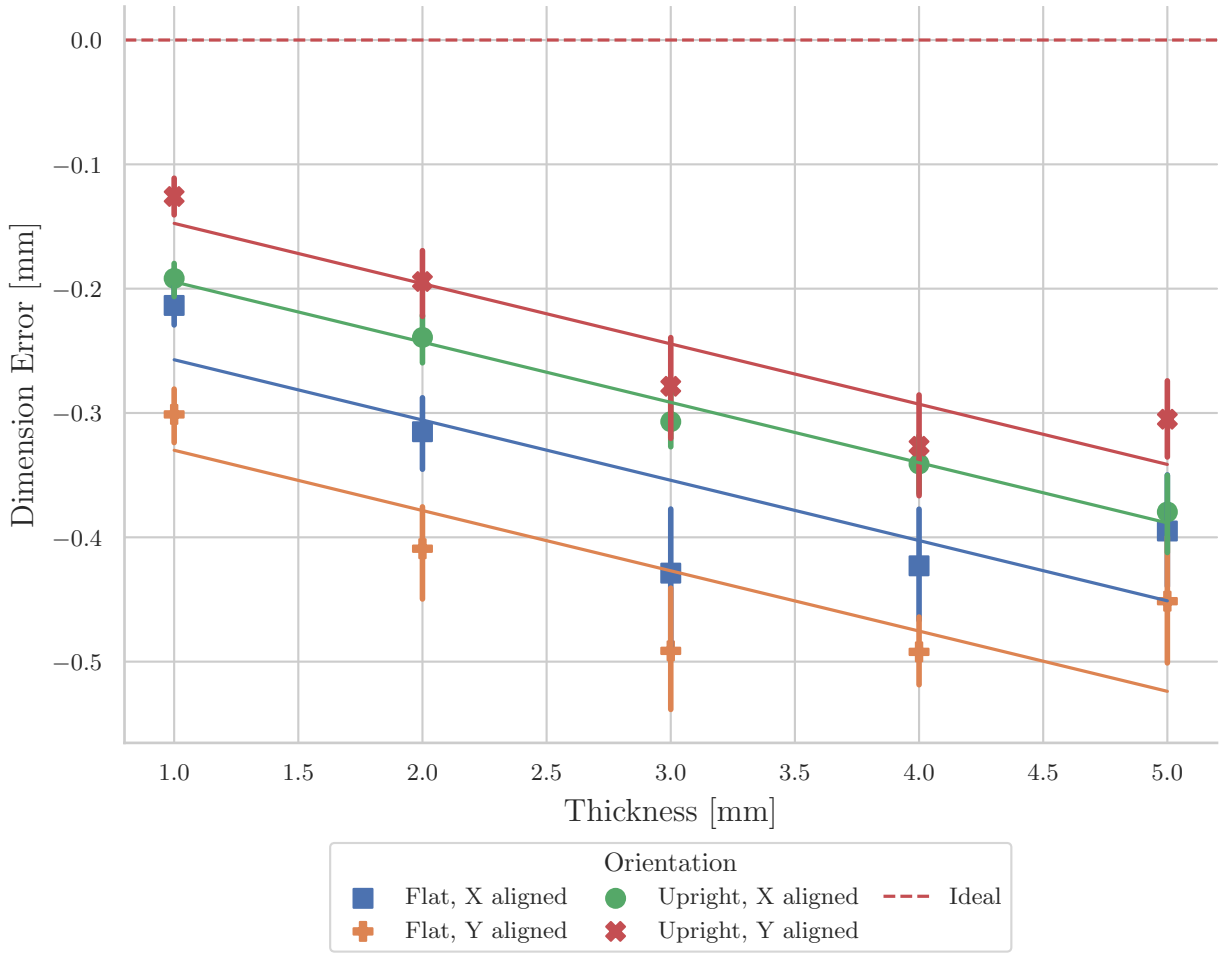


Figure 5.21: Dimensional error of through hole features for all nominal dimensions, plotted against their part thickness, categorized by orientation. Error bars correspond to 95% confidence interval and the lines represent the linear regression evaluated for each part thickness.

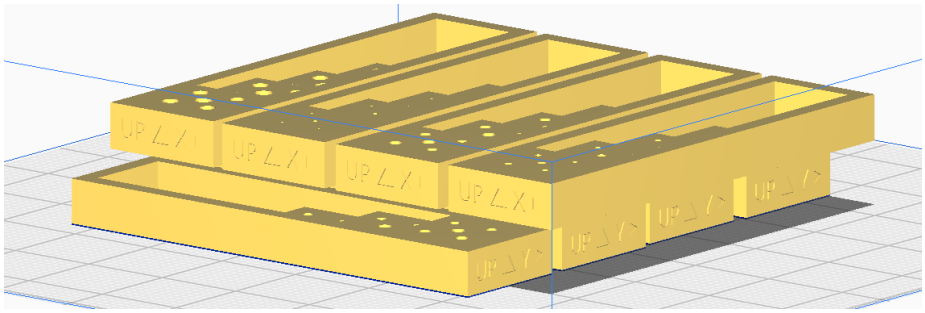


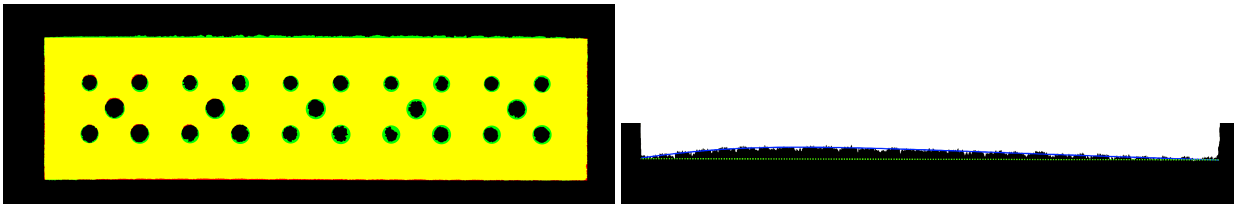
Figure 5.22: The build layout used to print a subset of through hole specimens, where the parts with "Flat, X aligned" orientations are stacked on top of the ones with "Flat, Y aligned" orientations, with sufficient vertical clearance.

5.3 Overprint and underprint areas

Underprint was rarely observed for all geometric features observed in this study. This is consistent with the observation that most parts have been experiencing excessive material, with larger dimensions for positive features and smaller dimensions for negative features respectively. One instance of severe underprint was observed in the data, but with closer examination of the underlying parts revealed that the underprint was being falsely measured due to a print that was warped and thus was not being correctly aligned with the sliced CAD image during the computer vision process. The comparison of this part with the CAD can be seen in Figure 5.23a. Despite a good alignment with the four corners of the part, the bottom edge of the part is bowed and can be seen deviating from the ideal line from the sliced CAD image. This misalignment is what led to a higher apparent underprint area despite not actually having significant underprinting issues. It can be noted that this is a drawback of the computer vision approach that will need to be considered in future work to either mitigate or avoid this.

The warping is likely to have been caused by the friction between the side of the build chamber and the powder bed as it moves downwards, as visualized in Figure 5.24. The powder that is contact with the wall will experience friction that opposes movement, causing an uneven movement of powder that results in this warping. Thus, the distance from the side of the print volume is also an important consideration when preparing parts for printing.

Overprint gives more information about the quality of parts once they are printed. From the earlier section, it is understood that the measured dimension of a part will be offset from the designed nominal dimension of the part. The overprint can be used to examine more closely how these enlarged dimensions affect the quality of the printed part.



(a) (b)

Figure 5.23: Warping observations in a through hole feature specimen. (a) Warping seen with through hole specimen, the top and bottom edges do not align with the CAD model and have overprint and underprint resepectively. (b) Amplified contour of warping behaviour seen along bottom edge of part in (a), where the part contour curves upwards and does not follow the designed straight edge

For thin wall and thin gap features, no significant relationship between overprint and nominal dimension or orientation could be determined through linear regression; rather, a constant offset can be applied to these features. This is consistent with the remarks made when examining dimensional error, as the saturation of the binder causes a constant amount of imbibition along the straight edge of the feature for parts with constant thickness. It is hypothesized that for parts with a greater part thickness, they may experience greater overprint due higher likelihood of binder spreading further out at some point as the part is printed. Because overprint is measured in this work from a two-dimensional flattening of a part, compounding the cross-sectional area though the height of the part, any excess material at each layer height can contribute to overprint. Given a large enough part thickness, it is expected that this overprint measure will plateau at a maximum as the stochastic behaviour of binder spreading reaches its limit and the binder cannot spread any further away from the edge.

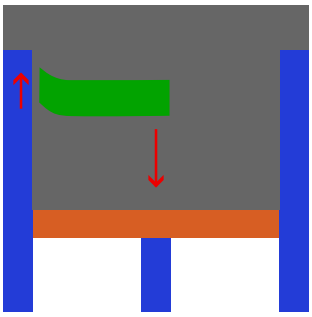


Figure 5.24: Exaggerated view of how part proximity to build volume wall during printing can lead to warping, where the arrows represent the forces acting on the powder bed as the build bed moves down

With regards to the through hole feature printed at different part thickness levels, a linear regression indicated that nominal dimension, orientation, and part thickness are all significant regressors for the square root of overprint area. This transformation for the overprint area was determined to have a good fit for the data. This regression is expressed in Equation 5.5, where A_{op} is the overprint area in mm^2, $t_{feature}$ is the part thickness, $d_{feature}$ is the nominal dimension, and $O_{orientation}$ represents the indicator variable for each given orientation, taking the Flat, X aligned orientation as the default condition.

$$\sqrt{A_{op}} = 0.0561\, t_{feature} + 0.2885\, d_{feature} + 0.0793\, O_{Flat,Y} - 0.0657\, O_{Up,X} - 0.1133\, O_{Up,Y} + 0.2431 \tag{5.5}$$

The square root transformation suggests that the overprint area scales non-linearly with the variables examined. If a compensation factor is desired for through hole features to increase geometric fidelity, then Equation 5.4 stated earlier is recommended as a starting point and Equation 5.5 can be used afterwards to predict the amount of overprint and check if it would be acceptable. It is theorized that the relationship to nominal dimension is due to the overprint being proportional to the total edge perimeter that forms the feature, and

for the case of a through hole, the perimeter of the hole is proportional to its diameter. Another explanation for this is due to the increased curvature of small diameter holes, this reduces the effectiveness of depowdering as powder is more likely to get stuck as the nominal dimension decreases. A similar effect was observed in other studies, where internal corners that were in sharp in design became rounded once printed [6].

5.4 Projection contour roughness

No significant correlation was found between projection contour roughness and nominal dimension, orientation, or part thickness for thin wall, thin gap, vertical gap, or through hole features. A full linear correlation with all possible regressors and their interaction effects was performed for each partial or fully successful feature and their R^2 values are tabulated in Table 5.2 [96]. As indicated by their low R^2 values, these models are poor fits for the data. Other transformations also did not yield any significant relationships to the data.

Table 5.2: Table containing the goodness of fit as calculated using R^2 for each full linear regression used to try modelling projection contour roughness of each feature.

Feature type	R^2
Thin wall	0.440
Thin gap	0.573
Vertical gap	0.272
Through hole	0.286

This measure is highly dependent on the roughness of the edges of features, which in turn is largely driven by the powder characteristics. This is apparent when looking at Figure 5.25, where the variations at the edge of the feature are on the same scale as the powder diameter. This observation indicates that this measure may not be a good metric for comparing feature quality for green binder jetted parts that have been manufactured using the same powder feedstock. It is possible that this metric can provide insights when comparing parts made from different powder materials or sizes. This measure is also worth considering as a method of comparing the change in roughness after densification of fully sintered parts to green parts.

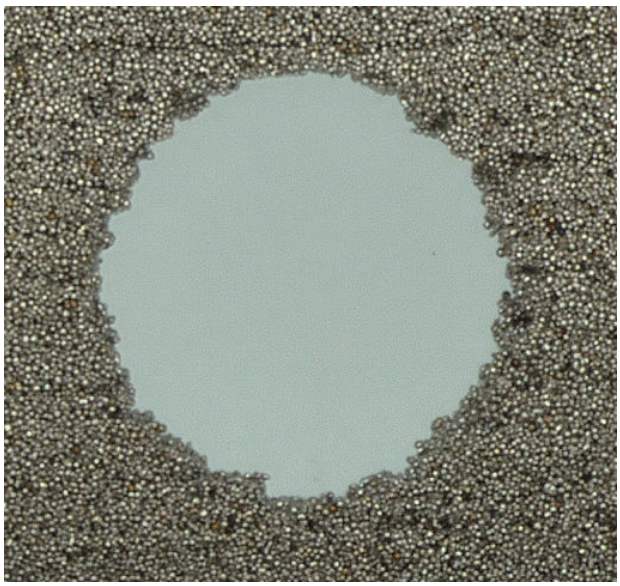


Figure 5.25: Close-up view of a through hole feature showing the powder along the edges of the parts and how projection contour roughness is determined by the number and size of powder agglomerations.

5.5 Clearance between solid volumes

The clearance cylinder artifacts reveal some information about the minimum clearance required between parts that are designed to be separable. The inner cylinders were attempted to be removed during the depowdering process, using gentle force. Figure 5.26 shows one of the specimens with its cylinders removed. This type of study is important in determining the appropriate clearance between two volumes in assemblies.

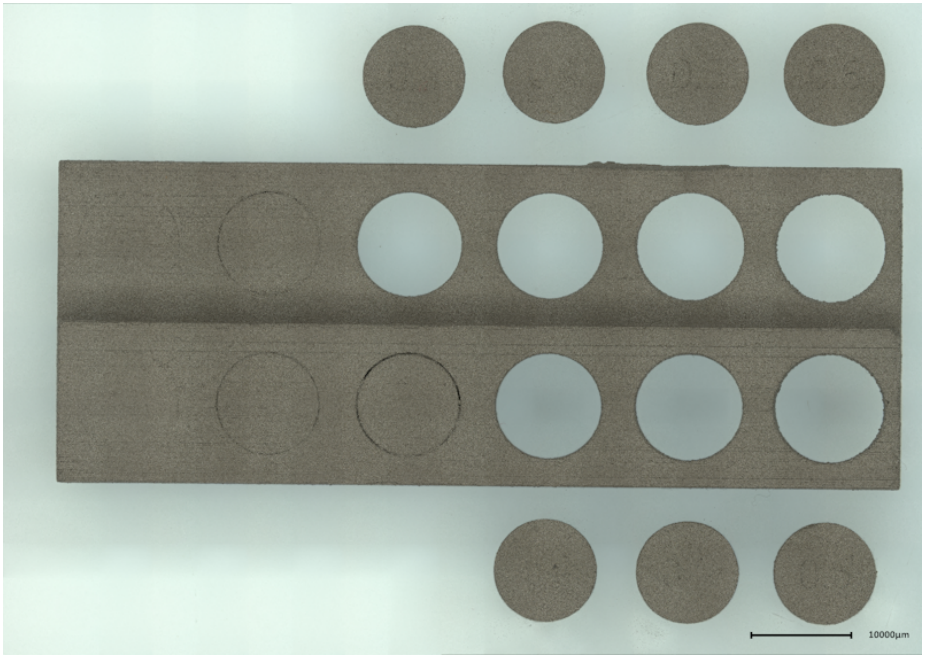


Figure 5.26: Clearance cylinder printed specimen

Figure 5.27 maps out the successful features, where success is defined as the cylinder being able to be removed from the outer wall after depowdering. A clearance of 0.4 mm is identified as the minimum clearance for being able to separate parts after printing, which is greater than the value reported by Blunk and Seibel for similar geometry [6]. One reason for this discrepency may be the effect of part thickness, the height of the cylinder in this

case, which has an effect on which clearances are successful. Intuitively, this makes sense as the difficulty of powder removal from a gap increases with depth, which determines if the cylinder can be removed. Given that the part thickness used by Blunk and Seibel is not reported, this could be a possible explanation. Referring back to the earlier results on thin gap features in Figure 5.2, it was seen that partial success was only possible down to a 0.7 mm gap. This difference is because for the clearance cylinders to move, full depowdering of the space between the cylinder and the wall is not required. There only needs to be sufficient powder removed to reduce the friction between the cylinder and the wall.

Considering now the effect of overprint, as observed in the thin wall and thin gap features, the external hole should be smaller and the internal cylinder should be larger, reducing the effective clearance between the two. Applying the values found for thin wall and thin gap as a reasonable estimate of overprint for this feature, the diameter of the cylinder would be approximately 0.3 mm oversized and the hole diameter would be approximately 0.3 mm undersized. The clearance is defined as the designed distance between the cylinder and the hole, so when referencing the CAD model, the difference in diameter between the cylinder and the hole is double the chosen clearance value. So a minimum clearance of at least 0.3 mm is expected. The actual value was noted as being 0.7 mm, which is consistent with the need for slightly more clearance than just accounting for overprint when working with powder-based AM technologies as observed by Allison et al. [65].

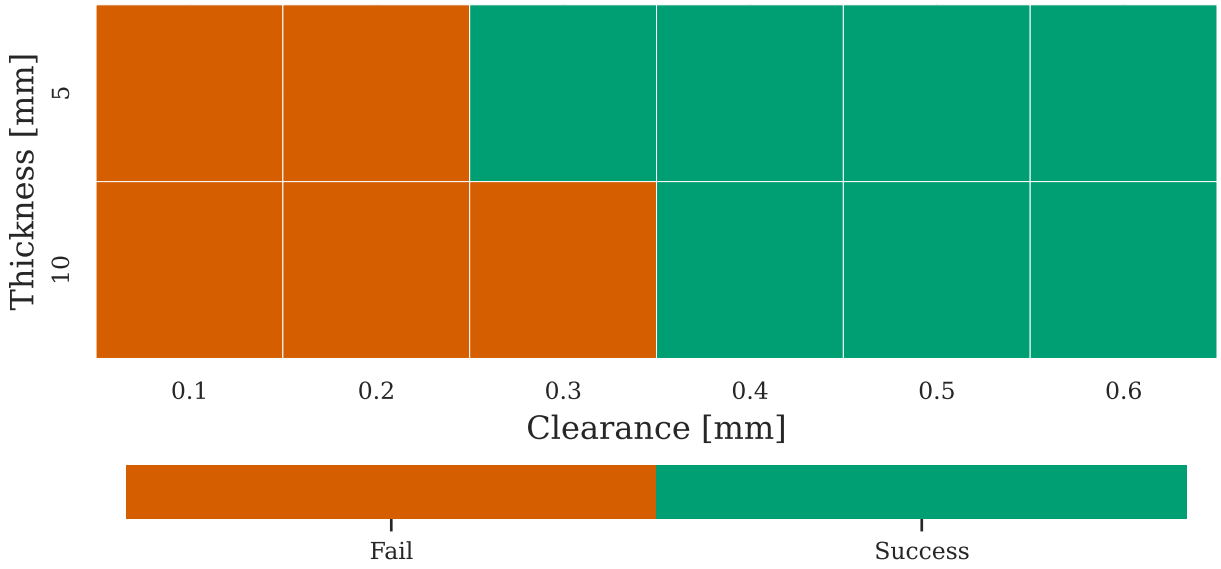


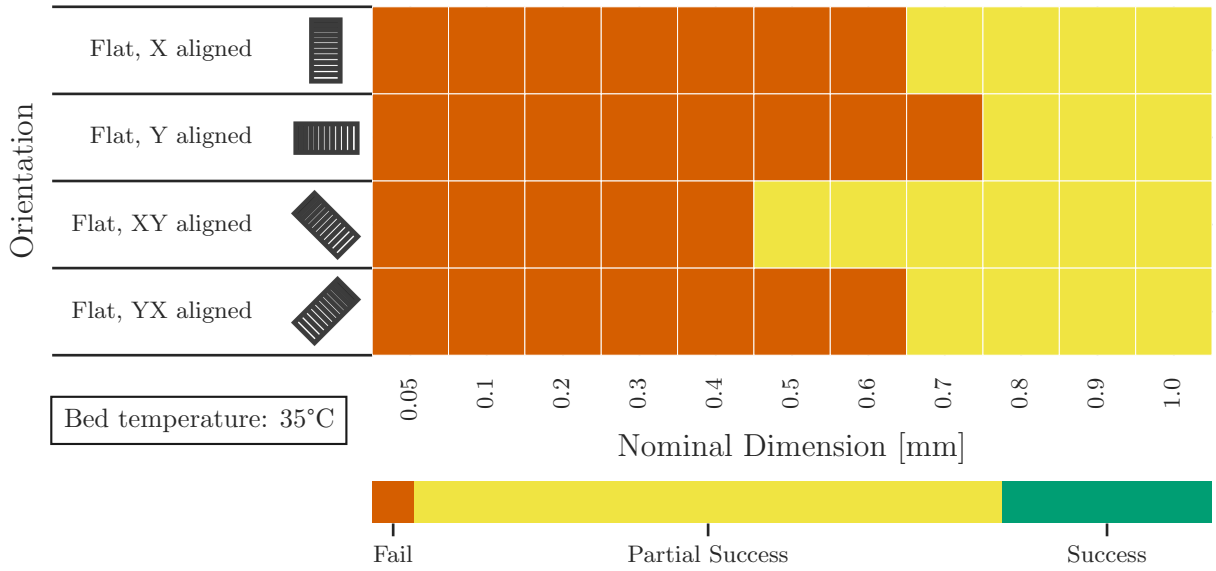
Figure 5.27: Heatmap depicting the success of removing a cylinder feature from a hole with a given clearance between the concentric surfaces and a given cylinder height (part thickness).

5.6 Effect of process parameters

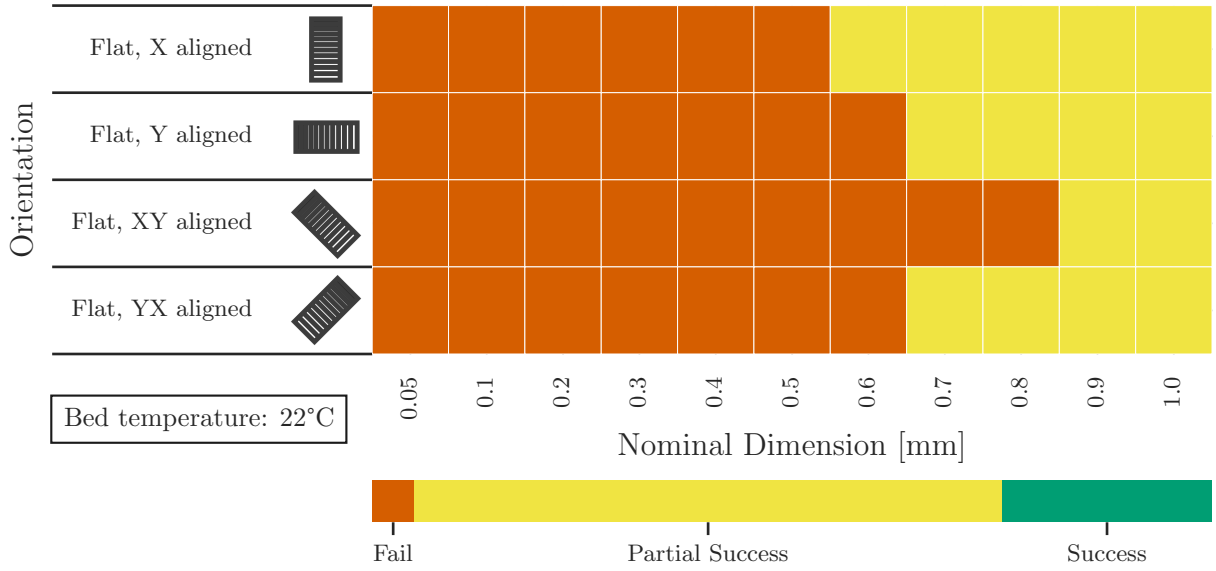
Looking first at the effect of bed temperature on the thin gap width feature, Figure 5.28a can be compared to Figure 5.28b. The results are similar, with some orientations performing better with higher bed temperatures and some orientations performing worse. It is important to note that insufficient bed heating will lead to a loss of accuracy, as binder that is not adequately heated on each layer will continue to permeate and eventually cause significant geometric deviation and overall print quality issues such as increased overprint, poor surface roughness, and/or blobs of powder on the bottom and sides of the part, [97]–[99]. Indeed, that is what is observed in Figure 5.29, where the lower temperature prints have a higher dimensional error. An example of a part that suffered a complete failure due

to inadequate heating and binder evaporation is shown in Figure 5.30. It is also noted in the literature that excessive heating can cure the binder too quickly and prevent it from permeating sufficiently to form a single cohesive part [93], so simply increasing the heating powder to the maximum possible power is not likely to lead to good part quality. Comparing the results from the main collection of specimens with those printed using the hopper configuration and lower bed temperature, the thin wall specimen was also printed on the feed bed configuration in all orientations. These results can be seen in Figure 5.31. There appears to be slight variation in the successful printing of 0.1 mm thin walls, but overall the two sets of outcomes are similar. Looking at the dimensional error of these thin wall features, the printing configuration and bed temperature does not seem to have a significant effect on that either, as seen in Figure 5.32. It is quite possible to suggest that the effects of printing configuration and bed temperature do not have a chance to show a predominant effect for parts with the same (short) thickness and with an orientation where the part thickness is always in the same Z-direction. Further work should be done to investigate these effects in detail.

Looking now at the through hole feature specimens printed using the feed bed vs. the hopper system, with performance captured in Figure 5.33a and Figure 5.33b, the results indicate that small holes less than 1.2 mm printed using the feed bed are more likely to fail than those printed with the hopper. The dimensional accuracy of these features is also significantly lower when printed using the feed bed as seen in Figure 5.34. This suggests that the machine configuration setup for supplying powder may have an effect on through holes, which is a negative feature, in contrast with thin walls which is a positive feature. This may be caused by the difference in powder bed density and how that interplays with the binder saturation and bed heating between the two configurations; these findings open up new research opportunities to study the root cause of this phenomenon.



(a) Success rate for thin gap features printed with main bed temperature



(b) Success rate for thin gap features printed with alternate bed temperature

Figure 5.28: Degree of success for printing thin gap features as categorized by Coincident%, split by bed temperature used during printing (a) specimens printed as part of main collection, with bed temperature set to 35 °C (b) specimens printed at an alternate bed temperature of 22 °C

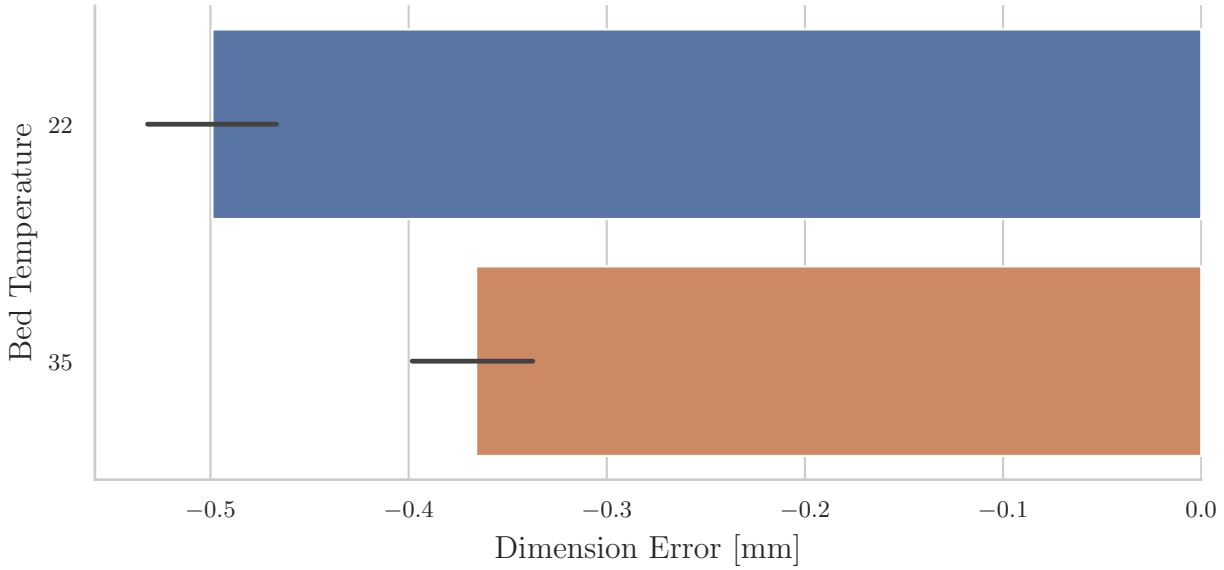


Figure 5.29: The effect of bed temperature on dimensional error of thin wall features, averaging across all nominal dimensions and orientations. Error bars represent 95% confidence interval.

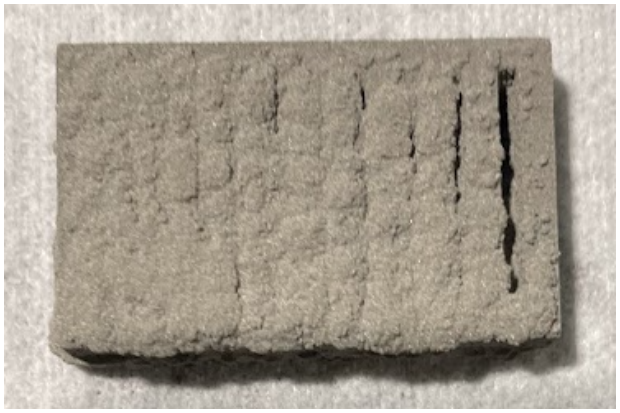
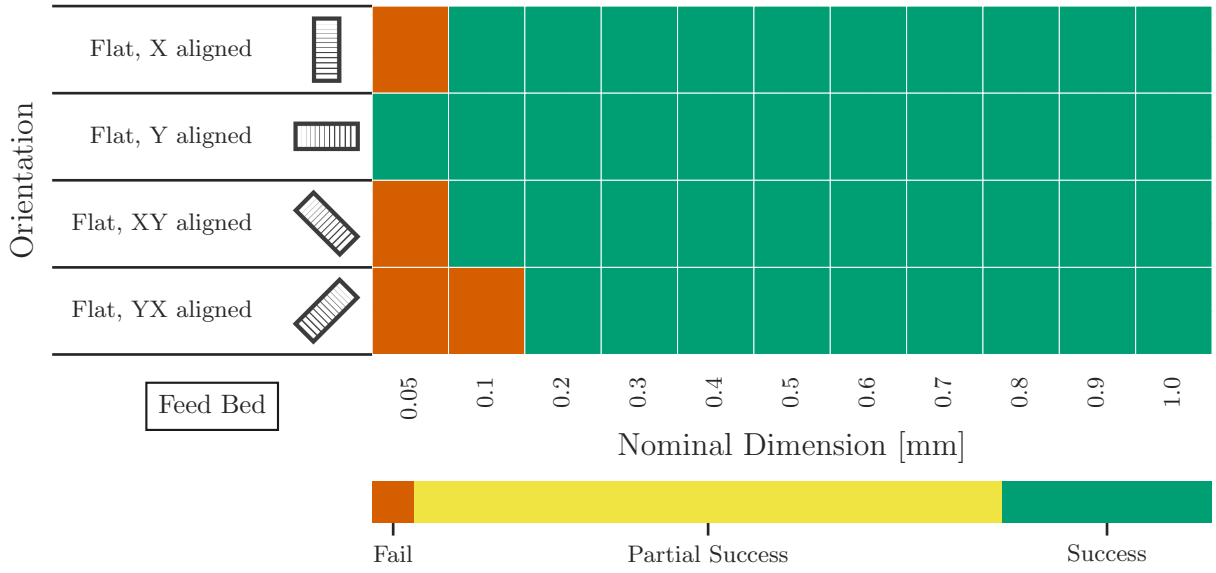
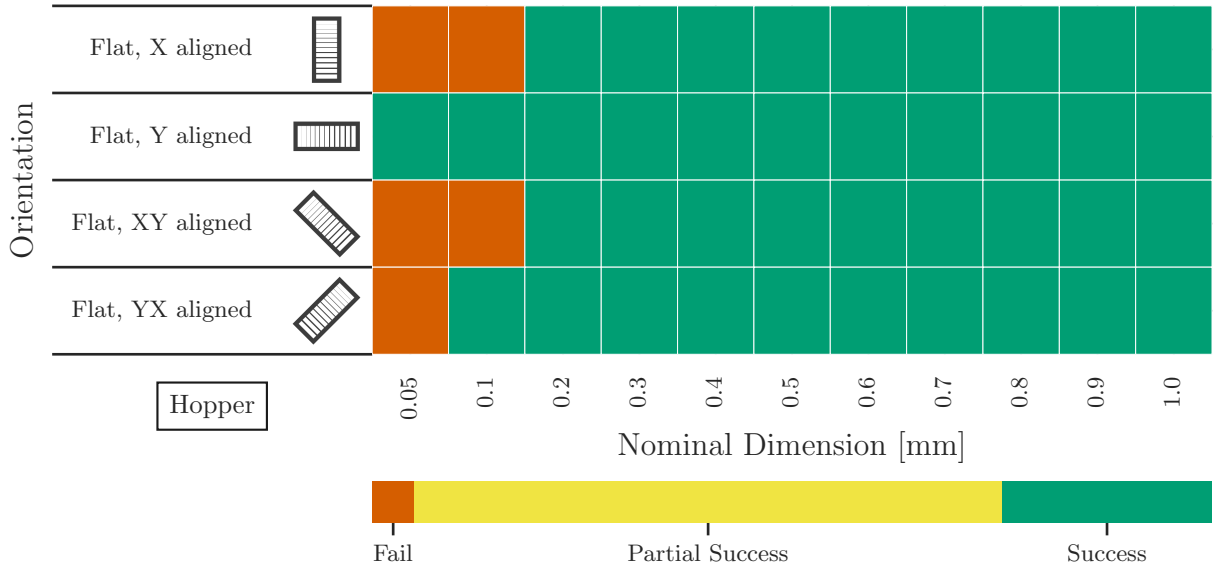


Figure 5.30: Oversaturation of thin gap specimen due to inadequate heating and binder evaporation, causing lumpy surfaces and poor geometric fidelity.



(a)



(b)

Figure 5.31: Degree of success for thin wall features based on the Coincident%, printed with powder supplied by (a) feed bed or; (b) hopper.

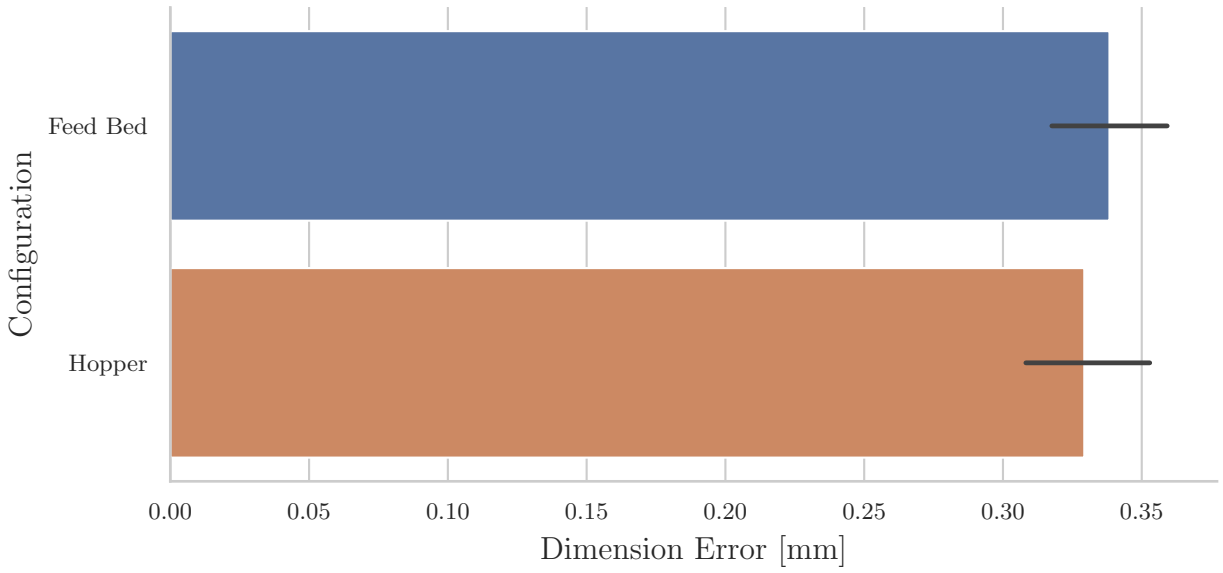
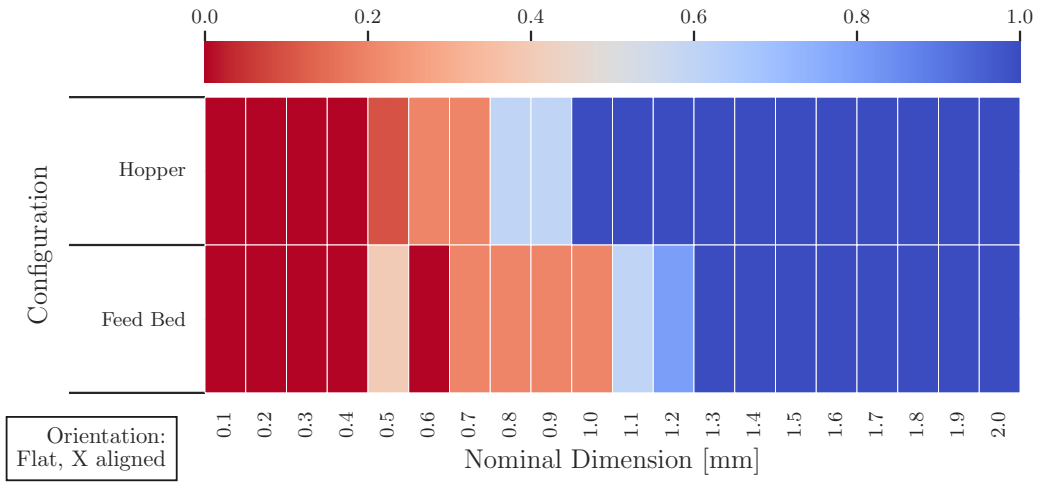
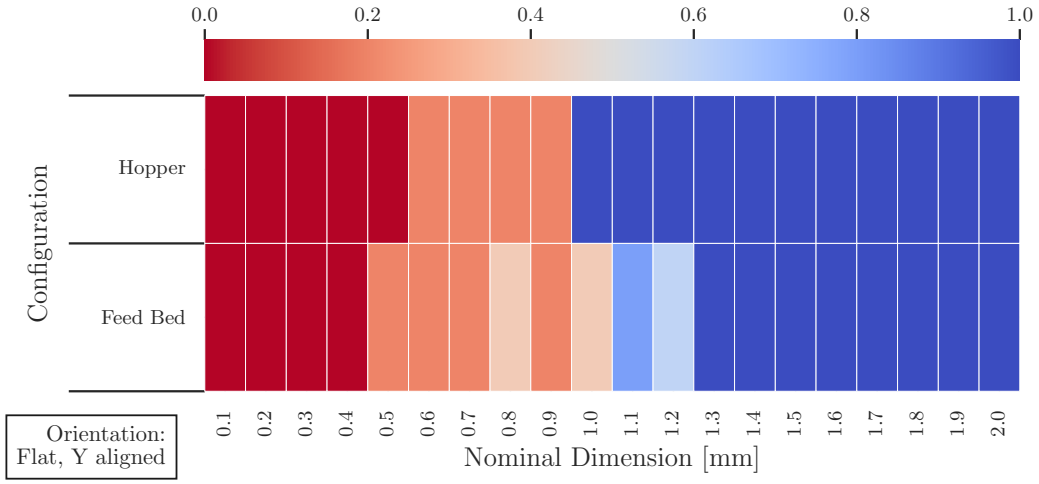


Figure 5.32: Effect of powder supply configuration on dimensional error of thin wall features, averaging across all nominal dimensions and orientations. Error bars represent 95% confidence interval.



(a)



(b)

Figure 5.33: Heatmap depicting the success ratio for through hole features averaged across different part thicknesses. The colour represents the ratio of number of features successfully printed, averaged across all part thicknesses, with the ratio ranging from 0 to 1 as indicated by the colour bar. This is for orientations of (a) Flat, X aligned and; (b) Flat, Y aligned

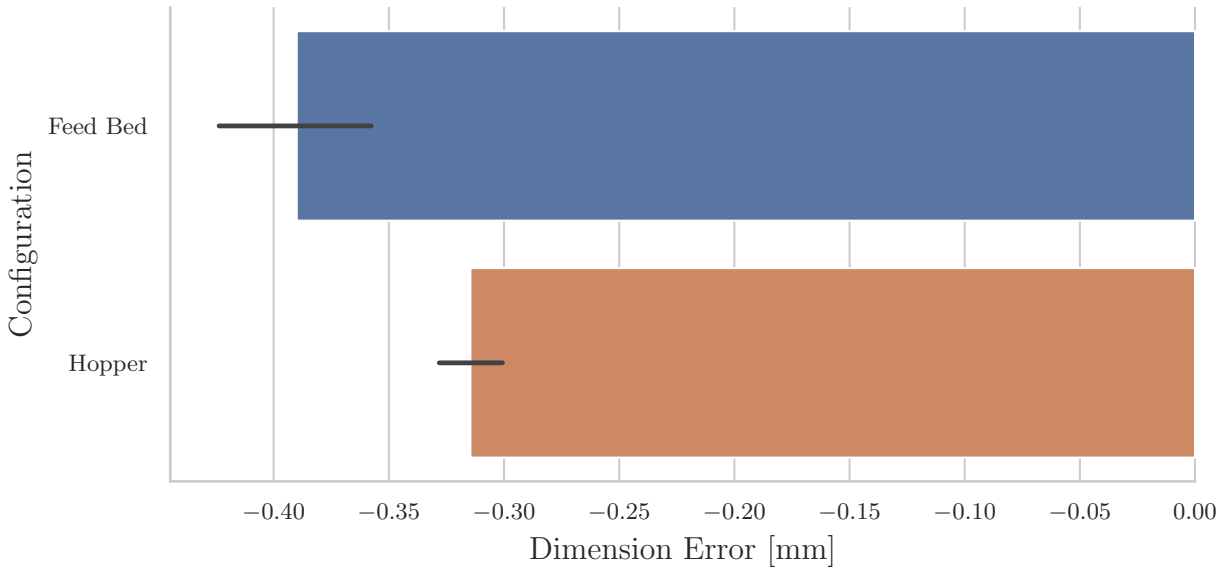


Figure 5.34: Effect of printer configuration on dimensional error for through hole features, averaging across all nominal dimensions, part thicknesses, and orientations. Error bars represent 95% confidence interval.

5.7 Proposed design rules

All of the trends and observations made in this chapter are useful for stating formal design rules that can be applied in practice when designing parts for BJAM. In the spirit of moving from design fundamentals to design rules, as described by Manesh et al. [1], the observations made earlier in this chapter will be codified as explicit relationships between feature type, feature dimension, part thickness, feature orientation, print success, dimensional error, clearance, and/or printing parameters. Based on the linear regressions performed on dimensional error, these design rules can be used to counteract the error by undersizing features at the design stage in order to achieve greater part accuracy [68]. All these design rules are limited to stainless steel 316L with spherical morphology and powder size distribution of 15-45 µm, printed on an ExOne M-Flex BJAM printer, using the specific process parameters described in Table 4.2. What is important is to propose design artefacts and methodologies to develop these regressions to help standardize reporting on dimensional fidelity and tune compensation to improve dimensional accuracy across materials and BJAM technology classes. This work was a demonstration of such a workflow. The descriptions below provide an overview of the design rules, and Figure 5.35 and Figure 5.36 shows a more detailed list of design rules in graphical format.

5.7.1 Thin walls

For the experimental conditions described in this study, thin walls should be designed with a minimum 0.3 mm thickness if printing in any orientation where the walls are perpendicular to the build bed. Thin walls with a minimum thickness of 0.05 mm may be used if oriented so that the walls are parallel to the direction of printhead jetting, such as the specimens printed in the "Flat, Y aligned" orientation.

The thickness of thin walls should be decreased by 0.33 mm to improve the dimensional fidelity in printing. This design rule combined with the design rule describing the minimum width of thin walls as described in the previous paragraph means that the minimum wall size that can be consistently printed in practice will measure roughly 0.6 mm in thickness across different orientations.

5.7.2 Thin gaps and vertical gaps

Long thin gaps with a depth of 5 mm should be designed with a minimum 0.7 mm width if printing in any orientation. If printing so that the gap is purely along the Z-axis, a minimum width of 0.4 mm may be used. If the gap is purely along the Z-axis and the depth of the gap is 1 mm, then a minimum width of 0.2 mm may be used.

The width of gaps along the X or Y axes should be increased by 0.37 mm to improve the dimensional fidelity in printing. If the gap is along the Z axis, then Equation 5.3 should be applied to calculate the appropriate compensation. This design rule combined with the design rule describing the minimum width of thin gaps as described in the previous paragraph means that the minimum gap width that can be printed along the X or Y axes will measure roughly 0.3 mm in width.

5.7.3 Through holes

Circular through holes with a depth of 1 mm should be designed with a minimum 0.5 mm diameter if printing in any orientation. If printing through holes with a depth of 5 mm, a minimum diameter of 0.8 mm should be used. More specific tables for intermediate part thicknesses can be found in Figures 5.5 - 5.9.

The diameter of through holes along the Z axis should be increased by 0.39 mm to increase the dimensional fidelity in printing. If the gap is along the X axis, then it should be increased by 0.35 mm and if along the Y axis, 0.25 mm. More precise compensation values can be calculated using Equation 5.4 and should be applied to calculate the appropriate compensation. This design rule combined with the previous one means that the minimum hole diameter that can be printed in any orientation with a depth of 5 mm will measure roughly 0.6 mm in width.

5.7.4 Clearance

Parts that are intended to be separated after printing should be separated by at least a minimum clearance of 0.4 mm in the X and Y axes. This clearance is dependent on the depth of the parts and Figure 5.27 can referenced for more details.

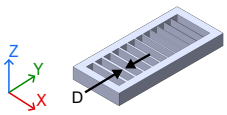
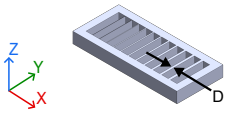
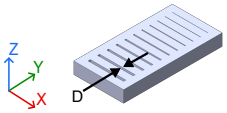
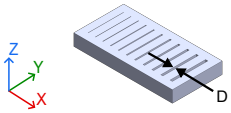
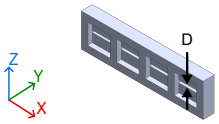
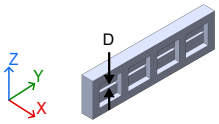
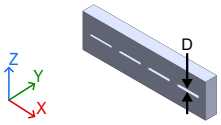
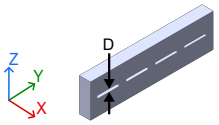
	1.1 For a thin wall that is X aligned and 5 mm high, dimension D must satisfy the constraint: D ≥ 0.3 mm
	1.2 For a thin wall that is Y aligned and 5 mm high, dimension D must satisfy the constraint: D ≥ 0.05 mm
	2.1 For a thin gap feature that is X aligned and 5 mm deep, dimension D must satisfy the constraint: D ≥ 0.7 mm
	2.2 For a thin gap feature that is Y aligned and 5 mm deep, dimension D must satisfy the constraint: D ≥ 0.8 mm
	3.1 For a vertical gap that is X aligned and 1 mm thick, dimension D must satisfy the constraint: D ≥ 0.2 mm
	3.2 For a vertical gap that is Y aligned and 1 mm thick, dimension D must satisfy the constraint: D ≥ 0.1 mm
	3.3 For a vertical gap that is X aligned and 5 mm thick, dimension D must satisfy the constraint: D ≥ 0.3 mm
	3.4 For a vertical gap that is Y aligned and 5 mm thick, dimension D must satisfy the constraint: D ≥ 0.3 mm

Figure 5.35: Proposed design rule table for thin walls, thin gaps, and vertical gaps, with graphical representations of each feature type and their orientation.

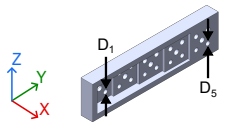
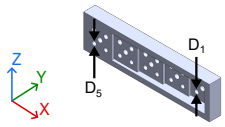
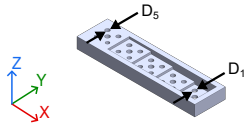
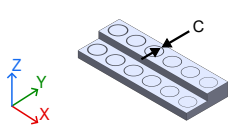
	For a through hole feature that is along the X axis, diameter D must satisfy the constraint: 4.1 if part thickness is 1 mm: $D_1 \geq 0.5$ mm 4.2 if part thickness is 5 mm: $D_5 \geq 0.8$ mm
	For a through hole feature that is along the Y axis, diameter D must satisfy the constraint: 4.3 if part thickness is 1 mm: $D_1 \geq 0.3$ mm 4.4 if part thickness is 5 mm: $D_5 \geq 0.8$ mm
	For a through hole feature that is along the Z axis, diameter D must satisfy the constraint: 4.5 if part thickness is 1 mm: $D_1 \geq 0.6$ mm 4.6 if part thickness is 5 mm: $D_5 \geq 1.0$ mm
	For a cylindrical feature to be separated, clearance C must satisfy the constraint: 5.1 if the height of cylinder is 5 mm: $C \geq 0.4$ mm 5.2 if the height of cylinder is 10 mm: $C \geq 0.5$ mm

Figure 5.36: Proposed design rule table for through holes and clearances, with graphical representations of each feature type and their orientation.

Chapter 6

Conclusion

This work presented a workflow for developing design rules for an AM process based on design artifacts that are printed in multiple conditions, that are then analysed using a standardized computer vision workflow. This workflow is a fast and consistent method for collecting the data required to quantify dimensional defects and could be expanded to a variety of geometries and processes, provided that the the design artifacts test limiting design features that are relevant for the AM technology class under invesitgation. The workflow presented here describes a set of artifacts designed particularly to test BJAM. This workflow was then demonstrated to develop a set of design rules for binder jetting additive manufacturing under a specific set of process parameters to determine the behaviour of thin walls, gaps, and through holes. Clearances were investigated using a separate approach to augment the coverage of the design rules.

In the process of developing the design rules, several observations were made about the printability of certain classes of features and their dimensional error. Relationships between dimensional error and nominal dimension, feature orientation, and/or feature

thickness were found using linear regression for these features. Additional experiments hinted at the possible effects of powder dispensing configurations (hopper versus feed bed), bed temperature, and binder saturation on feature printability success and dimensional fidelity error; opportunities for further work were identified to understand those effects.

These design rules can now be applied to a variety of designs within this material and process parameter specification, allowing designers to adapt and compensate their geometries for BJAM to ensure successful printing and good dimensional fidelity by applying offsets to features. Furthermore, the workflow can be applied if the material and/or printing conditions are changed to devise the design rules under such conditions.

6.1 Limitations of this work

This work is subject to a number of limitations, both inherent to the scope that was chosen and experimental limitations. The printing of specimens was affected by a number of manufacturing challenges, including a malfunctioning roller motor, mechanical jamming of the build bed, inconsistent powder dispensing from the hopper, incorrectly aligned bed temperature sensors, and variations in printhead droplet volume. Another challenge of this work was that the printing parameters were not optimized prior to starting the experimental runs, meaning that the proposed design rules are subject to change if an improved set of parameters are found. Samples that did not have identical machine printing conditions (outside of the parameters of interest) were not included in this study. Depowdering is also subject to operator influence, a different set of outcomes may have been measured if the skill and experience of the operator was different. The value of this work is in the workflow that is described and in the development of design rules within defined boundaries.

6.2 Future work

Many areas exist to expand or adapt the work that was carried out in this thesis. One application is to use the workflow to collect further experimental data to build a full process map for binder jetting additive manufacturing across material classes, for process parameters that have been optimized to yield the best green part density outcome. Furthermore, using the current set of features but expanding to angled orientations, other thicknesses, and changing the length of features would provide useful information to further specify the design rules proposed in this work. Other work needed for a full process mapping would include expanding to other geometric features such as edges, fillets, and blind holes. Printing repeated copies of specimens would also validate the repeatability of the observations and could also be used to track whether the performance of the machine changes over time and usage. The work flow and resulting process performance maps could also be used in process parameter optimization and refinement to target dimensional fidelity and green part density in tandem; in particular, the layer thickness, bed temperature, binder saturation, and printing configuration are of importance. Expanding this knowledge to other material classes and powder size distributions would also prove useful for users seeking to design parts for biomedical and electromagnetic applications of BJAM.

This workflow is also suitable to be used in conjunction with testing of mechanical properties such as tensile strength or density to perform a holistic process parameter optimization, from green part density, to geometric fidelity, to mechanical properties, for both existing and novel materials. The workflow could also be used in benchmarking performance drift across machines or over time on the same machine.

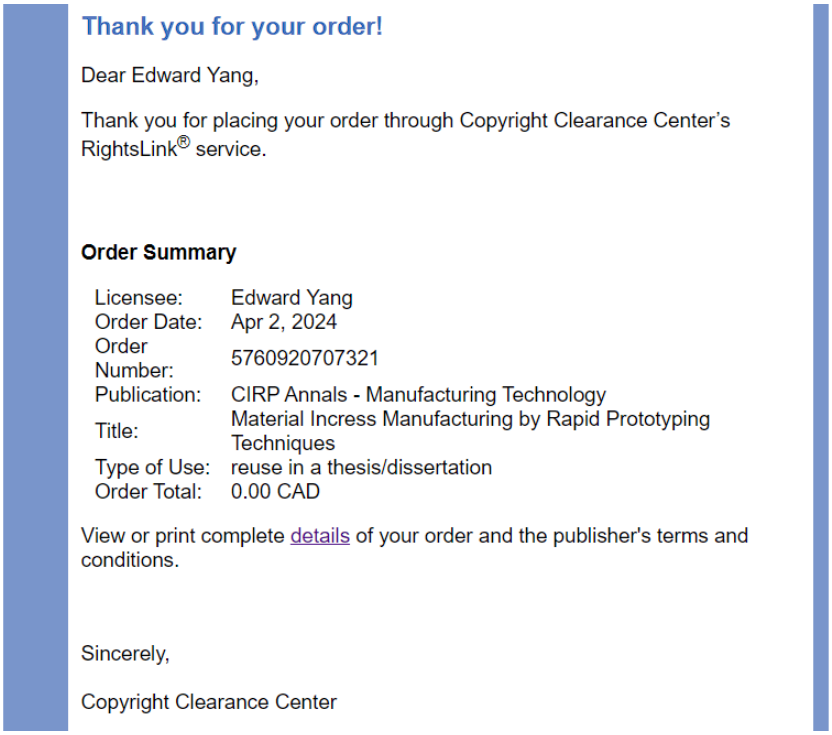
Another way this work can be expanded is by looking at the computer vision algorithm within the workflow. At the moment, it is a useful but limited tool that could be improved

in many ways. This could include increasing the robustness of the contour registration, automating the selection of certain function parameters, and even expanding its utility by integrating it into in-situ monitoring of the printing process to extract layer-by-layer geometric fidelity data. Application of machine learning techniques to analyse the images also holds promise and could also provide a useful source of data for training models to predict printability and geometric compensation factors [100].

Looking more broadly at the topic of geometric fidelity of BJAM, the workflow presented here could also be applied to understanding the effects of post-processing on green parts. The specimens printed as part of this thesis can be sintered to expand design rules to include sintering and develop a new model for compensation factors to offset deformation occuring during sintering. Currently, work exists on predicting the shrinkage behaviour of parts after undergo sintering, however optical dilatometry presents a source of in-situ image data that could be used to further understand the geometric behaviour of parts as they are sintered [80].

Letters of Copyright Permission

Figure 2.4 is reproduced under license from Elsevier, see Figure 6.1 for a copy of the letter confirming the license order [48].



Thank you for your order!

Dear Edward Yang,

Thank you for placing your order through Copyright Clearance Center's RightsLink® service.

Order Summary

Licensee:	Edward Yang
Order Date:	Apr 2, 2024
Order Number:	5760920707321
Publication:	CIRP Annals - Manufacturing Technology
Title:	Material Incress Manufacturing by Rapid Prototyping Techniques
Type of Use:	reuse in a thesis/dissertation
Order Total:	0.00 CAD

View or print complete details of your order and the publisher's terms and conditions.

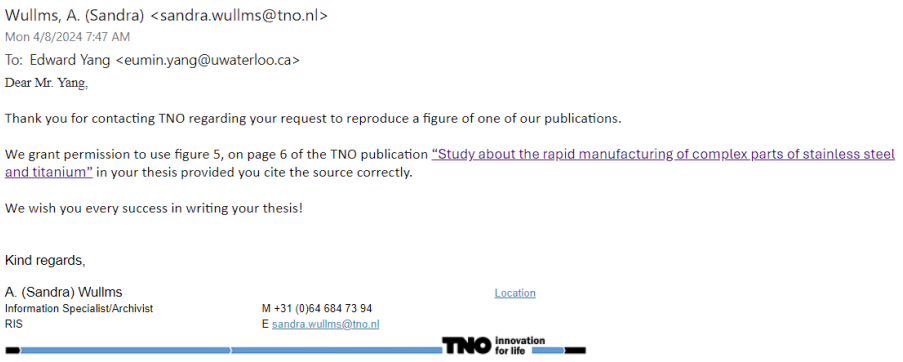
Sincerely,

Copyright Clearance Center

Figure 6.1: Letter confirming the license to reproduce Figure 2.4

Figure 2.5 is reproduced from a report published by the National Institute of Standards and Technology (NIST) which is in the public domain [54].

Figure 2.6 is reproduced with permission from TNO, Netherlands, see Figure 6.2 for a copy of the letter granting permission [55].



Wullms, A. (Sandra) <sandra.wullms@tno.nl>
Mon 4/8/2024 7:47 AM
To: Edward Yang <eumin.yang@uwaterloo.ca>
Dear Mr. Yang,

Thank you for contacting TNO regarding your request to reproduce a figure of one of our publications.

We grant permission to use figure 5, on page 6 of the TNO publication "Study about the rapid manufacturing of complex parts of stainless steel and titanium" in your thesis provided you cite the source correctly.

We wish you every success in writing your thesis!

Kind regards,

A. (Sandra) Wullms
Information Specialist/Archivist
RIS
M +31 (0)64 684 73 94
E sandra.wullms@tno.nl
Location
TNO innovation for life

Figure 6.2: Letter granting appropriate permission to reproduce Figure 2.6

References

[1] M. Mani, P. Witherell, and H. Jee, "Design rules for additive manufacturing: A categorization," in *Volume 1: 37th Computers and Information in Engineering Conference*, Cleveland, Ohio, USA: American Society of Mechanical Engineers, Aug. 6, 2017, V001T02A035, ISBN: 978-0-7918-5811-0. DOI: 10.1115/DETC2017-68446. [Online]. Available: https://asmedigitalcollection.asme.org/IDETC-CIE/proceedings/IDETC-CIE2017/58110/Cleveland,%20Ohio,%20USA/259177 (visited on 12/09/2022).

[2] M. Yang, M. K. Keshavarz, M. Vlasea, and A. Molavi-Kakhki, "Towards full-dense high geometric fidelity parts via binder jetting and controlled sintering," *Journal of Manufacturing Processes*, vol. 115, pp. 180–191, Apr. 15, 2024, ISSN: 1526-6125. DOI: 10.1016/j.jmapro.2024.02.028. [Online]. Available: https://www.sciencedirect.com/science/article/pii/S1526612524001580 (visited on 03/03/2024).

[3] G. K. Meenashisundaram, Z. Xu, M. L. S. Nai, S. Lu, J. S. Ten, and J. Wei, "Binder jetting additive manufacturing of high porosity 316l stainless steel metal foams," *Materials (Basel, Switzerland)*, vol. 13, no. 17, p. 3744, Aug. 24, 2020, ISSN: 1996-1944. DOI: 10.3390/ma13173744.

[4] A. Elliott and C. Waters, *Additive Manufacturing for Designers: A Primer*. SAE International, Feb. 15, 2019, 92 pp., Google-Books-ID: GuObEAAAQBAJ, ISBN: 978-0-7680-9412-1.

[5] C. C. Seepersad, T. Govett, K. Kim, M. Lundin, and D. Pinero, "A designer's guide for dimensioning and tolerancing SLS parts," p. 11,

[6] H. Blunk and A. Seibel, "Design guidelines for metal binder jetting," *Progress in Additive Manufacturing*, Jun. 30, 2023, ISSN: 2363-9520. DOI: 10.1007/s40964-023-00475-y. [Online]. Available: https://doi.org/10.1007/s40964-023-00475-y (visited on 10/12/2023).

[7] Matthias Schmidt-Lehr and Timo Fuhrer, *Design guideline for sinter-based additive manufacturing*, Mar. 2021.

[8] ExOne, *2020 metal 3d printing manufacturing design guidelines*, 2020.

[9] Xometry, *Design guide binder jet metal 3d printing*.

[10] A. Mostafaei, A. M. Elliott, J. E. Barnes, *et al.*, "Binder jet 3d printing—process parameters, materials, properties, modeling, and challenges," *Progress in Materials Science*, vol. 119, p. 100 707, Jun. 1, 2021, ISSN: 0079-6425. DOI: 10.1016/j.pmatsci.2020.100707. [Online]. Available: https://www.sciencedirect.com/science/article/pii/S0079642520300712 (visited on 07/25/2022).

[11] M. Li, W. Du, A. Elwany, Z. Pei, and C. Ma, "Metal binder jetting additive manufacturing: A literature review," *Journal of Manufacturing Science and Engineering*, vol. 142, no. 9, Jun. 25, 2020, ISSN: 1087-1357. DOI: 10.1115/1.4047430. [Online]. Available: https://doi.org/10.1115/1.4047430 (visited on 06/13/2022).

[12] A. M. Elliott, A. M. Momen, M. Benedict, and J. Kiggans, "Experimental study of the maximum resolution and packing density achievable in sintered and non-sintered binder-jet 3d printed steel microchannels," presented at the ASME 2015 International Mechanical Engineering Congress and Exposition, American Society of Mechanical Engineers Digital Collection, Mar. 7, 2016. DOI: 10.1115/IMECE2015-53428. [Online]. Available: http://asmedigitalcollection-asme-org/IMECE/proceedings/IMECE2015/57359/V02AT02A019/260439 (visited on 10/07/2022).

[13] W. Du, W. Yu, D. M. France, and D. Singh, "Depowdering of an additively manufactured heat exchanger with narrow and turning channels," *Additive Manufacturing Letters*, vol. 9, p. 100 202, Apr. 1, 2024, ISSN: 2772-3690. DOI: 10.1016/j.addlet.2024.100202. [Online]. Available: https://www.sciencedirect.com/science/article/pii/S2772369024000112 (visited on 03/17/2024).

[14] M. Yang, M. K. Keshavarz, M. Vlasea, A. Molavi-Kakhki, and M. Laher, "Super-solidus liquid phase sintering of water-atomized low-alloy steel in binder jetting additive manufacturing," *Heliyon*, vol. 9, no. 3, Mar. 1, 2023, Publisher: Elsevier, ISSN: 2405-8440. DOI: 10.1016/j.heliyon.2023.e13882. [Online]. Available: https://www.cell.com/heliyon/abstract/S2405-8440(23)01089-7 (visited on 03/05/2024).

[15] S. Mirzababaei and S. Pasebani, "A review on binder jet additive manufacturing of 316l stainless steel," *Journal of Manufacturing and Materials Processing*, vol. 3, no. 3, p. 82, Sep. 9, 2019, ISSN: 2504-4494. DOI: 10.3390/jmmp3030082. [Online]. Available: https://www.mdpi.com/2504-4494/3/3/82 (visited on 10/05/2022).

[16] B. J. Paudel, H. Deng, and A. C. To, "A physics-based data-driven distortion compensation model for sintered binder jet parts considering size effects," *Additive Man-*

ufacturing, vol. 68, p. 103 517, Apr. 25, 2023, ISSN: 2214-8604. DOI: 10.1016/j.addma.2023.103517. [Online]. Available: https://www.sciencedirect.com/science/article/pii/S2214860423001306 (visited on 03/11/2024).

[17] B. J. Paudel, D. Conover, J.-K. Lee, and A. C. To, "A computational framework for modeling distortion during sintering of binder jet printed parts," *Journal of Micromechanics and Molecular Physics*, vol. 06, no. 4, pp. 95–102, Dec. 2021, Publisher: World Scientific Publishing Co., ISSN: 2424-9130. DOI: 10.1142/S242491302142008X. [Online]. Available: https://worldscientific.com/doi/abs/10.1142/S242491302142008X (visited on 03/11/2024).

[18] S. Sadeghi Borujeni, A. Shad, K. Abburi Venkata, N. Günther, and V. Ploshikhin, "Numerical simulation of shrinkage and deformation during sintering in metal binder jetting with experimental validation," *Materials & Design*, vol. 216, p. 110 490, Apr. 1, 2022, ISSN: 0264-1275. DOI: 10.1016/j.matdes.2022.110490. [Online]. Available: https://www.sciencedirect.com/science/article/pii/S0264127522001113 (visited on 04/11/2023).

[19] K. Zhang, W. Zhang, R. Brune, *et al.*, "Numerical simulation and experimental measurement of pressureless sintering of stainless steel part printed by binder jetting additive manufacturing," *Additive Manufacturing*, vol. 47, p. 102 330, Nov. 1, 2021, ISSN: 2214-8604. DOI: 10.1016/j.addma.2021.102330. [Online]. Available: https://www.sciencedirect.com/science/article/pii/S2214860421004887 (visited on 02/20/2023).

[20] T. Do, P. Kwon, and C. S. Shin, "Process development toward full-density stainless steel parts with binder jetting printing," *International Journal of Machine Tools and Manufacture*, Special Issue on the State-of-the-Art in North American Manufactur-

ing Research, vol. 121, pp. 50–60, Oct. 1, 2017, ISSN: 0890-6955. DOI: 10.1016/j.ijmachtools.2017.04.006. [Online]. Available: https://www.sciencedirect.com/science/article/pii/S0890695516304758 (visited on 10/05/2022).

[21] E. Sachs, M. Cima, and J. Cornie, "Three-dimensional printing: Rapid tooling and prototypes directly from a CAD model," *CIRP Annals*, vol. 39, no. 1, pp. 201–204, Jan. 1, 1990, ISSN: 0007-8506. DOI: 10.1016/S0007-8506(07)61035-X. [Online]. Available: https://www.sciencedirect.com/science/article/pii/S00078506 0761035X (visited on 03/09/2024).

[22] H. Miyanaji, N. Momenzadeh, and L. Yang, "Effect of powder characteristics on parts fabricated via binder jetting process," *Rapid Prototyping Journal*, vol. 25, no. 2, pp. 332–342, 2019, Num Pages: 11 Place: Bradford, United Kingdom Publisher: Emerald Group Publishing Limited, ISSN: 13552546. DOI: 10.1108/RPJ-03-2018-0069. [Online]. Available: https://www.proquest.com/docview/2185492891/abstract/10F7C121DE304111PQ/1 (visited on 03/11/2024).

[23] A. Lores, N. Azurmendi, I. Agote, and E. Zuza, "A review on recent developments in binder jetting metal additive manufacturing: Materials and process characteristics," *Powder Metallurgy*, vol. 62, no. 5, pp. 267–296, Oct. 20, 2019, Publisher: Taylor & Francis _eprint: https://doi.org/10.1080/00325899.2019.1669299, ISSN: 0032-5899. DOI: 10.1080/00325899.2019.1669299. [Online]. Available: https://doi.org/10.1080/00325899.2019.1669299 (visited on 10/05/2022).

[24] S. Stopp, T. Wolff, F. Irlinger, and T. Lueth, "A new method for printer calibration and contour accuracy manufacturing with 3d-print technology," *Rapid Prototyping Journal*, vol. 14, no. 3, pp. 167–172, Jan. 1, 2008, Publisher: Emerald Group Publish-

ing Limited, ISSN: 1355-2546. DOI: 10.1108/13552540810878030. [Online]. Available: https://doi.org/10.1108/13552540810878030 (visited on 03/09/2024).

[25] I. Gibson, D. Rosen, B. Stucker, and M. Khorasani, "Binder jetting," *Additive Manufacturing Technologies*, pp. 237–252, 2021, Publisher: Springer, Cham. DOI: 10.1007/978-3-030-56127-7_8. [Online]. Available: http://link-springer-com/chapter/10.1007/978-3-030-56127-7_8 (visited on 10/05/2022).

[26] B. Verlee, T. Dormal, and J. Lecomte-Beckers, "Density and porosity control of sintered 316l stainless steel parts produced by additive manufacturing," *Powder Metallurgy*, vol. 55, no. 4, pp. 260–267, 2012, ISSN: 1743-2901. DOI: 10.1179/003258912Z.00000000082.

[27] T. Do, C. S. Shin, D. Stetsko, *et al.*, "Improving structural integrity with boron-based additives for 3d printed 420 stainless steel," *Procedia Manufacturing*, 43rd North American Manufacturing Research Conference, NAMRC 43, 8-12 June 2015, UNC Charlotte, North Carolina, United States, vol. 1, pp. 263–272, Jan. 1, 2015, ISSN: 2351-9789. DOI: 10.1016/j.promfg.2015.09.019. [Online]. Available: https://www.sciencedirect.com/science/article/pii/S2351978915010197 (visited on 03/22/2024).

[28] M. Castilho, B. Gouveia, I. Pires, J. Rodrigues, and M. Pereira, "The role of shell/core saturation level on the accuracy and mechanical characteristics of porous calcium phosphate models produced by 3dprinting," *Rapid Prototyping Journal*, vol. 21, no. 1, pp. 43–55, Jan. 1, 2015, Publisher: Emerald Group Publishing Limited, ISSN: 1355-2546. DOI: 10.1108/RPJ-02-2013-0015. [Online]. Available: https://doi.org/10.1108/RPJ-02-2013-0015 (visited on 03/02/2024).

[29] C. Hartmann, J. Silberhorn, P. Erhard, and D. Günther, "On the mechanism of binder migration in furan binder jetting of sand molds and cores," *Additive Manufacturing*, vol. 83, p. 104 073, Mar. 5, 2024, ISSN: 2214-8604. DOI: 10.1016/j.addma.2024.104073. [Online]. Available: https://www.sciencedirect.com/science/article/pii/S2214860424001192 (visited on 03/12/2024).

[30] M. Turker, D. Godlinski, and F. Petzoldt, "Effect of production parameters on the properties of IN 718 superalloy by three-dimensional printing," *Materials Characterization*, vol. 59, no. 12, pp. 1728–1735, Dec. 1, 2008, ISSN: 1044-5803. DOI: 10.1016/j.matchar.2008.03.017. [Online]. Available: https://www.sciencedirect.com/science/article/pii/S1044580308001253 (visited on 03/22/2024).

[31] A. Mostafaei, E. L. Stevens, E. T. Hughes, S. D. Biery, C. Hilla, and M. Chmielus, "Powder bed binder jet printed alloy 625: Densification, microstructure and mechanical properties," *Materials & Design*, vol. 108, pp. 126–135, Oct. 15, 2016, ISSN: 0264-1275. DOI: 10.1016/j.matdes.2016.06.067. [Online]. Available: https://www.sciencedirect.com/science/article/pii/S026412751630819X (visited on 03/22/2024).

[32] F. C. Fierz, F. Beckmann, M. Huser, *et al.*, "The morphology of anisotropic 3d-printed hydroxyapatite scaffolds," *Biomaterials*, vol. 29, no. 28, pp. 3799–3806, Oct. 1, 2008, ISSN: 0142-9612. DOI: 10.1016/j.biomaterials.2008.06.012. [Online]. Available: https://www.sciencedirect.com/science/article/pii/S0142961208004171 (visited on 03/22/2024).

[33] S. Infanger, A. Haemmerli, S. Iliev, A. Baier, E. Stoyanov, and J. Quodbach, "Powder bed 3d-printing of highly loaded drug delivery devices with hydroxypropyl cellulose as solid binder," *International Journal of Pharmaceutics*, vol. 555, pp. 198–

206, Jan. 30, 2019, ISSN: 0378-5173. DOI: 10.1016/j.ijpharm.2018.11.048. [Online]. Available: https://www.sciencedirect.com/science/article/pii/S037851731830872X (visited on 10/07/2022).

[34] I. Rishmawi, M. Salarian, and M. Vlasea, "Tailoring green and sintered density of pure iron parts using binder jetting additive manufacturing," *Additive Manufacturing*, vol. 24, pp. 508–520, Dec. 1, 2018, ISSN: 2214-8604. DOI: 10.1016/j.addma.2018.10.015. [Online]. Available: https://www.sciencedirect.com/science/article/pii/S2214860418304731 (visited on 02/20/2023).

[35] E. Mendoza Jimenez, D. Ding, L. Su, *et al.*, "Parametric analysis to quantify process input influence on the printed densities of binder jetted alumina ceramics," *Additive Manufacturing*, vol. 30, p. 100 864, Dec. 1, 2019, ISSN: 2214-8604. DOI: 10.1016/j.addma.2019.100864. [Online]. Available: https://www.sciencedirect.com/science/article/pii/S2214860419307821 (visited on 02/20/2023).

[36] J. Ingaglio, J. Fox, C. J. Naito, and P. Bocchini, "Material characteristics of binder jet 3d printed hydrated CSA cement with the addition of fine aggregates," *Construction and Building Materials*, vol. 206, pp. 494–503, May 10, 2019, ISSN: 0950-0618. DOI: 10.1016/j.conbuildmat.2019.02.065. [Online]. Available: https://www.sciencedirect.com/science/article/pii/S0950061819303587 (visited on 03/22/2024).

[37] F. E. Wiria, J. Y. M. Shyan, P. N. Lim, F. G. C. Wen, J. F. Yeo, and T. Cao, "Printing of titanium implant prototype," *Materials & Design*, Advanced Component Manufacture from Light Materials, vol. 31, S101–S105, Jun. 1, 2010, ISSN: 0261-3069. DOI: 10.1016/j.matdes.2009.12.050. [Online]. Available: https:

//www.sciencedirect.com/science/article/pii/S0261306910000130 (visited on 03/22/2024).

[38] H. Miyanaji, S. Zhang, A. Lassell, A. A. Zandinejad, and L. Yang, "Optimal process parameters for 3d printing of porcelain structures," *Procedia Manufacturing*, vol. 5, pp. 870–887, 2016, ISSN: 23519789. DOI: 10.1016/j.promfg.2016.08.074. [Online]. Available: https://linkinghub.elsevier.com/retrieve/pii/S2351978916300865 (visited on 03/21/2024).

[39] A. Kumar, Y. Bai, A. Eklund, and C. B. Williams, "Effects of hot isostatic pressing on copper parts fabricated via binder jetting," *Procedia Manufacturing*, 45th SME North American Manufacturing Research Conference, NAMRC 45, LA, USA, vol. 10, pp. 935–944, Jan. 1, 2017, ISSN: 2351-9789. DOI: 10.1016/j.promfg.2017.07.084. [Online]. Available: https://www.sciencedirect.com/science/article/pii/S2351978917302664 (visited on 03/22/2024).

[40] S. Zhu, P. Vazquez Ramos, O. R. Heckert, M. Stieger, A. J. van der Goot, and M. Schutyser, "Creating protein-rich snack foods using binder jet 3d printing," *Journal of Food Engineering*, vol. 332, p. 111 124, Nov. 1, 2022, ISSN: 0260-8774. DOI: 10.1016/j.jfoodeng.2022.111124. [Online]. Available: https://www.sciencedirect.com/science/article/pii/S0260877422001789 (visited on 10/05/2022).

[41] M. Caputo, C. V. Solomon, P.-K. Nguyen, and A. E. Berkowitz, "Electron microscopy investigation of binder saturation and microstructural defects in functional parts made by additive manufacturing," *Microscopy and Microanalysis*, vol. 22, pp. 1770–1771, S3 Jul. 2016, ISSN: 1431-9276, 1435-8115. DOI: 10.1017/S1431927616009697. [Online]. Available: https://www.cambridge.org/core/journals/microscopy-and-microanalysis/article/electron-microscopy-investigation-

of-binder-saturation-and-microstructural-defects-in-functional-parts-made-by-additive-manufacturing/C647ACEE9784368A2AC9585A59A6CF07 (visited on 03/22/2024).

[42] F. Liravi and M. Vlasea, "Powder bed binder jetting additive manufacturing of silicone structures," *Additive Manufacturing*, vol. 21, pp. 112–124, May 1, 2018, ISSN: 2214-8604. DOI: 10.1016/j.addma.2018.02.017. [Online]. Available: https://www.sciencedirect.com/science/article/pii/S2214860418300083 (visited on 10/05/2022).

[43] P. Stoyanov, K. Andre, P. Prichard, M. Yao, and C. Gey, "Microstructural and mechanical characterization of mo-containing stellite alloys produced by three dimensional printing," *Procedia CIRP*, 3rd CIRP Conference on Surface Integrity, vol. 45, pp. 167–170, Jan. 1, 2016, ISSN: 2212-8271. DOI: 10.1016/j.procir.2016.02.358. [Online]. Available: https://www.sciencedirect.com/science/article/pii/S2212827116007216 (visited on 03/22/2024).

[44] ExOne. "ExOne qualifies aluminum binder jet 3d printing with ford." (Mar. 11, 2021), [Online]. Available: https://www.exone.com/en-US/Ford-and-ExOne-Achieve-Scientific-Breakthrough (visited on 04/09/2024).

[45] P. R. (R. Baker, "Three dimensional printing with fine metal powders," Accepted: 2009-06-30T18:52:07Z Journal Abbreviation: 3D printing with fine metal powders, Thesis, Massachusetts Institute of Technology, 1997. [Online]. Available: https://dspace.mit.edu/handle/1721.1/46287 (visited on 02/13/2024).

[46] H. Miyanaji, K. M. Rahman, M. Da, and C. B. Williams, "Effect of fine powder particles on quality of binder jetting parts," *Additive Manufacturing*, vol. 36, p. 101 587, Dec. 1, 2020, ISSN: 2214-8604. DOI: 10.1016/j.addma.2020.101587.

[Online]. Available: https://www.sciencedirect.com/science/article/pii/S2214860420309593 (visited on 03/11/2024).

[47] X. Lv, F. Ye, L. Cheng, S. Fan, and Y. Liu, "Binder jetting of ceramics: Powders, binders, printing parameters, equipment, and post-treatment," *Ceramics International*, vol. 45, no. 10, pp. 12 609–12 624, Jul. 1, 2019, ISSN: 0272-8842. DOI: 10.1016/j.ceramint.2019.04.012. [Online]. Available: https://www.sciencedirect.com/science/article/pii/S0272884219308223 (visited on 10/05/2022).

[48] J. P. Kruth, "Material incress manufacturing by rapid prototyping techniques," *CIRP Annals*, vol. 40, no. 2, pp. 603–614, Jan. 1, 1991, ISSN: 0007-8506. DOI: 10.1016/S0007-8506(07)61136-6. [Online]. Available: https://www.sciencedirect.com/science/article/pii/S0007850607611366 (visited on 03/09/2024).

[49] M. Mahesh, "Rapid prototyping and manufacturing benchmarking," Accepted: 2010-04-08T10:45:49Z, Thesis, Mar. 22, 2005. [Online]. Available: https://scholarbank.nus.edu.sg/handle/10635/14697 (visited on 10/12/2023).

[50] L. Rebaioli and I. Fassi, "A review on benchmark artifacts for evaluating the geometrical performance of additive manufacturing processes," *The International Journal of Advanced Manufacturing Technology*, vol. 93, no. 5, pp. 2571–2598, Nov. 1, 2017, ISSN: 1433-3015. DOI: 10.1007/s00170-017-0570-0. [Online]. Available: https://doi.org/10.1007/s00170-017-0570-0 (visited on 10/12/2023).

[51] P. Shah, R. Racasan, and P. Bills, "Comparison of different additive manufacturing methods using computed tomography," *Case Studies in Nondestructive Testing and Evaluation*, Special Issue: Industrial computed tomography, vol. 6, pp. 69–78, Nov. 1, 2016, ISSN: 2214-6571. DOI: 10.1016/j.csndt.2016.05.008. [Online]. Available:

https://www.sciencedirect.com/science/article/pii/S2214657116300260 (visited on 10/12/2023).

[52] M. Mahesh, Y. Wong, J. Fuh, and H. Loh, "Benchmarking for comparative evaluation of RP systems and processes," *Rapid Prototyping Journal*, vol. 10, no. 2, pp. 123–135, Jan. 1, 2004, Publisher: Emerald Group Publishing Limited, ISSN: 1355-2546. DOI: 10.1108/13552540410526999. [Online]. Available: https://doi.org/10.1108/13552540410526999 (visited on 10/12/2023).

[53] H.-S. Byun and K. H. Lee, "Design of a new test part for benchmarking the accuracy and surface finish of rapid prototyping processes," in *Computational Science and Its Applications — ICCSA 2003*, V. Kumar, M. L. Gavrilova, C. J. K. Tan, and P. L'Ecuyer, Eds., ser. Lecture Notes in Computer Science, Berlin, Heidelberg: Springer, 2003, pp. 731–740, ISBN: 978-3-540-44842-6. DOI: 10.1007/3-540-44842-X_74.

[54] S. Moylan, J. Slotwinski, A. Cooke, K. Jurrens, and M. A. Donmez, "An additive manufacturing test artifact," *Journal of Research of the National Institute of Standards and Technology*, vol. 119, p. 429, Oct. 2014, ISSN: 2165-7254. DOI: 10.6028/jres.119.017. [Online]. Available: https://nvlpubs.nist.gov/nistpubs/jres/119/jres.119.017.pdf (visited on 10/12/2023).

[55] L. Castillo, "Study about the rapid manufacturing of complex parts of stainless steel and titanium," *TNO report with the collaboration of AIMME*, Nov. 16, 2005.

[56] R. Buswell, J. Xu, D. De Becker, *et al.*, "Geometric quality assurance for 3d concrete printing and hybrid construction manufacturing using a standardised test part for benchmarking capability," *Cement and Concrete Research*, vol. 156, p. 106 773, Jun. 1, 2022, ISSN: 0008-8846. DOI: 10.1016/j.cemconres.2022.106773. [Online].

Available: https://www.sciencedirect.com/science/article/pii/S0008884622000643 (visited on 03/09/2024).

[57] K. Kamarudin, M. S. Wahab, A. A. Raus, A. Ahmed, and S. Shamsudin, "Benchmarking of dimensional accuracy and surface roughness for AlSi10mg part by selective laser melting (SLM)," presented at the 7TH INTERNATIONAL CONFERENCE ON MECHANICAL AND MANUFACTURING ENGINEERING: Proceedings of the 7th International Conference on Mechanical and Manufacturing Engineering, Sustainable Energy Towards Global Synergy, Jogjakarta, Indonesia, 2017, p. 020 047. DOI: 10.1063/1.4981188. [Online]. Available: https://pubs.aip.org/aip/acp/article/885466 (visited on 03/09/2024).

[58] C. Relvas, A. Ramos, A. Completo, and J. A. Simões, "A systematic approach for an accuracy level using rapid prototyping technologies," *Proceedings of the Institution of Mechanical Engineers, Part B: Journal of Engineering Manufacture*, vol. 226, no. 12, pp. 2023–2034, Dec. 1, 2012, Publisher: IMECHE, ISSN: 0954-4054. DOI: 10.1177/0954405412461865. [Online]. Available: https://doi.org/10.1177/0954405412461865 (visited on 03/09/2024).

[59] M. Moshiri, S. Candeo, S. Carmignato, S. Mohanty, and G. Tosello, "Benchmarking of laser powder bed fusion machines," *Journal of Manufacturing and Materials Processing*, vol. 3, no. 4, p. 85, Dec. 2019, Number: 4 Publisher: Multidisciplinary Digital Publishing Institute, ISSN: 2504-4494. DOI: 10.3390/jmmp3040085. [Online]. Available: https://www.mdpi.com/2504-4494/3/4/85 (visited on 10/12/2023).

[60] V. M. Rivas Santos, A. Thompson, D. Sims-Waterhouse, I. Maskery, P. Woolliams, and R. Leach, "Design and characterisation of an additive manufacturing benchmarking artefact following a design-for-metrology approach," *Additive Manufactur-*

ing, vol. 32, p. 100 964, Mar. 1, 2020, ISSN: 2214-8604. DOI: 10.1016/j.addma.2019.100964. [Online]. Available: https://www.sciencedirect.com/science/article/pii/S2214860419301137 (visited on 03/09/2024).

[61] J. Montero, S. Weber, C. Petroll, *et al.*, "Geometrical benchmarking of laser powder bed fusion systems based on designer needs," *Proceedings of the Design Society*, vol. 1, pp. 1657–1666, Aug. 2021, ISSN: 2732-527X. DOI: 10.1017/pds.2021.427. [Online]. Available: https://www.cambridge.org/core/journals/proceedings-of-the-design-society/article/geometrical-benchmarking-of-laser-powder-bed-fusion-systems-based-on-designer-needs/795C7EF675FF7F96BDD43F4ED1C339E1 (visited on 03/09/2024).

[62] S. Giganto, S. Martínez-Pellitero, E. Cuesta, P. Zapico, and J. Barreiro, "Proposal of design rules for improving the accuracy of selective laser melting (SLM) manufacturing using benchmarks parts," *Rapid Prototyping Journal*, vol. 28, no. 6, pp. 1129–1143, 2022, Num Pages: 15 Place: Bradford, United Kingdom Publisher: Emerald Group Publishing Limited, ISSN: 13552546. DOI: 10.1108/RPJ-06-2021-0130. [Online]. Available: https://www.proquest.com/docview/2666837175/abstract/D6815823FAF149F0PQ/1 (visited on 03/11/2024).

[63] W. M. Johnson, M. Rowell, B. Deason, and M. Eubanks, "Benchmarking evaluation of an open source fused deposition modeling additive manufacturing system," presented at the International Solid Freeform Fabrication Symposium, Accepted: 2021-10-04T21:18:43Z, University of Texas at Austin, 2011. DOI: 10.26153/tsw/15288. [Online]. Available: https://repositories.lib.utexas.edu/handle/2152/88349 (visited on 10/12/2023).

[64] E. Lopez, T. Felgueiras, C. Grunert, *et al.*, "Evaluation of 3d-printed parts by means of high-performance computer tomography," *Journal of Laser Applications*, vol. 30, no. 3, p. 032 307, Jun. 20, 2018, ISSN: 1042-346X. DOI: 10.2351/1.5040644. [Online]. Available: https://doi.org/10.2351/1.5040644 (visited on 03/11/2024).

[65] J. Allison, C. Sharpe, and C. C. Seepersad, "Powder bed fusion metrology for additive manufacturing design guidance," *Additive Manufacturing*, vol. 25, pp. 239–251, Jan. 1, 2019, ISSN: 2214-8604. DOI: 10.1016/j.addma.2018.10.035. [Online]. Available: https://www.sciencedirect.com/science/article/pii/S2214860418304330 (visited on 03/11/2024).

[66] H. Miyanaji, N. Momenzadeh, and L. Yang, "Effect of printing speed on quality of printed parts in binder jetting process," *Additive Manufacturing*, vol. 20, pp. 1–10, Mar. 1, 2018, ISSN: 2214-8604. DOI: 10.1016/j.addma.2017.12.008. [Online]. Available: https://www.sciencedirect.com/science/article/pii/S2214860417305080 (visited on 03/11/2024).

[67] M. Vaezi and C. K. Chua, "Effects of layer thickness and binder saturation level parameters on 3d printing process," *The International Journal of Advanced Manufacturing Technology*, vol. 53, no. 1, pp. 275–284, Mar. 1, 2011, ISSN: 1433-3015. DOI: 10.1007/s00170-010-2821-1. [Online]. Available: https://doi.org/10.1007/s00170-010-2821-1 (visited on 03/12/2024).

[68] T.-J. Hsu and W.-H. Lai, "Manufacturing parts optimization in the three-dimensional printing process by the taguchi method," *Journal of the Chinese Institute of Engineers*, vol. 33, no. 1, pp. 121–130, Jan. 1, 2010, Publisher: Taylor & Francis _eprint: https://doi.org/10.1080/02533839.2010.9671604, ISSN: 0253-3839. DOI: 10.1080/

02533839.2010.9671604. [Online]. Available: https://doi.org/10.1080/02533839.2010.9671604 (visited on 03/17/2024).

[69] B. Weiss, O. Diegel, D. Storti, and M. Ganter, "A process for estimating minimum feature size in selective laser sintering," *Rapid Prototyping Journal*, vol. 24, no. 2, pp. 436–440, 2018, Num Pages: 5 Place: Bradford, United Kingdom Publisher: Emerald Group Publishing Limited, ISSN: 13552546. DOI: 10.1108/RPJ-01-2017-0001. [Online]. Available: https://www.proquest.com/docview/2023913571/abstract/373DAE327FA3459EPQ/1 (visited on 03/11/2024).

[70] G. D. Kim and Y. T. Oh, "A benchmark study on rapid prototyping processes and machines: Quantitative comparisons of mechanical properties, accuracy, roughness, speed, and material cost," *Proceedings of the Institution of Mechanical Engineers, Part B: Journal of Engineering Manufacture*, vol. 222, no. 2, pp. 201–215, Feb. 1, 2008, Publisher: IMECHE, ISSN: 0954-4054. DOI: 10.1243/09544054JEM724. [Online]. Available: https://doi.org/10.1243/09544054JEM724 (visited on 03/09/2024).

[71] M. N. Islam and S. Sacks, "An experimental investigation into the dimensional error of powder-binder three-dimensional printing," *The International Journal of Advanced Manufacturing Technology*, vol. 82, no. 5, pp. 1371–1380, Feb. 1, 2016, ISSN: 1433-3015. DOI: 10.1007/s00170-015-7482-7. [Online]. Available: https://doi.org/10.1007/s00170-015-7482-7 (visited on 03/09/2024).

[72] D. Dimitrov, W. van Wijck, K. Schreve, and N. de Beer, "Investigating the achievable accuracy of three dimensional printing," *Rapid Prototyping Journal*, vol. 12, no. 1, pp. 42–52, Jan. 1, 2006, Publisher: Emerald Group Publishing Limited, ISSN:

1355-2546. DOI: 10.1108/13552540610637264. [Online]. Available: https://doi.org/10.1108/13552540610637264 (visited on 10/12/2023).

[73] L. L. Howell, S. P. Magleby, and B. M. Olsen, Eds., *Handbook of compliant mechanisms*, Chichester, West Sussex, United Kingdom ; Hoboken: John Wiley & Sons, Inc, 2013, 324 pp., ISBN: 978-1-119-95345-6.

[74] O. Ibhadode, I. Z. Rishmawi, M. Kirby, M. Vlasea, and S. Winkler, "Topological fidelity of additively manufactured AlSi10mg gyroid structures," *Journal of Manufacturing Processes*, vol. 108, pp. 671–684, Dec. 2023, ISSN: 15266125. DOI: 10.1016/j.jmapro.2023.11.033. [Online]. Available: https://linkinghub.elsevier.com/retrieve/pii/S1526612523010800 (visited on 02/28/2024).

[75] A. J. L. Morgan, L. H. S. Jose, W. D. Jamieson, *et al.*, "Simple and versatile 3d printed microfluidics using fused filament fabrication," *PLOS ONE*, vol. 11, no. 4, e0152023, Apr. 6, 2016, Publisher: Public Library of Science, ISSN: 1932-6203. DOI: 10.1371/journal.pone.0152023. [Online]. Available: https://journals.plos.org/plosone/article?id=10.1371/journal.pone.0152023 (visited on 03/06/2024).

[76] ExOne, *M-flex data sheet*. [Online]. Available: https://www.exone.com/getattachment/fb0a12be-2566-412a-abfd-6b720e0c287b/m-flex-data-sheet-08312020.pdf (visited on 03/21/2024).

[77] A. T. Sutton, C. S. Kriewall, M. C. Leu, and J. W. Newkirk, "Powder characterisation techniques and effects of powder characteristics on part properties in powder-bed fusion processes," *Virtual and Physical Prototyping*, vol. 12, no. 1, pp. 3–29, Jan. 2, 2017, ISSN: 1745-2759. DOI: 10.1080/17452759.2016.1250605. [Online].

Available: https://doi.org/10.1080/17452759.2016.1250605 (visited on 03/22/2024).

[78] S. Mirzababaei, B. K. Paul, and S. Pasebani, "Metal powder recyclability in binder jet additive manufacturing," *JOM*, vol. 72, no. 9, pp. 3070–3079, Sep. 1, 2020, ISSN: 1543-1851. DOI: 10.1007/s11837-020-04258-6. [Online]. Available: https://doi.org/10.1007/s11837-020-04258-6 (visited on 08/22/2023).

[79] Ultimaker B.V., *Ultimaker cura*, version 5.4.0, Jul. 2023. [Online]. Available: https://github.com/Ultimaker/Cura.

[80] R. Boychuk, "Towards predicting densification and deformation in the sintering of binder-jet additively manufactured parts," Ph.D. dissertation, University of Waterloo, Waterloo, Ontario, Canada, 2023.

[81] Keyence, *Keyence VHX-700 manual*.

[82] E. Yang, *Ewdyang/open-OpticalComparator*, Mar. 8, 2024. [Online]. Available: https://github.com/ewdyang/Open-OpticalComparator (visited on 03/17/2024).

[83] G. Bradski, "The OpenCV library," *Dr. Dobb's Journal of Software Tools*, 2000, tex.citeulike-article-id: 2236121 tex.posted-at: 2008-01-15 19:21:54 tex.priority: 4.

[84] S. van der Walt, J. L. Schönberger, J. Nunez-Iglesias, *et al.*, "Scikit-image: Image processing in python," *PeerJ*, vol. 2, e453, Jun. 2014, ISSN: 2167-8359. DOI: 10.7717/peerj.453. [Online]. Available: https://doi.org/10.7717/peerj.453.

[85] Dawson-Haggerty et al., *Trimesh*, version 3.2.0, Dec. 8, 2019. [Online]. Available: https://trimesh.org/.

[86] P. Virtanen, R. Gommers, T. E. Oliphant, *et al.*, "SciPy 1.0: Fundamental algorithms for scientific computing in python," *Nature Methods*, vol. 17, pp. 261–272, 2020, tex.adsurl: https://rdcu.be/b08Wh. DOI: 10.1038/s41592-019-0686-2.

[87] S. Gillies, C. van der Wel, J. Van den Bossche, M. W. Taves, J. Arnott, B. C. Ward, *et al.*, *Shapely*, version 2.0.3, Feb. 2024. DOI: 10.5281/zenodo.10671398. [Online]. Available: https://doi.org/10.5281/zenodo.10671398.

[88] A. Murray, H. v. Kemenade, wiredfool, *et al.*, *Python-pillow/pillow: 10.2.0*, version 10.2.0, Jan. 2, 2024. DOI: 10.5281/zenodo.10450403. [Online]. Available: https://zenodo.org/records/10450403 (visited on 03/03/2024).

[89] A. A. Hagberg, D. A. Schult, and P. J. Swart, "Exploring network structure, dynamics, and function using NetworkX," in *Proceedings of the 7th python in science conference*, G. Varoquaux, T. Vaught, and J. Millman, Eds., Pasadena, CA USA, 2008, pp. 11–15.

[90] C. R. Harris, K. J. Millman, S. J. van der Walt, *et al.*, "Array programming with NumPy," *Nature*, vol. 585, no. 7825, pp. 357–362, Sep. 2020, Publisher: Springer Science and Business Media LLC. DOI: 10.1038/s41586-020-2649-2. [Online]. Available: https://doi.org/10.1038/s41586-020-2649-2.

[91] I. D. Coope, "Circle fitting by linear and nonlinear least squares," *Journal of Optimization Theory and Applications*, vol. 76, no. 2, pp. 381–388, Feb. 1993, ISSN: 0022-3239, 1573-2878. DOI: 10.1007/BF00939613. [Online]. Available: http://link.springer.com/10.1007/BF00939613 (visited on 02/25/2024).

[92] K. Myers, A. Paterson, T. Iizuka, and A. Klein, "The effect of print speed on surface roughness and density uniformity of parts produced using binder jet 3d printing," PHYSICAL SCIENCES, preprint, Jan. 25, 2021. DOI: 10.20944/preprints202101.0459.v1. [Online]. Available: https://www.preprints.org/manuscript/202101.0459/v1 (visited on 02/29/2024).

[93] H. Miyanaji, S. Zhang, A. Lassell, A. Zandinejad, and L. Yang, "Process development of porcelain ceramic material with binder jetting process for dental applications," *JOM*, vol. 68, no. 3, pp. 831–841, Mar. 1, 2016, ISSN: 1543-1851. DOI: 10.1007/s11837-015-1771-3. [Online]. Available: https://doi.org/10.1007/s11837-015-1771-3 (visited on 03/21/2024).

[94] H. Miyanaji, S. Zhang, and L. Yang, "A new physics-based model for equilibrium saturation determination in binder jetting additive manufacturing process," *International Journal of Machine Tools and Manufacture*, vol. 124, pp. 1–11, Jan. 1, 2018, ISSN: 0890-6955. DOI: 10.1016/j.ijmachtools.2017.09.001. [Online]. Available: https://www.sciencedirect.com/science/article/pii/S0890695517301335 (visited on 03/16/2024).

[95] Y. Bai, C. Wall, H. Pham, A. Esker, and C. B. Williams, "Characterizing binder-powder interaction in binder jetting additive manufacturing via sessile drop goniometry," *Journal of Manufacturing Science and Engineering*, vol. 141, no. 11005, Oct. 19, 2018, ISSN: 1087-1357. DOI: 10.1115/1.4041624. [Online]. Available: https://doi.org/10.1115/1.4041624 (visited on 03/22/2024).

[96] D. C. Montgomery, E. A. Peck, and G. G. Vining, "Introduction to linear regression analysis," in *Introduction to linear regression analysis*, ser. Wiley series in probability and statistics, Sixth edition., tex.lccn: 2020034055, Hoboken, NJ: John Wiley & Sons, Inc., 2021, ISBN: 978-1-119-57872-7.

[97] H. Chen and Y. F. Zhao, "Process parameters optimization for improving surface quality and manufacturing accuracy of binder jetting additive manufacturing process," *Rapid Prototyping Journal*, vol. 22, no. 3, pp. 527–538, Jan. 1, 2016, Publisher: Emerald Group Publishing Limited, ISSN: 1355-2546. DOI: 10.1108/RPJ-11-2014-

0149. [Online]. Available: https://doi.org/10.1108/RPJ-11-2014-0149 (visited on 03/08/2024).

[98] K. Lu and W. T. Reynolds, "3dp process for fine mesh structure printing," *Powder Technology*, vol. 187, no. 1, pp. 11–18, Oct. 8, 2008, ISSN: 0032-5910. DOI: 10.1016/j.powtec.2007.12.017. [Online]. Available: https://www.sciencedirect.com/science/article/pii/S0032591008000053 (visited on 03/12/2024).

[99] H. Miyanaji, "Binder jetting additive manufacturing process fundamentals and the resultant influences on part quality.," Ph.D. dissertation, University of Louisville, 2018. DOI: 10.18297/etd/3058. [Online]. Available: https://ir.library.louisville.edu/etd/3058 (visited on 03/11/2024).

[100] M. Ntousia, I. Fudos, S. Moschopoulos, and V. Stamati, "Predicting geometric errors and failures in additive manufacturing," *Rapid Prototyping Journal*, vol. 29, no. 9, pp. 1843–1861, 2023, ISSN: 1355-2546. DOI: 10.1108/RPJ-11-2022-0402.